

University of Alberta

Free-breathing Cine-Navigator Cardiac Magnetic Resonance Imaging

by

Angela On Yee Leung



A thesis submitted to the Faculty of Graduate Studies and Research
in partial fulfillment of the requirements for the degree of

Master of Science

Department of Biomedical Engineering

Edmonton, Alberta

Spring 2007



Library and
Archives Canada

Bibliothèque et
Archives Canada

Published Heritage
Branch

Direction du
Patrimoine de l'édition

395 Wellington Street
Ottawa ON K1A 0N4
Canada

395, rue Wellington
Ottawa ON K1A 0N4
Canada

Your file *Votre référence*
ISBN: 978-0-494-29984-5
Our file *Notre référence*
ISBN: 978-0-494-29984-5

NOTICE:

The author has granted a non-exclusive license allowing Library and Archives Canada to reproduce, publish, archive, preserve, conserve, communicate to the public by telecommunication or on the Internet, loan, distribute and sell theses worldwide, for commercial or non-commercial purposes, in microform, paper, electronic and/or any other formats.

The author retains copyright ownership and moral rights in this thesis. Neither the thesis nor substantial extracts from it may be printed or otherwise reproduced without the author's permission.

AVIS:

L'auteur a accordé une licence non exclusive permettant à la Bibliothèque et Archives Canada de reproduire, publier, archiver, sauvegarder, conserver, transmettre au public par télécommunication ou par l'Internet, prêter, distribuer et vendre des thèses partout dans le monde, à des fins commerciales ou autres, sur support microforme, papier, électronique et/ou autres formats.

L'auteur conserve la propriété du droit d'auteur et des droits moraux qui protègent cette thèse. Ni la thèse ni des extraits substantiels de celle-ci ne doivent être imprimés ou autrement reproduits sans son autorisation.

In compliance with the Canadian Privacy Act some supporting forms may have been removed from this thesis.

Conformément à la loi canadienne sur la protection de la vie privée, quelques formulaires secondaires ont été enlevés de cette thèse.

While these forms may be included in the document page count, their removal does not represent any loss of content from the thesis.

Bien que ces formulaires aient inclus dans la pagination, il n'y aura aucun contenu manquant.


Canada

Every experiment proves something.
If it doesn't prove what you wanted it
to prove, it proves something else.

Prof. Anon

Abstract

In cardiovascular MRI, breathing will sometimes blur images beyond diagnostic value. Free-breathing cine-navigator imaging corrects respiratory-related displacements using the k-space data for both motion correction and image reconstruction. An interleaved segmented radial trajectory was implemented in a retrospectively-gated SSFP scan, allowing real-time images to be acquired throughout a conventional gated-segmented experiment. The real-time images were registered for each cardiac phase, providing cardiac-motion-independent respiratory motion information that was used to correct the k-space data prior to gated-segmented cine image reconstruction. Profiles were drawn over uncorrected, corrected free-breathing and breath-hold images to measure the maximum normalized sharpness. There is significant improvement in edge sharpness, especially in the direction of respiratory motion, and residual blurring artifacts are due to local deformations uncorrectable by the current affine motion model or regridding error. Thresholding and masking did not affect the reconstruction, but this may be due to the success of the motion correction.

Acknowledgements

Thanks go to my supervisor Dr. Richard Thompson for his insight, guidance and helpful discussions on the principles of MR imaging, signal processing, and the graduate studies experience as a whole. He has taught me a lot about the world of scientific research while reminding me to keep an eye on the big picture. I would also like to acknowledge my supervisory committee, consisting of Dr. Alan Wilman, Dr. Ian Patterson and chair Dr. Kelvin Jones, who willingly donated their time and energy (thanks for reading my thesis during your sabbatical Alan!). Their comments were useful in creating this manuscript. Thanks go to the Alberta Heritage Foundation for Medical Research for funding this project.

Further acknowledgement must be given to the other students and staff in the department, who answered my numerous questions and commiserated over some of the roadblocks that arose during the course of my degree. Finally, I am grateful to my friends for keeping me grounded and at times forcefully encouraging me to have a life outside research, and to my family, who have offered unconditional support for all my endeavours.

Table of Contents

1	Introduction.....	1
2	MR Physics and Imaging Basics.....	3
2.1	NMR Phenomenon.....	3
2.1.1	Quantum Mechanical Properties.....	3
2.1.2	Polarization	6
2.1.3	Energy Levels	7
2.1.4	Bulk Magnetization.....	9
2.1.5	Nuclear Precession.....	10
2.1.6	Transverse Excitation.....	11
2.1.7	Nuclear shielding	14
2.1.8	Bloch Equation & Rotating Frame of Reference.....	15
2.1.9	Flip Angle	18
2.1.10	Relaxation	19
2.2	Imaging Basics.....	24
2.2.1	Gradients.....	25
2.2.2	Slice Selection.....	28
2.2.3	Frequency and Phase Encoding	30
2.2.4	K-space Formalism	33
2.2.5	Contrast Mechanisms.....	37
2.2.6	Pulse Sequences	38
2.3	Projection Reconstruction Trajectory	45
2.3.1	Projection Reconstruction.....	46

2.3.2	Regridding.....	47
2.3.3	Undersampling.....	50
3	Cardiac Imaging (Literature Review).....	53
3.1	Cardiac Gating.....	53
3.2	Respiratory Motion.....	55
3.2.1	Artifacts.....	56
3.2.2	Motion Artifact Suppression.....	58
3.2.3	Real-time Ultrafast Imaging.....	65
3.2.4	Motion Artifact Correction.....	65
3.2.5	Dual-Purpose Acquisition.....	67
4	Methods.....	69
4.1	K-space Acquisition Scheme.....	69
4.2	Real-time Motion Measurement.....	75
4.3	Image Correction & Ultimate Reconstruction.....	79
4.3.1	Patient Studies.....	80
4.3.2	Quantitative Sharpness Analysis.....	81
5	Results.....	84
5.1	Acquisition.....	84
5.2	Full Reconstruction.....	84
5.3	Correlation Threshold Reconstruction.....	85
5.4	Sharpness Profiling Analysis.....	87
5.5	Individual Ventricle Correction.....	93
5.6	Other Orientations.....	96

6	Discussion/Conclusion.....	99
7	Bibliography	105
8	Appendix I	111

List of Tables

Table 2.1 Table of magnetogyric ratios for isotopes common in medical imaging, with I values. 6

Table 5.1 Summary of results of motion correction for EH mask, for ED, ES and MC images, across four profiles (IVS, LV-PFW, LV-LFW, LV-AFW). 1 means there is significant difference between the image series (FB, MCFB, BH), 0 means there is none. 93

Table 5.2 Summary of results of motion correction for LV mask, for ED, ES and MC images, across four profiles (IVS, LV-PFW, LV-LFW, LV-AFW). 1 means there is significant difference between the image series (FB, MCFB, BH), 0 means there is none. 96

List of Figures

- Figure 2.1** Representation of classical vector model. Left, spinning charged nuclei with magnetic field lines. Right, magnetic moment vector $\vec{\mu}$ represented as an arrow. 4
- Figure 2.2** Left, randomly oriented magnetic moment vectors. Right, external field vector B_0 and parallel/anti-parallel moment vectors for spin- $1/2$ system..... 7
- Figure 2.3** Zeeman splitting phenomenon for spin- $1/2$ system. When in the presence of B_0 the spins will populate parallel and anti-parallel energy states ($m = -1/2, 1/2$), with an energy level difference ΔE 8
- Figure 2.4** Precession of spin $\vec{\mu}$ about the longitudinal magnetic field \vec{B}_0 at Larmor frequency ω_0 . Direction of precession follows left-hand rule. 11
- Figure 2.5** Illustration of precessing transverse magnetization \vec{M}_{xy} inducing an FID signal in an RF coil placed along the y-axis. The signal decays away with time due to relaxation..... 14
- Figure 2.6** Rotating frame of reference. a) In the general case, \vec{M}_p rotates in a cone of precession about \vec{B}_{eff} at frequency ω_{eff} . b) When the resonance condition is fulfilled, \vec{M}_p precesses about \vec{B}_1 at frequency ω_1 . The flip angle θ is measured from the positive z-axis and depends on the strength and duration of the excitation RF pulse. 18
- Figure 2.7** Longitudinal relaxation curves for 90° and 180° pulses [3]..... 20
- Figure 2.8** Transverse relaxation curve, showing transverse magnetization decay over time [3]..... 22
- Figure 2.9** Spin-echo generation. The dephasing transverse magnetization is refocused by applying a 180°_x pulse that flips the spins over the x_p -axis. After a time τ , the spins meet up again on the opposite side of the y_p -axis, generating a second FID signal called the spin-echo [3]..... 24
- Figure 2.10** Plot of magnetic field strength B versus distance x from the iso-centre of the magnet while a linear gradient G_x is applied. Gradient strength is zero at iso-centre (effective field is B_0). 26
- Figure 2.11** After excitation, spin vectors $\vec{\mu}_1$ and $\vec{\mu}_2$ precess away from the y-axis and accumulate a phase angle ϕ , dependent on the spin's frequency ω and precession time..... 27

Figure 2.12 Slice selection on an arbitrary r-axis involving the spatial encoding of spin frequency ω by a linear gradient G_r . The slice width Δr is determined by the RF pulse bandwidth $\Delta\omega_{RF}$	29
Figure 2.13 Rephasing lobe which is half the total area of the slice select gradient.	30
Figure 2.14 T_1 relaxation contrast mechanism. Tissues with different T_1 values will have different longitudinal magnetization amounts after a time t . The larger the difference in magnetization, the more image contrast obtained [3].....	38
Figure 2.15 Spin-echo pulse sequence. After the 90°_z excitation RF pulse, the spins are dephased by a preparation FE gradient, then flipped over the x-axis by the 180°_x pulse. This creates a spin echo signal in the middle of the acquisition period. G_{slice} , slice-select gradient; G_{read} , readout gradient; G_{phase} , phase-encode gradient; ADC, analog-to-digital converter; TE, excitation time. Adapted from [6].....	40
Figure 2.16 Gradient-echo or FLASH pulse sequence. A preparatory dephasing gradient is applied in the readout direction to create a gradient echo at the centre of the acquisition period. The excitation RF pulse flip angle α is less than 90° . Adapted from [6].....	42
Figure 2.17 Typical SSFP pulse sequence. RF pulses are symmetrical and all gradient effects are rewound. TR, repetition time [6].....	45
Figure 2.18 Projection reconstruction trajectory with 32 evenly spaced projections. The dotted circle delineates the threshold for full FOV reconstruction [9].....	46
Figure 2.19 Kaiser-Bessel function used as the convolution kernel. $N = 3$, $M = 2048$, order = 8. a) $\beta = 8$. b) $\beta = 16$. Circles indicate the N sampling trajectory points.....	48
Figure 2.20 Undersampling for projection reconstruction trajectory can be accomplished by reducing the number of projections N_p so the angular spacing $\Delta k_{\theta max}$ exceeds the radial spacing Δk_r . The angular step size is given by π/N_p [13].....	51
Figure 2.21 Point spread functions of a) undersampled PR and b) truncated undersampled PR. The unaliased or low-aliasing zone and the main lobe is wider for b), leading to increased blurring but decreased overall aliasing [9].....	52
Figure 3.1 Cardiac gated-segmented acquisition. K-space data acquired at each cardiac phase can be combined into a fully sampled dataset that gives a high spatial and temporal resolution image. a) Prospective triggering acquires a certain	

number of segments for each cardiac cycle starting at a particular point in the cardiac cycle, regardless of the length of each individual heartbeat. b) Retrospective triggering acquires segments over the entire acquisition, relying on recorded ECG signal data to match up the data for the appropriate phases post-acquisition. 55

Figure 3.2 A 1D signal $s(t')$ obtained by applying different phase-encode gradient pulses is modulated by a periodic motion-induced variation in signal $m(t')$. In image space, this translates into the convolution of the corresponding component of the stationary object $S(f)$ by the Fourier transform of the modulation function $M(f)$ [20]. 57

Figure 3.3 a) Breath-hold gold standard and b) free-breathing short-axis cardiac images. In b), the edge of the myocardium is blurred, and fine features such as pulmonary vessels in the lungs are obscured (arrows). Adapted from [29]. 59

Figure 3.4 Typical vertical navigator echo used in cardiac imaging. a) Coronal scout MR image showing column of excited spins across liver-diaphragm-lung boundary marked by white rectangle, with right hemidiaphragm marked by white arrow. b) 1D edge signal representing respiratory motion over time [36]. 62

Figure 4.1 K-space dual-purpose acquisition scheme. Sliding window reconstruction is used to create a series of real-time subimages (left) for respiratory motion navigation purposes. The corrected k-space lines are then used in conventional gated-segmented reconstruction to create high temporal and spatial resolution cine-images, which contain blurring and ghosting due to motion (right). For greater temporal resolution of each line, each unique segment configuration (i.e. segment 1, 2, 3, 4, 5, etc) is acquired over several heartbeats. 71

Figure 4.2 K-space radial trajectory interleaving. Each consecutive radial segment configuration is angularly offset from the previous. This gives even coverage of k-space for both the undersampled real-time and the combined gated-segmented dataset. 72

Figure 4.3 K-space segment line ordering. a) Conventional cine-imaging line interleaving with each segment's lines or projections evenly covering k-space, and b) cine-navigator line interleaving, where every two consecutive segments' projections combine for a more densely sampled dataset. Each line is acquired at different times for each heartbeat due to retrospective triggering, so each unique segment configuration is acquired over several heartbeats to maintain the temporal resolution of the k-space lines (in this example, lines have been shifted by a whole cardiac phase from one heartbeat to the next). 73

Figure 4.4 a) Undersampled RT DCF (calculated with $N = 9$, $\beta = 8$ Kaiser-Bessel kernel). b) Fully sampled GS DCF (Shepp-Logan filter). The vertical axis gives

the weighting value while the horizontal axis gives the index of the readout points in each projection. The DCF would be applied to each individual projection in the RT or GS k-space dataset..... 74

Figure 4.5 Flowchart of real-time respiratory motion measurement and correction procedure..... 75

Figure 4.6 Reference profile-time series. a) A 1-D profile (white line) is chosen parallel to the intraventricular septum (white arrow) across the left ventricle for all the real-time images, going from left to right. b) When ordered sequentially, the profile series gives the translational motion with respect to time in that direction. Both the respiratory and cardiac motion characteristics are easily visible. The white lines delineate the individual cardiac cycles. 76

Figure 4.7 In-plane translation (x and y directions) as well as rotation parameters returned by the registration algorithm, mapped out serially in time..... 77

Figure 4.8 Affine registration algorithm phantom test. a) Difference image of phantom and artificially sheared phantom. b) Difference image of phantom and artificially sheared phantom corrected with output parameters of registration algorithm. c) Difference image of phantom and artificially sheared phantom corrected with inverse transpose of registration algorithm output parameters. 79

Figure 4.9 Flowchart of statistical analysis using the results of the one-way ANOVA test with Tukey-Kramer analysis. F values indicate if there is significant difference between any of the means of the groups being compared, while the Tukey-Kramer analysis performs pairwise comparisons to see which of the groups are significantly different. FB, free-breathing; MCFB, motion-corrected free-breathing; BH, breath-hold image series. 82

Figure 5.1 a) Pre-registration free-breathing, b) post-registration free-breathing, and c) breath-hold gold standard short-axis gated-segmented image. Images within each series are at (from left-to-right) end-diastole, end-systole, and mid-contraction..... 85

Figure 5.2 Sample histograms of correlation coefficient values for pre- (top) and post-registration (bottom) real-time images of short-axis view. Threshold levels for 10%, 20% and 30% removal of lines from final reconstruction are shown on the post-registration histogram. 86

Figure 5.3 Correlation thresholded images at end-diastole: a) full reconstruction, b) 10% threshold, c) 20% threshold, and d) 30% threshold. 87

Figure 5.4 a) Example of profiles drawn over the left ventricle at end-diastole for the three image series (FB, MCFB, BH). The corresponding normalized signal profile plots are given for the b) IVS, c) LV-PFW, d) LV-LFW, and e) LV-AFW.

The maximum absolute normalized sharpness ($\max |S_{h_{norm}}|$) is indicated on the graph with a diamond..... 89

Figure 5.5 Motion correction with entire-heart mask. Box plots of $\max |S_{h_{norm}}|$ values for 4 profiles drawn on three different cardiac phases across 9 patient studies. ED, end-diastole; ES, end-systole; MC, mid-contraction. Profile 1, IVS; Profile 2, LV-PFW; Profile 3, LV-LFW; Profile 4, LV-AFW. Column 1, FB; Column 2, MCFB; Column 3, BH..... 90

Figure 5.6 Motion correction with entire-heart mask. Graph of estimated differences between mean maximum $|S_{h_{norm}}|$ values for each pairwise comparison (FB-BH, FB-MCFB, MCFB-BH) and the respective confidence interval limits for $p < 0.05$. If range does not include 0, groups are significantly different. Profile 1, IVS; Profile 2, LV-PFW; Profile 3, LV-LFW; Profile 4, LV-AFW..... 91

Figure 5.7 Motion correction with left-ventricle mask. Box plots of $\max |S_{h_{norm}}|$ values for 4 profiles drawn on three different cardiac phases across 9 patient studies. ED, end-diastole; ES, end-systole; MC, mid-contraction. Profile 1, IVS; Profile 2, LV-PFW; Profile 3, LV-LFW; Profile 4, LV-AFW. Column 1, FB; Column 2, MCFB; Column 3, BH..... 94

Figure 5.8 Motion correction with left-ventricle mask. Graph of estimated differences between mean maximum $|S_{h_{norm}}|$ values for each pairwise comparison (FB-BH, FB-MCFB, MCFB-BH) and the respective confidence interval limits for $p < 0.05$. If range does not include 0, groups are significantly different. 95

Figure 5.9 Sample histograms of correlation coefficient values for pre- (top) and post-registration (bottom) real-time images of four-chamber orientation. Threshold levels for 10%, 20% and 30% removal of lines from final reconstruction are shown on the post-registration histogram. 97

Figure 5.10 4-chamber view of the heart for: a) uncorrected free-breathing, b) motion-corrected free-breathing at full reconstruction, c) 10% thresholded, and d) 30% thresholded motion-corrected free-breathing. 98

List of Symbols, Nomenclature, and Abbreviations

CT	computed tomography
MRI	magnetic resonance imaging
NMR	nuclear magnetic resonance
Z	atomic number
A	atomic mass
\vec{J}	angular momentum or spin
$\vec{\mu}$	magnetic moment
γ	magnetogyric ratio
γ	magnetogyric ratio, in frequency scale
\hbar	Planck's constant in frequency scale (1.055 x 10 ⁻³⁴ Js)
I	nuclear spin quantum number
m _I	magnetic quantum number
\vec{B}	magnetic field
ω_0	Larmor frequency
E	energy
K	Boltzmann constant (1.38 x 10 ⁻²³ J/K)
T	temperature
n _↑ , n _↓	number of parallel, anti-parallel spins
\vec{M}	magnetization
N _s	number of spins

φ	phase angle
RF	radiofrequency
$T_{1,2}$	longitudinal, transverse relaxation time constants
T_2^*	overall transverse relaxation time constant
T_2'	transverse relaxation time constant due to static inhomogeneities
ρ	subscript indicating rotating frame of reference
θ	flip angle
t, τ	time
$S(t)$	detected NMR signal
FID	free induction decay
TE/TR	excitation time/repetition time
G	gradient
SR	slew rate
Δr	slice width in any direction
FE/PE	frequency encode/phase encode
f_s	sampling frequency
f_{\max}	sampling bandwidth
FOV	field of view
N	number of pixels per dimension
SE/TSE/FSE	spin echo/turbo spin echo/fast spin echo

GRE/FLASH	gradient returned echo/fast low angle shot
SSFP/FISP	steady state free precession/fast imaging with steady state precession
SNR	signal to noise ratio
PR	projection reconstruction
$N_{p,r}$	number of projections, readout points
FFT	fast Fourier transform
$C(k_x, k_y)$	convolution kernel (k-space units)
β	Kaiser-Bessel shape factor
N	Kaiser-Bessel kernel number of sampling points
M	Kaiser-Bessel kernel number of inter- sampling points
\otimes	convolution
DCF, $W(k_x, k_y)$	density compensation function, weighting function (k-space units)
$M_C(k_x, k_y)$	regridded k-space data (k-space units)
$M_S(k_x, k_y)$	original k-space data (k-space units)
$S(k_x, k_y)$	sampling trajectory (k-space units)
$R(k_x, k_y)$	Cartesian sampling trajectory (k-space units)
PSF	point spread function
d	distance between ghost artifacts
f_{mot}	frequency of motion ghost artifacts

DVA	diminishing variance algorithm
ROPE/COPE	respiratory/centrally ordered phase encoding
MAST	motion artifact suppression technique
A	affine transformation matrix
r	image spatial coordinates
t	translation transformation matrix
R(ϕ, θ, ψ)	rotation matrix
{S_{xy}, S_{xz}, S_{yz}}	shear parameters
{S_x, S_y, S_z}	scaling parameters
k, k'	k-space coordinates, before and after regridding
F, F'	k-space data, before and after regridding
RT	real-time
GS	gated-segmented
$n_{\text{cardphases}}$	number of reconstructed cardiac phases
det(A)	determinant of affine matrix
CC	correlation coefficient
$S_{\text{norm}}, Sh_{\text{norm}}$	normalized signal, normalized sharpness
ROI	region of interest
SAX	short axis view
ANOVA	analysis of variance
p	probability
FB	free-breathing

MCFB	motion-corrected free-breathing
BH	breath-hold
IVS	intraventricular septum
LV-PFW	left ventricle posterior free wall
LV-LFW	left ventricle lateral free wall
LV-AFW	left ventricle anterior free wall
ED	end diastole
ES	end systole
MC	mid-contraction

1 Introduction

Magnetic resonance imaging (MRI) is currently the gold standard for myocardial function assessment due to its high spatial resolution, excellent tissue contrast and reliable reproducibility. One drawback is that the acquisition time is still long, so respiratory motion from breathing will introduce blurring into the image. Breath-hold imaging is currently the method of choice due to its easy implementation, but it limits the acquisition time within which data can be acquired to the maximum duration of a breath-hold and excludes a portion of the population, including children and the very ill, who experience difficulty in holding their breath. Various techniques for respiratory gating have been tried, but all are slow and have certain amounts of dead time during which no data is acquired. Navigator techniques are inappropriate for cine imaging due to the time required to excite the tissue, acquire the navigator information and then re-establish the steady-state conditions for the primary imaging experiment. A method for free breathing motion correction called free-breathing cine-navigator imaging is presented in this thesis which will increase the duty cycle to 100%, correct the motion artifacts using only the k-space data itself, and allow imaging of previously excluded patient populations.

To refresh the reader's memory of MRI, chapter 2 will present MR physics and imaging concepts necessary to understand the rest of the thesis. Chapter 3 will introduce some previous methods of respiratory motion correction in the literature and other cardiac imaging considerations such as cardiac gating and cine-imaging.

The cine-navigator technique will be introduced and explained in chapter 4, with results and discussion presented in chapters 5 and 6 respectively. Chapter 5 will consist of a comparison between uncorrected, corrected free-breathing and gold-standard breath-hold images, and normalized sharpness profiling analysis will be performed as a quantitative measure of image quality and the effectiveness of motion correction. Chapter 6 will discuss the strengths and drawbacks of cine-navigator imaging and propose future steps for improvement and further development.

2 MR Physics and Imaging Basics

Where previously medical practitioners relied on indirect or invasive methods to diagnose disease, the development of tomographic imaging provided a means of directly viewing internal physical and chemical structures based on external detection of various properties of the human body. Transmission tomography such as x-ray and computed tomography (CT) relies on the attenuation of transmitted waves (x-rays) as it passes through the body, and diffraction tomography such as ultrasound relies on the reflection of acoustic pressure waves. Magnetic resonance imaging, on the other hand, is in an entirely different category. It does not measure the alteration in an externally applied wave but rather measures the change in an intrinsic property after external excitation. This property is called nuclear magnetic resonance (NMR).

2.1 NMR Phenomenon

In 1946, Felix Bloch and Edward Purcell independently discovered that magnetic nuclei in bulk matter could absorb radiofrequency energy when in the presence of a magnetic field and in turn produce a detectable signal [5, 44]. This is known as the nuclear magnetic resonance phenomenon.

2.1.1 Quantum Mechanical Properties

To understand what NMR is, an explanation of what makes nuclei magnetic is required. Each atomic nuclei possesses protons and neutrons in varying amounts, with the number

of protons determining the atomic number Z or static positive charge and the sum of the number of protons and neutrons determining the mass number A or nuclear mass of the nucleus. If either or both of the neutrons and protons are present in odd quantities, the nucleus possesses an angular momentum or spin. Although spin is a quantum mechanical property, it is represented as the nucleus rotating about its own axis in the classical vector model. As with any charged spinning object, a local magnetic dipole is generated. This is called the magnetic moment $\vec{\mu}$, and is represented by a vector (Figure 2.1).

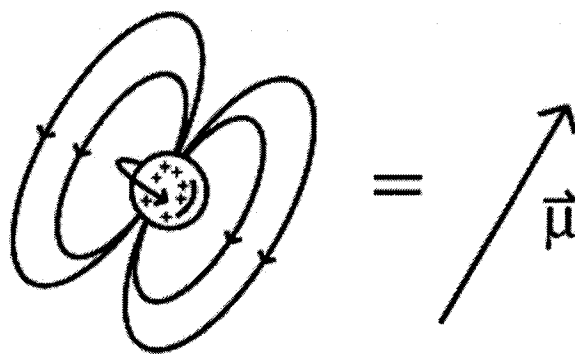


Figure 2.1 Representation of classical vector model. Left, spinning charged nuclei with magnetic field lines. Right, magnetic moment vector $\vec{\mu}$ represented as an arrow.

The spin angular momentum \vec{J} and the magnetic moment $\vec{\mu}$ are related to each other by a physical constant called the magnetogyric ratio γ , where:

$$\vec{\mu} = \gamma \vec{J} \quad (2.1)$$

This ratio is unique for every atomic nucleus. It is also commonly converted to frequency scale and renamed to γ :

$$\gamma = \frac{\gamma}{2\pi} \quad (2.2)$$

Some values for γ of useful nuclei for diagnostic imaging are given in Table 2.1.

\vec{J} is referred to as a quantified vector because it is only allowed discrete orientations. The spin angular momentum magnitude is given by:

$$\|\vec{J}\| = \hbar \sqrt{I(I+1)} \quad (2.3)$$

where \hbar is Planck's constant in frequency scale and I is another quantum mechanical property called the nuclear spin quantum number. I takes on only integer, half-integer and zero values such as:

$$I = 0, \frac{1}{2}, 1, \frac{3}{2}, 2, \frac{5}{2}, \dots \quad (2.4)$$

and is chosen based on the atomic mass and charge numbers. Odd mass numbers give half-integral spin, even mass and charge numbers give zero spin, and even mass but odd charge numbers give integral spin. Non-zero spin in turn gives rise to non-zero magnetic moment. Common nuclei like ^1H , ^{13}C , ^{19}F , ^{31}P have $I = \frac{1}{2}$, and are called spin- $\frac{1}{2}$ systems.

Isotope	Magnetogyric Ratio (MHz/T)	I (nuclear spin quantum number)
^1H	42.58	$\frac{1}{2}$
^3He	32.44	$\frac{1}{2}$
^{13}C	10.71	$\frac{1}{2}$
^{17}O	5.77	$\frac{5}{2}$
^{19}F	40.08	$\frac{1}{2}$

²³ Na	11.27	3/2
³¹ P	17.25	1/2

Table 2.1 Table of magnetogyric ratios for isotopes common in medical imaging, with I values.

2.1.2 Polarization

Undisturbed, the nuclei's magnetic moments are oriented randomly due to Brownian motion and cancel each other out, meaning there is no net magnetization at thermal equilibrium. When a strong uniform magnetic field \vec{B}_0 is applied, the magnetic moments orient themselves parallel and anti-parallel to the field direction, conventionally called the z-direction. The z-projection of the magnetic moment vector can only assume one of a set of discrete values, given by:

$$\mu_z = \gamma m_l \hbar \quad (2.5)$$

where m_l is the magnetic quantum number and can be any of $(2I+1)$ values as follows:

$$m_l = -I, -I+1, \dots, I \quad (2.6)$$

Thus there are $(2I+1)$ possible orientations for $\vec{\mu}$ with respect to the z-direction. In the case of a spin- $1/2$ system, there are 2 possible orientations, $-1/2$ and $1/2$, or parallel and anti-parallel. Speaking in terms of quantum mechanics, each of the orientations represents a different quantum state with different energy. The parallel orientation represents the quantum state with lower energy and thus is preferred, making the net magnetization oriented parallel with the external magnetic field (Figure 2.2). The process of aligning the

magnetic moments with \vec{B}_0 initializes the spin system for uniform response to external perturbation and is called polarization.

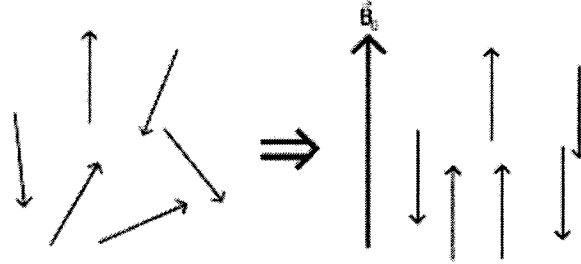


Figure 2.2 Left, randomly oriented magnetic moment vectors. Right, external field vector \vec{B}_0 and parallel/anti-parallel moment vectors for spin- $\frac{1}{2}$ system.

2.1.3 Energy Levels

Let's take a closer look at the energies of the quantum states. The interaction energy of the magnetic moment and the external magnetic field is given by:

$$E = -\vec{\mu} \cdot \vec{B}_0 = -\gamma \hbar B_0 \quad (2.7)$$

and the number of energy levels is the same as the number of possible spin quantum numbers. For a spin- $\frac{1}{2}$ system, the difference between the two energy levels is:

$$\Delta E = E_{\langle\beta\rangle} - E_{\langle\alpha\rangle} = \gamma \hbar B_0 \left(\frac{1}{2} - \left(-\frac{1}{2} \right) \right) = \gamma \hbar B_0 \quad (2.8)$$

This difference is referred to as the Zeeman splitting phenomenon (Figure 2.3).

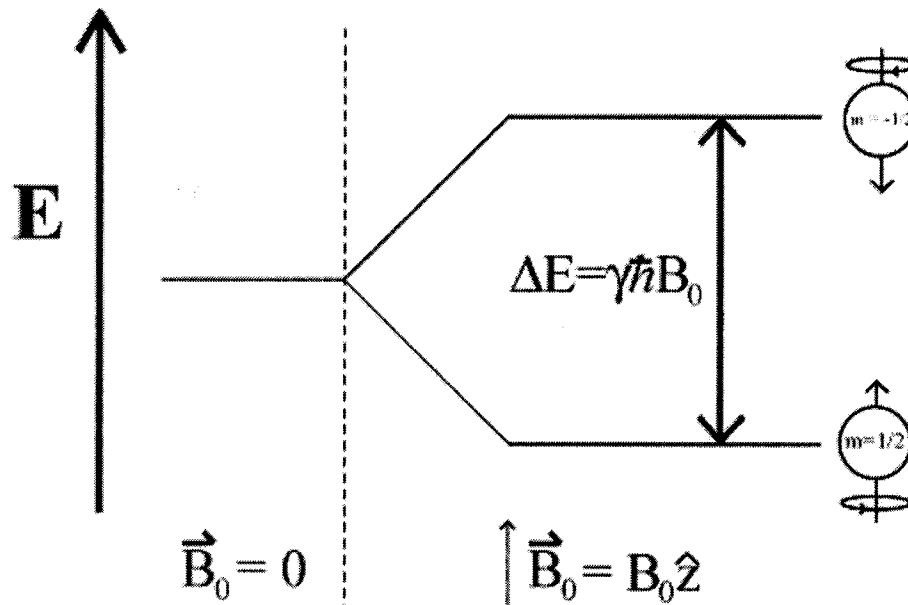


Figure 2.3 Zeeman splitting phenomenon for spin- $\frac{1}{2}$ system. When in the presence of \vec{B}_0 the spins will populate parallel and anti-parallel energy states ($m = -\frac{1}{2}, \frac{1}{2}$), with an energy level difference ΔE .

From thermodynamics, at a finite temperature T (given in Kelvins) both orientations will also have different spin populations as described by the Boltzmann relation:

$$n_{\uparrow} / n_{\downarrow} = e^{\frac{\Delta E}{k_B T}} \quad (2.9)$$

where n_{\uparrow} is the number of parallel spins, n_{\downarrow} is the number of anti-parallel spins, and k_B is the Boltzmann constant (1.38×10^{-23} J/K).

For protons (hydrogen) at room temperature (293 K) under a field strength of 1.5T, there are 0.001% more spins in the parallel rather than the anti-parallel orientation, resulting in a small net magnetization aligned with \vec{B}_0 . The small ratio precludes detection of individual magnetic moments but is adequate for the generation of a significant net

magnetization in a larger sample size, there being approximately 7×10^{22} protons for every mL of water.

2.1.4 Bulk Magnetization

The bulk or net magnetization is the sum of all the magnetic moments in the system. The xy-components of the magnetic moments sum to zero because they still have random orientation and cancel each other out. The magnitude of the spin- $\frac{1}{2}$ system z-component is given by:

$$M_z = \frac{\gamma^2 \hbar^2 B_0 N_s}{4 K T} \quad (2.10)$$

where N_s is the total number of spins in a system. For a general spin-I system, the equation becomes:

$$M_z = \frac{\gamma^2 \hbar^2 B_0 N_s I(I+1)}{3 K T} \quad (2.11)$$

The bulk magnetization can be increased by turning up the external field strength or decreasing the temperature of the object. In most clinical exams, decreasing the patient's body temperature is out of the question, and detection sensitivity increases with field strength roughly proportional to $B_0^{7/4}$.

2.1.5 Nuclear Precession

From classical mechanics, a magnetic field also applies torque on a classical magnetic moment vector. The torque is equal to the rate of change of the angular momentum, given by:

$$\frac{d\vec{J}}{dt} = \vec{\mu} \times \vec{B}_0 \quad (2.12)$$

which is related to the rate of change of magnetic moment by the gyromagnetic ratio:

$$\frac{d\vec{\mu}}{dt} = \gamma \vec{\mu} \times \vec{B}_0 \quad (2.13)$$

This is the classical equation of motion for isolated spins. The solution is given as:

$$\mu_{xy}(t) = \mu_{xy}(0) e^{-i\gamma B_0 t} \quad (2.14a)$$

$$\mu_z(t) = \mu_z(0) \quad (2.14b)$$

The torque applied is perpendicular to the plane containing the magnetic moment and the external field, so the vector precesses around the field direction (Figure 2.4). The direction of precession is given by the left-hand rule, where the thumb is held in the direction of \vec{B}_0 and the nuclear precession follows the direction of the fingers.

The angular frequency at which $\vec{\mu}$ precesses is called the Larmor frequency ω_0 , where:

$$\omega_0 = \gamma B_0 \quad (2.15)$$

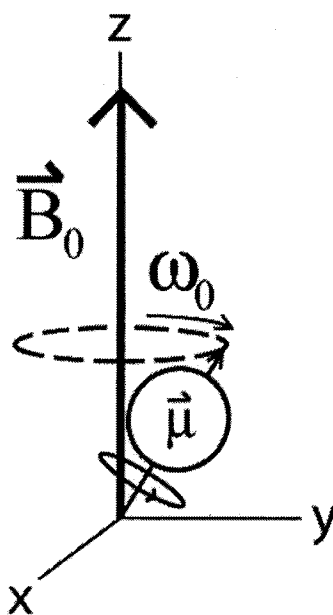


Figure 2.4 Precession of spin $\vec{\mu}$ about the longitudinal magnetic field \vec{B}_0 at Larmor frequency ω_0 . Direction of precession follows left-hand rule.

2.1.6 Transverse Excitation

In the previous section, the spin system has been polarized to create a uniform net magnetization \vec{M} aligned with the external magnetic field \vec{B}_0 . Since \vec{M} is grossly overmatched by \vec{B}_0 , there is no way to distinguish it along the longitudinal or z-direction; thus, the system must be excited such that the magnetization tips down into the transverse or xy-plane, where it can be detected.

If a radiofrequency (RF) pulse is applied with the same energy as ΔE , the energy difference between the spin- $\frac{1}{2}$ quantum states, the system's nuclei absorb the RF energy

and equalize the populations in each energy level. This behaviour is called resonance.

Recalling that the energy of a photon is given by:

$$E = h \cdot \nu_{rf} = \hbar\omega_{rf} \quad (2.16)$$

and combining this with Equation 2.8, we find that the RF pulse must have a frequency of:

$$\omega_{rf} = \gamma B_0 = \omega_0 \quad (2.17)$$

which turns out to be the Larmor frequency of the selected nuclei. The Larmor frequency is the natural resonant frequency unique to each nucleus, allowing imaging of separate spin systems without overlap.

As the nuclei move to the anti-parallel quantum state, the resulting magnetization is tipped down to the transverse plane. When \vec{M} is tipped down, it will have two components, one in the longitudinal direction M_z , and one in the transverse plane M_{xy} . Similar to nuclear precession for a single magnetic moment μ , a static longitudinal magnetic field $\vec{B}_z = (0,0,B_0)$ will apply a torque to M_{xy} , which will precess about the longitudinal axis at the Larmor frequency ω_0 .

How is this RF pulse generated? A secondary time-varying magnetic field $\vec{B}_1(t)$ is turned on that rotates in the same sense as the desired M_{xy} about the longitudinal axis and at the same resonant frequency as the target spins. The formal representation is given as:

$$\vec{B}_1(t) = B_1^e(t) \left[\cos(\omega_{rf} t + \phi) \hat{i} - \sin(\omega_{rf} t + \phi) \hat{j} \right] = B_1^e(t) e^{-i(\omega_{rf} t + \phi)} \quad (2.18)$$

where $B_1^e(t)$ is the envelope function and ϕ the initial phase angle, assumed to be zero for simplicity. The envelope function describes the shape and duration of the RF pulse, and will be discussed in a later section. $\vec{B}_1(t)$ has a time-varying rotating transverse component perpendicular to \vec{B}_0 and \vec{M} which, when the RF pulse is on resonance with the nuclei, will exert torque on \vec{M} and tip it away from the longitudinal direction.

After the excitation is terminated, the magnetization will tend to go back to equilibrium. The transverse magnetization will decay to zero and the longitudinal magnetization will return to M_0 , its equilibrium value. This relaxation can be utilized as a way of providing soft tissue contrast, discussed further in section 2.2.5.

By Faraday's law of induction, any rotating net magnetization will induce an electromotive force (EMF) in a coil positioned with its axis perpendicular to the longitudinal direction, say along the y-axis. This measured EMF signal is called the free induction decay (FID) and for a uniform spin system with Larmor frequency ω_0 , the FID will be a sinusoid oscillating at frequency ω_0 , modulated by a decay function (Figure 2.5). The sinusoid comes from the precession of the spin about its own axis, while the decay function is a result of relaxation. The Fourier transform of the FID or the spectrum is a delta function at ω_0 . Every magnetic nucleus has a unique spectrum which forms the basis for data used to reconstruct tomographical images.

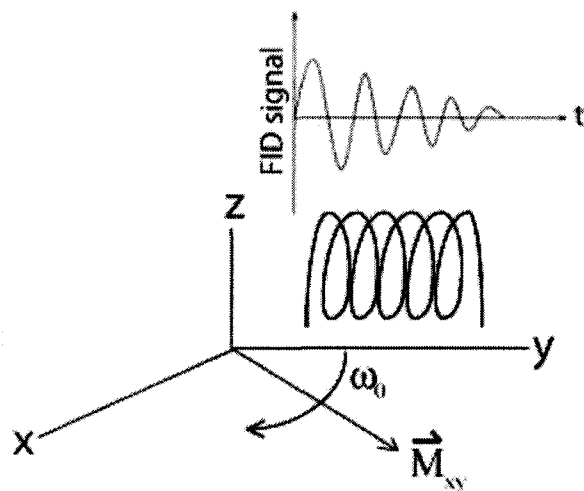


Figure 2.5 Illustration of precessing transverse magnetization M_{xy} inducing an FID signal in an RF coil placed along the y-axis. The signal decays away with time due to relaxation.

2.1.7 Nuclear shielding

Usually all spin systems have more than just one resonant frequency. Inhomogeneities in the background B_0 field can result in different Larmor frequencies for the same nuclei in different spatial locations. In molecular structures, nuclei can also be shielded from the effects of B_0 by interactions with different adjacent nuclei and their surrounding electrons. This phenomenon is called the chemical shift effect. Nuclei in homogenous B_0 but different molecular environments will have different resonant frequencies, allowing for the differentiation of different chemical structures. For example, fat will have a 3.35 ppm shift in Larmor frequency from water.

2.1.8 Bloch Equation & Rotating Frame of Reference

Mathematically, the system's behaviour under the influence of different magnetic fields, static or otherwise, can be described with what is known as the Bloch equation:

$$\frac{d\vec{M}}{dt} = \gamma \vec{M} \times \vec{B} - \frac{M_x \hat{i} + M_y \hat{j}}{T_2} - \frac{(M_z - M_z^0) \hat{k}}{T_1} \quad (2.19)$$

where $M_{x,y}$ are the transverse components, M_z^0 is the initial longitudinal magnetization as calculated by equation 2.10 or 2.11, and $T_{1,2}$ are the time constants that govern relaxation of the perturbed magnetization back to equilibrium conditions.

Since the transverse magnetization is rotating at a set frequency, a rotating frame of reference is applied in which the axes are rotating at the same frequency as the magnetization such that M_{xy} appears stationary. This makes it conceptually easier to describe the effect of excitation on the magnetization. To mathematically illustrate the simplification, the equation of motion for the system will now include both \vec{B}_0 and $\vec{B}_1(t)$:

$$\frac{d\vec{M}}{dt} = \gamma \vec{M} \times \vec{B} = \gamma \vec{M} \times \left(\vec{B}_0 \hat{k} + B_1 \cos \omega t \hat{i} + B_1 \sin(\omega t) \hat{j} \right) \quad (2.20)$$

This equation of motion comes from the Bloch equation under the assumption that it describes the behaviour of \vec{M} only during excitation, and that the RF pulse duration is short compared to T_1 and T_2 . It is analogous to the equation of motion for an individual magnetic moment in equation 2.13.

The x-, y-, and z-components thus become:

$$\frac{dM_x}{dt} = \gamma (M_y B_0 - M_z B_1 \sin(\omega t)) \quad (2.21a)$$

$$\frac{dM_y}{dt} = \gamma (M_z B_1 \cos(\omega t) - M_x B_0) \quad (2.21b)$$

$$\frac{dM_z}{dt} = \gamma (M_x B_1 \sin(\omega t) - M_y B_1 \cos(\omega t)) \quad (2.21c)$$

To switch from the laboratory to the rotating frame of reference, the following conversion is used:

$$\hat{i}_\rho = \cos(\omega t) \hat{i} - \sin(\omega t) \hat{j} \quad (2.22a)$$

$$\hat{j}_\rho = \sin(\omega t) \hat{i} + \cos(\omega t) \hat{j} \quad (2.22b)$$

$$\hat{k}_\rho = \hat{k} \quad (2.22c)$$

where ω is the frequency of rotation and the rotating frame directional vectors are denoted by ρ . Note that only the transverse components rotate, while the longitudinal component remains the same. Applying this conversion to M_x and M_y :

$$M_{x\rho} = M_x \cos(\omega t) + M_y \sin(\omega t) \quad (2.23a)$$

$$M_{y\rho} = -M_z \sin(\omega t) + M_y \cos(\omega t) \quad (2.23b)$$

where $M_{x\rho}$ and $M_{y\rho}$ are the new transverse components of \vec{M}_ρ in the rotating frame. After differentiation and substitution into 2.21a-c, the following is obtained:

$$\frac{dM_{x\rho}}{dt} = (\gamma B_0 + \omega) M_{y\rho} \quad (2.24a)$$

$$\frac{dM_{y\rho}}{dt} = -(\gamma B_0 + \omega) M_{x\rho} + \gamma B_1 M_{z\rho} \quad (2.24b)$$

$$\frac{dM_{z\rho}}{dt} = -\gamma B_1 M_{y\rho} \quad (2.24c)$$

It is seen that the rotation about the longitudinal axis has been removed and instead of the time-dependent combination of \vec{B}_0 and $\vec{B}_1(t)$, there is a static effective magnetic field:

$$\vec{B}_{eff} = B_1 \hat{k}_p + (B_0 + \omega / \gamma) \hat{k}_p \quad (2.25)$$

such that:

$$\frac{d\vec{M}_p}{dt} = \gamma \vec{M}_p \times \vec{B}_{eff} \quad (2.26)$$

which is the rotating frame's analogue to the laboratory frame's equation of motion in 2.20. B_1 is now a static magnetic field perpendicular to the longitudinal axis, and the longitudinal magnetization is B_0 plus some off-resonant field component ω/γ . \vec{M}_p precesses in a cone about \vec{B}_{eff} , that is incident upon the longitudinal axis. When the RF pulse is exactly on resonance with the spin system, the effective field is \vec{B}_1 alone and \vec{M}_p precesses about the x_p axis at a frequency of $\omega_1 = \gamma B_1$, as in Figure 2.6.

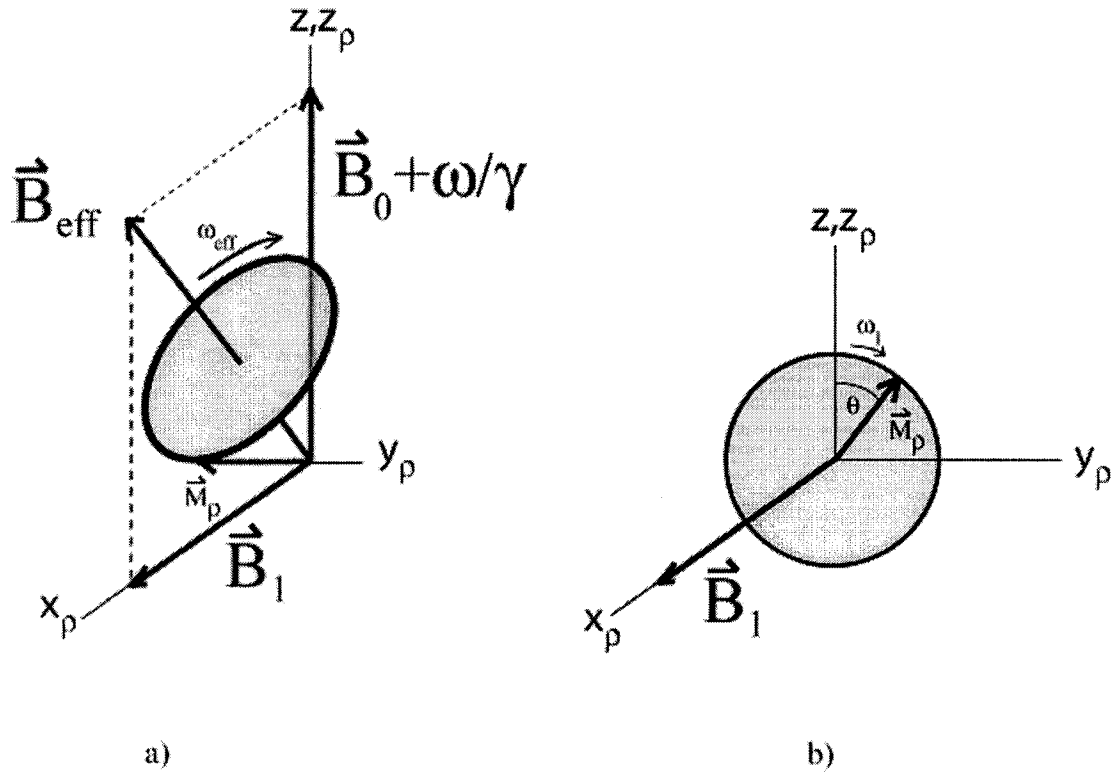


Figure 2.6 Rotating frame of reference. a) In the general case, \vec{M}_p rotates in a cone of precession about B_{eff} at frequency ω_{eff} . b) When the resonance condition is fulfilled, \vec{M}_p precesses about B_1 at frequency ω_1 . The flip angle θ is measured from the positive z-axis and depends on the strength and duration of the excitation RF pulse.

2.1.9 Flip Angle

The forced precession about B_1 tips the bulk magnetization away from the z-axis, and creates a measurable transverse component $M_{xy,p}$. The angle that \vec{M}_p forms with the longitudinal axis is called the flip angle (see Figure 2.6), and depends on the strength and duration t_{RF} of the RF pulse. For a rectangular RF pulse, it can be calculated as follows:

$$\theta = \omega_{eff} t_{rf} = \gamma B_1 t_{rf} \quad (2.27)$$

To place the magnetization squarely in the transverse plane, a flip angle of 90° or $\pi/2$ is applied, making $t_{RF} = (\pi/2)/\gamma B_1$. This results in maximal signal along the y_ρ -axis, where the RF receiver coil is located. If the RF pulse is left on for double that amount of time, as with a 180° or π pulse, the magnetization will be pushed down to the negative z -axis or inverted, and there will be no transverse magnetization.

2.1.10 Relaxation

After the excitation is stopped, the magnetization will slowly “relax” back to equilibrium conditions. This relaxation occurs in two separate ways, the return of the longitudinal magnetization back to equilibrium or M_0 and the decay of the transverse magnetization. The following describes the relaxation behaviour as well as how to measure the relaxation time constants using combinations of RF pulses.

2.1.10.1 Longitudinal Relaxation

The longitudinal relaxation is governed by interactions between the nuclear spins and their surrounding environment, which consists of unexcited nuclei and the surrounding electric fields. These are collectively known as the “lattice” and so the process is called spin-lattice relaxation. The spins begin to go back to equilibrium conditions as governed by the Boltzmann relation in equation 2.9. It can be described by a first-order rate equation:

$$\frac{dM_{z\rho}}{dt} = -\frac{M_{z\rho} - M_z^0}{T_1} \quad (2.28)$$

where T_1 denotes the time at which M_z is restored to 63% of M_z^0 . The solution to this equation for biological tissue is given as:

$$M_{zp}(t) = M_0 \left(1 - e^{-\frac{t}{T_1}} \right) + M_{zp}(0_+) e^{-\frac{t}{T_1}} \quad (2.29)$$

where $M_{zp}(0_+)$ is the longitudinal magnetization immediately after the RF pulse. It shows an exponential dependence on time, as seen in Figure 2.7, with different starting points depending on the flip angle.

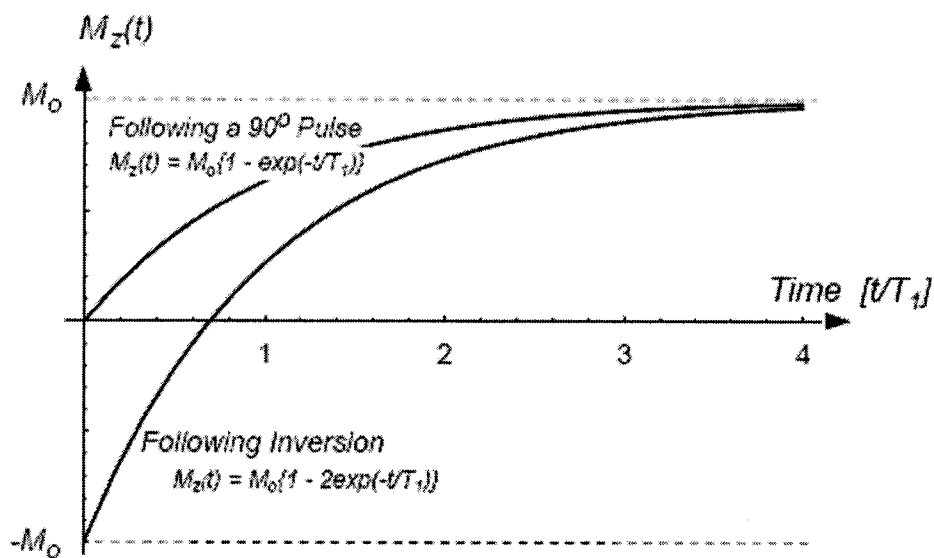


Figure 2.7 Longitudinal relaxation curves for 90° and 180° pulses[58].

To measure T_1 , an inversion-recovery experiment is undertaken. A 180° pulse is applied that tips the magnetization to the negative longitudinal axis, and allowed to decay over a time τ . A 90° pulse then tips the magnetization to the transverse plane for immediate acquisition of an FID signal. Varying τ and acquiring the corresponding FIDs gives a

time-dependent relaxation function as seen above in the inversion case, for which the time constant T_1 can be calculated.

2.1.10.2 Transverse Relaxation

The transversal relaxation is governed by interactions between the excited nuclei, and is called spin-spin relaxation. In a real system, each spin will experience a slightly different magnetic field due to local fields from neighbouring nuclear dipoles and electrons, so individual spins will precess at slightly different frequencies. These magnetization vectors destructively interfere with each other and thus cause an irreversible dephasing, decreasing the overall transverse magnetization to zero. It is also described by a first-order rate equation:

$$\frac{dM_{xy}}{dt} = -\frac{M_{xy}}{T_2} \quad (2.30)$$

where T_2 denotes the time at which the transverse magnetization has decayed to 37% of its initial value. Note that both equations are derived from the rotating frame Bloch equation in which \vec{B}_{eff} is zero, as $\vec{B}_1(t)$ has been turned off and the other term goes to zero if the resonance condition is satisfied. The solution is:

$$M_{xy}(t) = M_{xy}(0_+) e^{-\frac{t}{T_2}} \quad (2.31)$$

where $M_{xy}(0_+)$ is the initial transverse magnetization immediately after the RF pulse.

This shows an exponential decay to zero, as seen below.

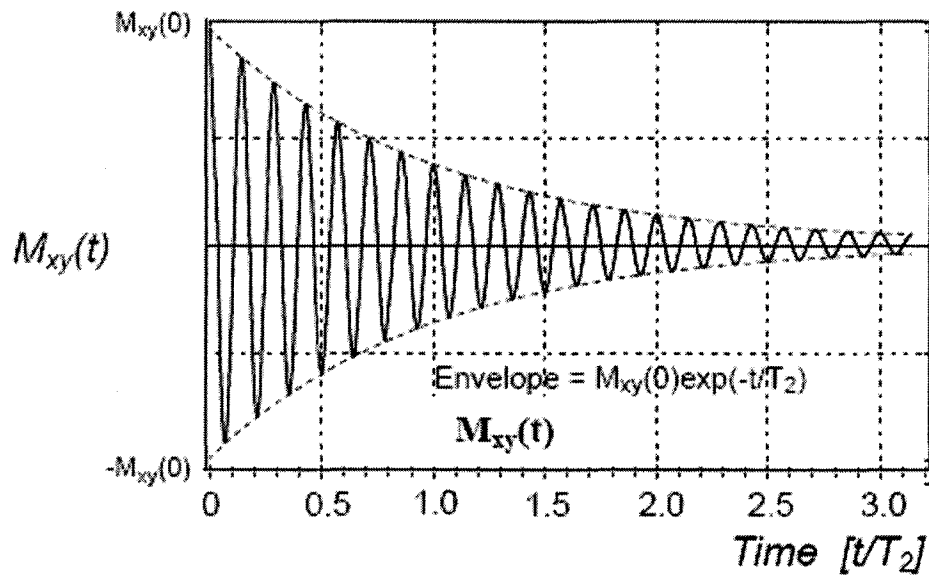


Figure 2.8 Transverse relaxation curve, showing transverse magnetization decay over time [58].

Transverse relaxation depends both on the spin-lattice interactions, which push the spin vectors from the transverse plane back to the longitudinal axis, and the additional dephasing of the spin vectors in the transverse plane, so T_2 values are always shorter than the T_1 values. Relaxation times for biological subjects are dependent on tissue composition, structure and surroundings, which provide a means for developing contrast between different tissues. This is further discussed in section 2.2.5.

Another source of dephasing is static inhomogeneities in the background \vec{B}_0 field caused by imperfections in magnet design and construction. These inhomogeneities cause the spin vectors to precess at slightly different frequencies, and over time the vectors will be spread out over the transverse plane. The decay of the transverse magnetization is hastened and the overall time constant T_2^* is given as:

$$\frac{1}{T_2^*} = \frac{1}{T_2} + \frac{1}{T_2'} \quad (2.32)$$

where T_2' is the time constant for the dephasing from static inhomogeneities alone. The equation governing the decay of the detected signal $S(t)$ is thus:

$$S(t) = S(0) e^{-\frac{t}{T_2^*}} \quad (2.33)$$

Unlike spin-spin relaxation, inhomogeneity-based dephasing can be reversed by applying a refocusing RF pulse, as in Figure 2.9. After an initial 90_z° pulse that tips the magnetization into the transverse plane, the spin vectors will eventually dephase, some precessing faster than others. If a transverse 180_x° refocusing RF pulse is applied along, say, the x_ρ -axis, the spins are flipped over that axis and now travel towards a common point on the y_ρ -axis. The once-decayed FID signal grows back to its original value in a certain time τ , at which point another measurement can be made. The second FID response is called a *spin-echo*, which was discovered by Erwin Hahn in 1950 [19].

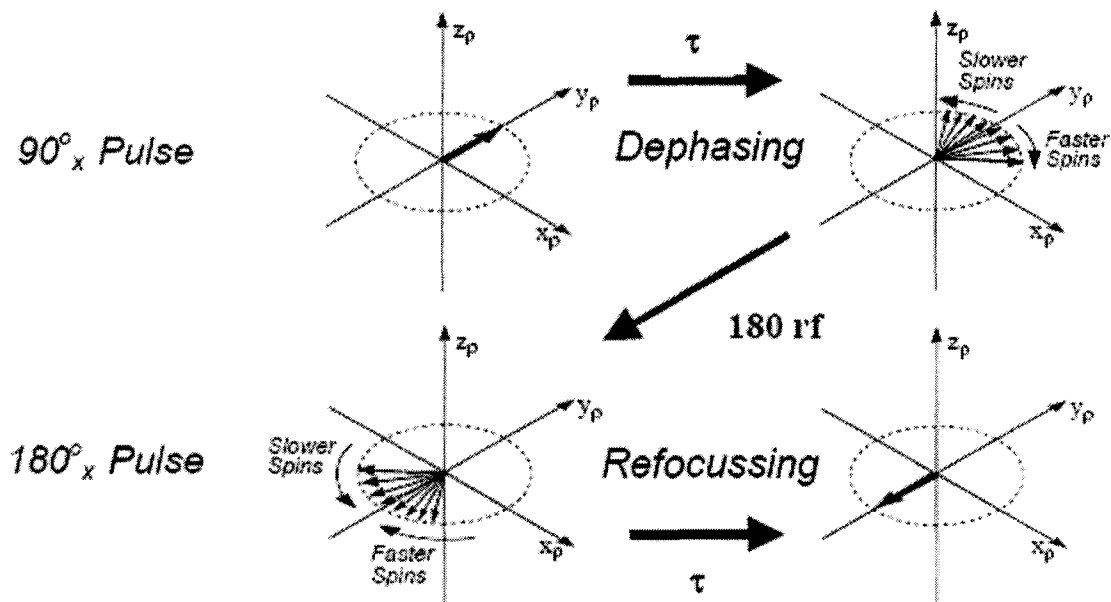


Figure 2.9 Spin-echo generation. The dephasing transverse magnetization is refocused by applying a 180°_x pulse that flips the spins over the x_p -axis. After a time τ , the spins meet up again on the opposite side of the y_p -axis, generating a second FID signal called the spin-echo [58].

After the refocusing pulse, the spins will immediately start to dephase again. Repeating the 180° refocusing pulses once the signal fades will continue to refocus the spins at a time interval known as the echo time (TE), which is designated as the time from the refocusing pulse to the occurrence of the spin-echo. The signal will continue to decay because of spin-spin relaxation, but the influence from static magnetic field inhomogeneities is eliminated, thus allowing the measurement of T_2 , which is an intrinsic property of the nuclei themselves.

2.2 Imaging Basics

Paul Lauterbur first applied the principles of NMR to creating a 2-D image in 1973, calling it zeugmatography. After applying what is now called a field gradient to the background magnetic field, he was able to relate the spin's Larmor frequency to its

spatial location [27]. About the same time, Peter Mansfield was able to use time-dependent gradient waveforms to create rapidly repeated spin-echoes for high-speed imaging [29]. Lauterbur and Mansfield are recognized as the forefathers of modern MR imaging. The following section will explain how to detect the spatial location of spins in 3D space and some different methods used to provide contrast.

2.2.1 Gradients

For a homogenous \vec{B}_0 field, the entire spin system of the selected nuclei will display one resonant frequency in the spectrum, but there is no way of telling where the individual spins are in the spatial domain. This problem is solved by varying the magnetic field such that each spatial location's spins will precess at a different Larmor frequency. Additional gradient magnetic fields increase or decrease the main magnetic field by a certain amount depending on the distance from the iso-center of the magnet.

For each direction, there will be a field gradient that varies linearly with position. The strength of these gradients are expressed as the slope of the generated field, in units of G/cm = 10 mT/cm. The effective field B along, say, the x-axis is calculated as:

$$B = B_0 + G_x x \tag{2.34}$$

where G_x is the gradient slope along the x-axis and x is the distance from the iso-centre along the x-axis (Figure 2.10). The Larmor frequency of the spin at that location is now:

$$\omega_{eff} = \gamma (B_0 + G_x x) = \omega_0 + \gamma G_x x \quad (2.35)$$

and is directly related to its spatial location. For the y and z axes, simply replace G_x and x with their analogues in the other directions.

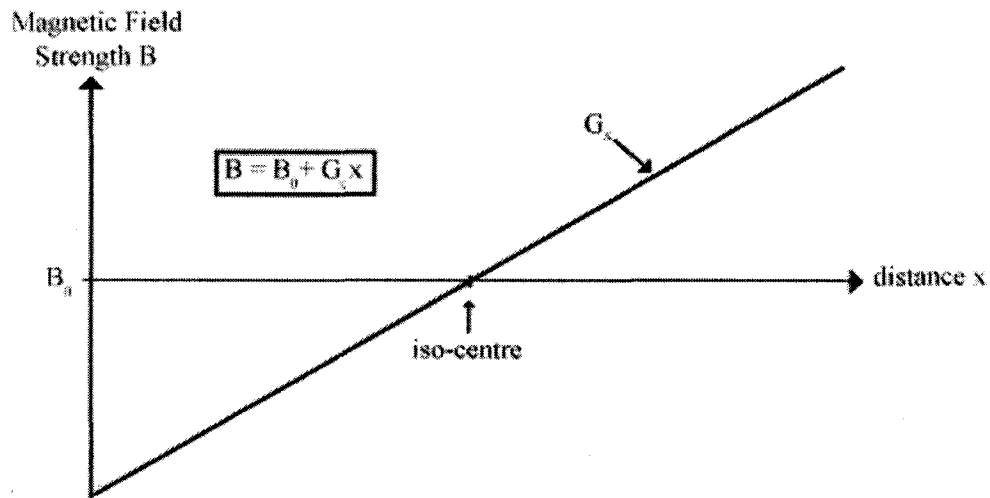


Figure 2.10 Plot of magnetic field strength B versus distance x from the iso-centre of the magnet while a linear gradient G_x is applied. Gradient strength is zero at iso-centre (effective field is B_0).

In the laboratory frame of reference, each spin will precess at a frequency offset from ω_0 by a fixed amount. In the rotating frame of reference, the spin vectors will be rotating at different frequencies ω in the transverse plane, and in the positive or negative sense about the z-axis depending on if ω_{eff} is faster or slower than ω_0 . The angle that they rotate from the x-axis in a given amount of time t is called the phase angle ϕ of those particular spins:

$$\phi = \omega t = \gamma G_x t \quad (2.36)$$

For a spin rotating in the negative sense about the z-axis, its phase will also be negative, as seen below.

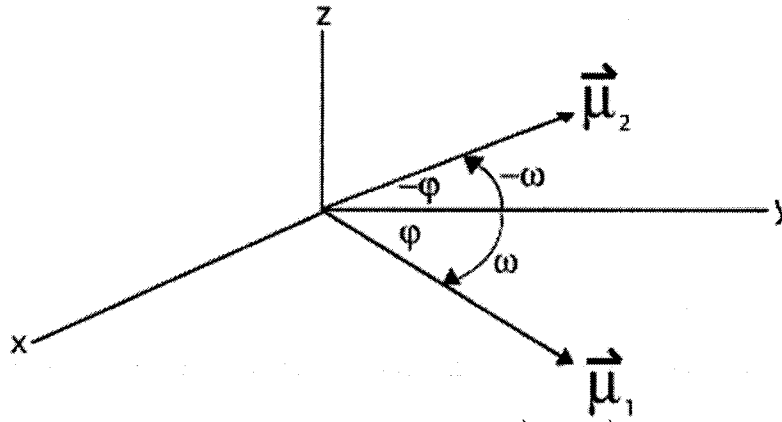


Figure 2.11 After excitation, spin vectors $\vec{\mu}_1$ and $\vec{\mu}_2$ precess away from the y-axis and accumulate a phase angle ϕ , dependent on the spin's frequency ω and precession time.

Gradient performance is often the limiting factor for any imaging procedure. The slew rate of a given gradient coil is a measure of the gradient coil performance, and is calculated as:

$$SR = \frac{G_{\max}}{t_{\text{rise}}} \tag{2.37}$$

where SR is the slew rate (T/m/s), G_{\max} is the peak gradient strength, and t_{rise} is the rise time or the time it takes the gradient amplitude to reach its maximum value.

2.2.2 Slice Selection

The first step is to isolate an imaging plane in a single direction. As previously explained, to excite the target nuclei, the RF pulse must have the same frequency as their resonant frequency, but if a gradient normal to the slice plane is present, the frequency of the RF pulse also determines the location of the slice. It can be summed up in the following equation:

$$\omega(z) = \omega_0 + \omega_z = \gamma(B_0 + G_z z) \quad (2.38)$$

where $\omega(z)$ is the frequency corresponding to the spatial location at distance z from the isocentre of the gradient G_z and ω_z is the offset frequency from the base Larmor frequency ω_0 . The frequency bandwidth $\Delta\omega_{RF}$ of the RF pulse will determine the slice width Δz as follows:

$$\Delta\omega_{rf} = \gamma G_z \Delta z \quad (2.39)$$

The flip angle is calculated as the area under the RF pulse envelope function:

$$\theta = \int_{-\infty}^{\infty} B_1 d\tau \quad (2.40)$$

One of the flexibilities of MRI is that any arbitrary axis can be used to select an imaging plane, using alternate or a combination of gradients. Generally, imaging planes are

defined along the x-, y-, and z-axes, but they can be selected to conform to a specific object's geometry, such as the heart.

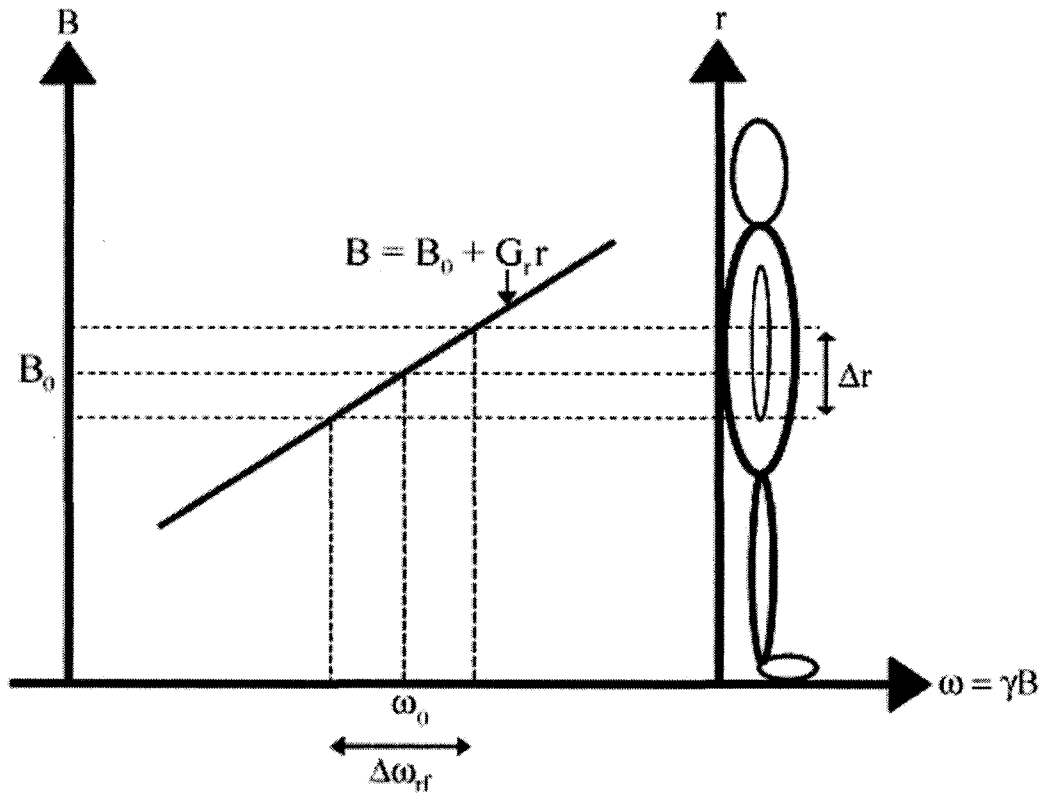


Figure 2.12 Slice selection on an arbitrary r-axis involving the spatial encoding of spin frequency ω by a linear gradient G_r . The slice width Δr is determined by the RF pulse bandwidth $\Delta\omega_{RF}$.

The application of the slice select gradient introduces a linear phase shift across the slice width resulting in dephasing of the transverse magnetization, so it is standard procedure to apply a rephasing gradient immediately after excitation to refocus the spins. The rephasing lobe must be opposite in polarity and have half the area of the initial slice select gradient, as seen in Figure 2.13.

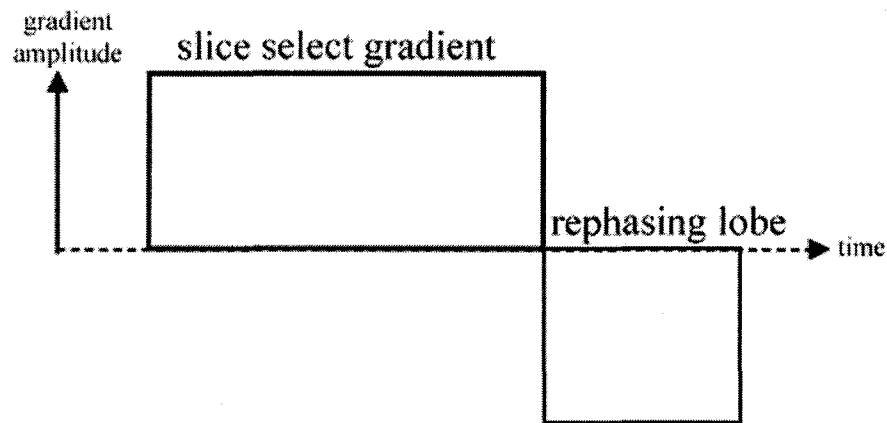


Figure 2.13 Rephasing lobe which is half the total area of the slice select gradient.

The frequency bandwidth is modulated by choosing the envelope function of the RF pulse. Ideally, in the frequency domain, the desired profile will be as close to a rectangle as possible, so the time domain RF pulse envelope will be as close to its Fourier pair, a sinc function, as possible. In practice, it is impossible to generate the infinite extent of a sinc pulse, so a truncated sinc envelope function is used which produces oscillations or ripples in the excitation profile, and decreases the cut-off steepness. More advanced envelope functions can be used, such as those which modulate the phase as well as the amplitude of the excited magnetization, or those that are calibrated to refocus the magnetization themselves.

2.2.3 Frequency and Phase Encoding

Post-excitation, the spins will precess freely in the transverse plane. Spatial information about spin location within the slice can be found through manipulation of two aspects, the frequency and the phase of the spins.

For frequency encoding, the frequency at which the spins precess about the longitudinal axis can be made to reflect spatial location with the application of a gradient along the transverse plane. Through combinations of different x- and y-gradients, the effective gradient can go along any angle through the object. When Lauterbur demonstrated MR imaging in 1973, he varied the frequency encode (FE) gradient direction and obtained projections at various angles, which were then back-projected to attain an image of the original object. This method is called projection reconstruction (PR), and its application to this project will be discussed in section 2.3.

The RF coil detects the FID signals of all the spins over the entire object at the same time. The resultant signal, influenced by frequency encoding along the x-axis, is given by:

$$S_{fe}(t) = e^{-i\gamma B_0 t} \int M_{xy}(x) e^{-i\gamma G_x x t} dx \quad (2.41)$$

and in the rotating frame of reference, the static B_0 term is eliminated. This resembles the Fourier transform relation, such that the original spatially encoded magnetization $M_{xy}(x)$ can be returned as:

$$M_{xy}(x) = \gamma G_x \int S_{fe}(t) e^{i\gamma G_x x t} dt \quad (2.42)$$

using $\gamma G_x t$ as the conjugate for the spatial variable x . The magnetization is proportional to spin density $\rho(x)$ by an invariable scaling constant, so the spatial map generated could represent one or the other.

To obtain information about the second transverse dimension, a different gradient is applied orthogonal to the FE gradient, a concept introduced by Edelstein in 1980 which is not used in any other imaging modality [12]. While the phase-encode (PE) gradient is on, the spins' precessional frequencies are altered, and the spins will accumulate phase according to equation 2.36, in which the phase depends on the spatial location of the spin and the duration of the gradient pulse. After the PE gradient is turned off, the spins will return to their base Larmor frequency, but the signal will be spatially encoded by the phase angles of the spins, and is thus called phase-encoded.

The resulting signal for phase-encoding along the y-axis is given as:

$$S_{pe}(t) = e^{-i\gamma B_0 t} \int M_{xy}(y) e^{-i\gamma G_y y T_{pe}} dy \quad (2.43)$$

where T_{pe} is the duration of G_y , and once again the static B_0 term is removed by transferring the equation into the rotating frame of reference. If phase-encoding is done alone, the result is all the spins rotating at the same precessional frequency with an initial phase angle determined by the location of the spins along the y-axis. The phase angle can be adjusted by increasing the PE gradient amplitude or altering the duration of the pulse, but for efficient imaging the former is more commonly practiced. The frequency of variation of phase will determine the location of the spins along the y-axis.

After frequency and phase encoding, both the frequency and phase of each spin are dependent on its spatial location within the 2D slice. The FE and PE gradients cannot be

turned on simultaneously, or it would simply result in a frequency-encoded projection along the effective gradient axis. Generally, the PE gradient is applied prior to the FE gradient such that the data is acquired for a projection parallel to the x-axis at a specific location along the y-axis. To acquire a full dataset, the PE gradient amplitude is varied while holding the FE gradient steady for each acquisition readout. Gradient-time waveforms illustrating the implementation of the pulse sequence are given in section 2.2.6.

2.2.4 K-space Formalism

The FID is decomposed into its component frequencies by taking the Fourier transform of the signal, which returns both real and imaginary components, preserving the phase information. The 2D frequency map can be taken as a direct spatial map of spin location, due to the linearity of the gradients. Thus the magnitude of the frequency components can be taken as an indication of nuclear density and converted to a gray-scale intensity map, where each pixel value represents the amount of the target nuclei present in that region.

The domain in which the FID is acquired is conventionally called k-space, with the frequency encode direction named the k_x -axis, the phase encode direction the k_y -axis, and the slice-select dimension the k_z -axis. This formalism greatly simplifies the Fourier analysis of the signal. K-space can also be thought of as the spatial domain's spatial frequency counterpart. The centre of k-space or low-frequency components hold the majority of the image intensity and contrast information, while the edges or high-frequency components have to do with edges and sharpness.

Transformation of the frequency-encoded time domain signal $S_{fe}(t)$ into the k-space domain requires the following substitution into 2.41:

$$k_x = \frac{\gamma}{2\pi} G_x t \quad (2.44)$$

such that the signal can now be written as:

$$S_{fe}(k_x) = \int M_{xy}(x) e^{-i2\pi k_x \cdot x} dx \quad (2.45)$$

Similarly, for the phase-encoded signal, the conversion used is:

$$k_y = \frac{\gamma}{2\pi} G_y T_{pe} \quad (2.46)$$

such that the signal is now given by:

$$S_{pe}(k_y) = \int M_{xy}(y) e^{-i2\pi k_y \cdot y} dy \quad (2.47)$$

In real life, the raw data is sampled discretely and uniformly over a finite extent of k-space. This is referred to as the sampling trajectory. For simplicity, the following will refer to only the rectangular grid or Cartesian sampling, with discussion of the PR trajectory put off until section 2.3. In the phase-encode direction, this translates into varying the gradient amplitude by discrete amounts (ΔG_y), while in the frequency-encode direction the signal is sampled at points separated by a uniform time interval Δt .

Thus the distance $\Delta k_{x,y}$ between raw data points in k-space is given respectively by:

$$\Delta k_x = \gamma |G_x| \Delta t \quad (2.48a)$$

$$\Delta k_y = \gamma \Delta G_y T_{pe} \quad (2.48b)$$

The Nyquist sampling criterion states that to be able to fully reconstruct a frequency-band-limited signal from its sampled data values, the sampling interval Δt must be:

$$\frac{1}{f_s} = \Delta t \leq \frac{1}{2f_{\max}} \quad (2.49)$$

where f_s is the sampling rate and f_{\max} is the frequency bandwidth of the signal. If the sampling interval is any higher than this value, the reconstructed signal will suffer from aliasing or overlap of signal replicas. Applying this to MRI, the separation in k-space is related to the field of view (FOV) in the spatial domain by:

$$\Delta k_{x,y} \leq \frac{1}{FOV_{x,y}} \quad (2.50)$$

Conversely, the spacing between image points (Δx) or the spatial resolution of the image is determined by the extent of the raw dataset or the spatial frequency bandwidth FOV_k :

$$\Delta x \leq \frac{1}{FOV_k} \quad (2.51)$$

Combining equations 2.47 and 2.49 returns the sampling requirements for an object with dimensions FOV_x by FOV_y :

$$\Delta t = \frac{2\pi}{\gamma |G_x| FOV_x} \quad (2.52a)$$

$$\Delta G_y = \frac{2\pi}{\gamma T_{pe} FOV_y} \quad (2.52b)$$

K-space and the spatial domain are now related by the discrete Fourier transform, as given by:

$$M(p\Delta x, q\Delta y) = \sum_{m=-\frac{N}{2}}^{\frac{N}{2}-1} \sum_{n=-\frac{N}{2}}^{\frac{N}{2}-1} S(m\Delta k_x, n\Delta k_y) e^{-i\left(\frac{2\pi mp}{N} + \frac{2\pi nq}{N}\right)} \quad (2.53)$$

where N is the k-space FOV, assumed to be the same for both dimensions, divided by the sampling interval $\Delta k_{x,y}$, also assumed to be identical for both dimensions:

$$N = \frac{FOV_k}{\Delta k} \quad (2.54)$$

Combining this with equation 2.50 gives us the number of returned image pixel points along a single dimension as identical to the number of points along a single dimension in k-space, N :

$$\frac{FOV_x}{\Delta x} = \frac{1/\Delta k}{1/N\Delta k} = N \quad (2.55)$$

2.2.5 Contrast Mechanisms

The gray-scale intensity of the pixels represents the strength of the transverse magnetization detected. Contrast is thus defined as the difference between gray-scale levels corresponding to the difference in magnetization strength. The greater the difference, the better the human eye can distinguish different features within the object. With transmission tomography, contrast is sometimes achieved through injection of contrast agent such as a dye or air that enhances the scattering effect of the tissue. This contrast mechanism is exogenous and can rarely result in morbidity or even mortality. With MRI, properties inherent to the tissue are manipulated for endogenous contrast mechanisms, and the exogenous paramagnetic contrast agent has shown less morbidity than the agents for CT [58].

The most basic tissue property is the spin density of the specific nuclei in the system, which is directly proportional to the amount of magnetization derived from equation 2.52. Usually proton spin density is measured for biological systems, but there is not much difference in the water content of different tissues. A better method of contrast enhancement is relaxation, where the relaxation times differ depending on the interaction of water with the molecular environment and cellular structure of the tissue. Structures in which the water is unable to freely move generally have lower $T_{1,2}$ values than more fluidic environments such as cerebrospinal fluid. The shorter relaxation times means the magnetization will recover more quickly towards equilibrium conditions, and a difference in magnetization signal strength will evolve over time, as in Figure 2.14.

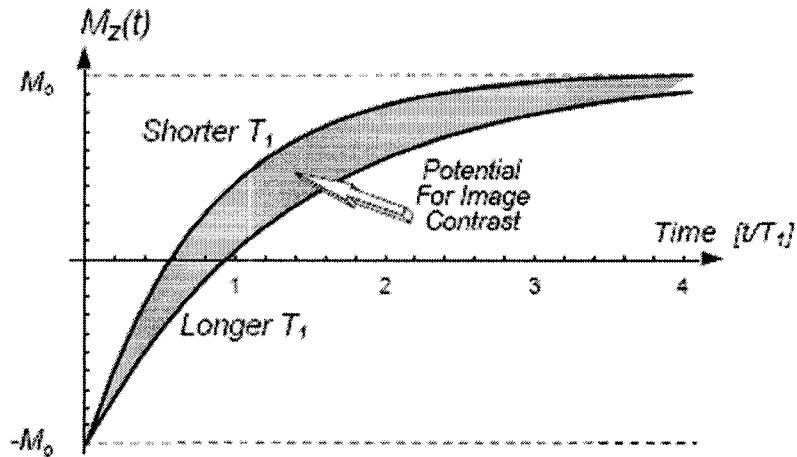


Figure 2.14 T_1 relaxation contrast mechanism. Tissues with different T_1 values will have different longitudinal magnetization amounts after a time t . The larger the difference in magnetization, the more image contrast obtained [58].

Different contrast agents can be used to either enhance T_1 or T_2 contrast. The use of paramagnetic contrast agent gadolinium diethylenetriamine pentetate (Gd-DTPA) decreases the T_1 relaxation time, while super-paramagnetic iron oxide (SPIO) particles distort the spins' local magnetic field and accelerate transverse dephasing, decreasing T_2 .

2.2.6 Pulse Sequences

A pulse sequence is the combination and timing of field gradients and RF pulses that acquires k-space data in a specific manner, depending on the purpose of the imaging experiment. The following section will describe the most common pulse sequences used, including spin-echo (SE), gradient-echo (GRE), and steady-state free precession (SSFP).

2.2.6.1 Spin-Echo

As in section 2.1.10.2, the spin-echo is a secondary signal that arises from the rephasing of the transverse magnetization. The initial 90_z° excitation pulse is applied simultaneously with a slice-select gradient G_z to tip the spin vectors into the transverse plane. Immediately after the excitation pulse is turned off, a rephasing lobe is applied to refocus the spins within the slice. As can be seen in Figure 2.15, the phase encode gradient is incremented as described in section 2.2.3, while the frequency encode gradient application is a little more complex. To ensure that the centre pixel of the k-space dataset corresponds to the centre of the acquisition period of the FID signal, an FE preparation gradient is applied, which has half the area of the actual readout gradient. The spins acquire FE gradient-dependent phase that is reversed after the 180_x° refocusing pulse. The readout gradient then rephases the spins such that the maximum amplitude of the FID occurs at the centre of the acquisition period, after which the FID will decay away once again. The period between the excitation pulse and the spin-echo is labeled the echo time (TE), while the period between each excitation pulse is called the repetition time (TR).

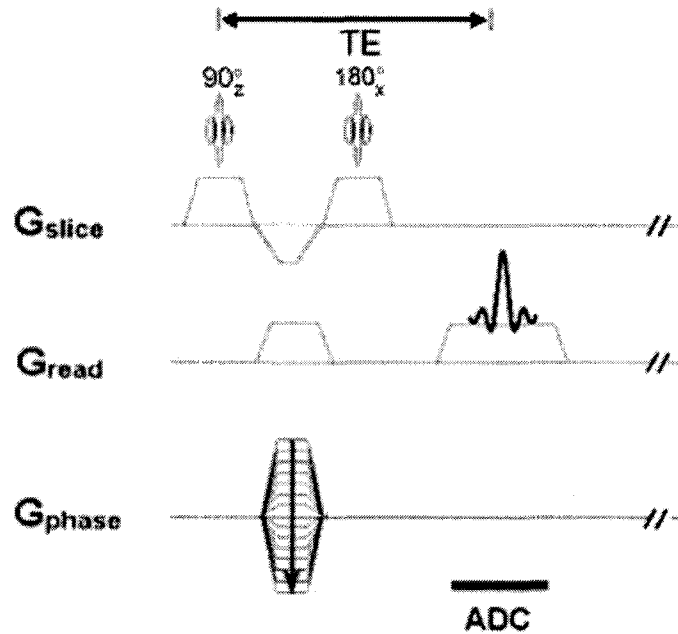


Figure 2.15 Spin-echo pulse sequence. After the 90_z° excitation RF pulse, the spins are dephased by a preparation FE gradient, then flipped over the x-axis by the 180_x° pulse. This creates a spin echo signal in the middle of the acquisition period. G_{slice} , slice-select gradient; G_{read} , readout gradient; G_{phase} , phase-encode gradient; ADC, analog-to-digital converter; TE, excitation time. Adapted from [15].

Depending on the TE/TR ratio, the image contrast can be altered to depend on any of the mechanisms described in section 2.2.5. For a long TR ($>3T_1$) and short TE, all the tissues' longitudinal magnetization reaches full relaxation prior to the next excitation pulse, and the image contrast relies solely on spin density. A short TR prevents complete longitudinal relaxation, and the recovered magnetization amplitude will depend on T_1 . Conversely, when a long TE is used, the transverse magnetization has more time to relax and differences in signal amplitude develop based on T_2 . For purely T_1 -weighted imaging, a short TE and short TR are used to eliminate the effects of T_2 relaxation.

In SE black-blood imaging, blood spins are washed out of the image plane in the time between excitation and refocusing, reducing the signal and increasing the contrast between blood and the surrounding walls. Spin echo is a relatively slow technique, so multiple 180_x° pulses can be applied after the initial excitation to form multiple echoes, as in turbo or fast spin echo (TSE or FSE). Multiple lines of k-space are acquired for a single excitation, increasing the efficiency and speed of the experiment. Prepulses can be used to further suppress blood signal for increased contrast, but at the cost of further acquisition time. With the advent of faster pulse sequences, SE category methods are no longer used for cine imaging, but segmented multiecho SE sequences are clinically used for black-blood morphological imaging [25].

2.2.6.2 Gradient-Recalled Echo

Another way of creating a signal echo is to use gradient pulses instead of RF pulses to reverse the phase of the spins, like in Fast Low Angle Shot or FLASH imaging (Figure 2.16). Instead of an FE preparation gradient, a gradient with the opposite polarity and half the duration of the readout gradient is applied to dephase the spins. This is effectively reversed by the first half of the readout gradient, and the maximum amplitude of the FID signal is again at the centre of the acquisition period, after which the spins will dephase again. The 180_x° pulse is eliminated, and transverse magnetization phase coherences can be destroyed or spoiled after the readout and before the next RF pulse by a gradient or RF spoiling in the slice-encode direction.

Furthermore, the flip angle used for the excitation pulse is less than 90° , in contrast to the spin-echo sequence. As such, the longitudinal magnetization will not be completely depleted and the relaxation time to equilibrium is shorter than if all the magnetization were flipped down. This allows for shorter TR than in the spin-echo sequence, but also results in less available transverse magnetization for FID signal production. Since the dephasing due to field inhomogeneities is not reversed with this method, the signal's maximum amplitude will be less than that of the spin-echo, being dependent on T_2^* rather than T_2 . Field inhomogeneity-dependent relaxation increases with increasing TE, so a relatively short TE is used for GRE pulse sequences. Thus a balance between flip angle and TE must be reached for effective imaging. Multiple echoes can be sampled after each individual excitation for increased speed, as in turboFLASH, but images will have limited signal-to-noise ratio (SNR).

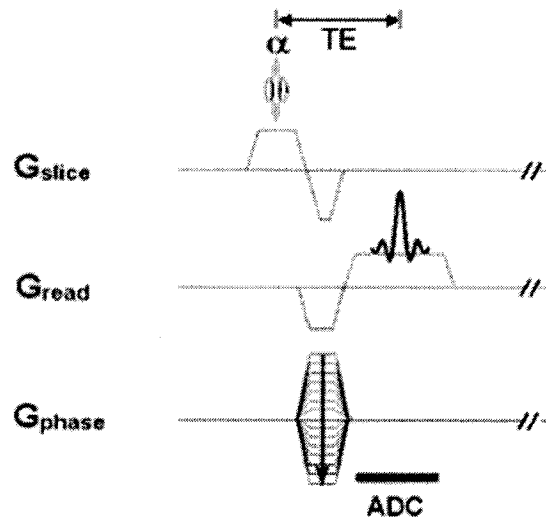


Figure 2.16 Gradient-echo or FLASH pulse sequence. A preparatory dephasing gradient is applied in the readout direction to create a gradient echo at the centre of the acquisition period. The excitation RF pulse flip angle α is less than 90° . Adapted from [15].

T_2^* weighting is implemented by using a small flip angle, such that the longitudinal magnetization has a short relaxation time, and a large TE allows for the evolution of T_2^* -dependent dephasing. Large flip angles and short TR can be used without much loss in signal amplitude in those tissues with sufficient concentrations of contrast agent. GRE sequences are most commonly used for T_1 contrast-enhanced imaging because of the short TE, which results in strong T_1 -weighting with short acquisition times. Rapid flow of blood through orifices enhances the signal, so cine GRE is used for imaging of heart valve flow and stenoses [25].

2.2.6.3 Steady-State Free Precession

The last pulse sequence described in this section is called a variety of names, such as true fast imaging with steady-state precession (TrueFISP), steady-state free precession (SSFP), balanced fast field echo (FFE), and fast imaging employing steady-state acquisition (FIESTA). The principle behind this imaging sequence is that the effects of all the separate components are reversed or rewound in each sequence repetition [38]. Thus the transverse magnetization is not spoiled after the readout acquisition, but rather refocused prior to the next sequence repetition, where it is combined with the next excitation of the remaining longitudinal magnetization (Figure 2.17). Although the technique has been around since the 1980s, implementation was not feasible until the advent of stronger and faster gradient systems.

All the gradients have dephasing and rephasing components, and each excitation RF pulse is opposite in phase from the previous. This results in a steady-state transverse

magnetization and TR is made extremely short to prevent additional dephasing due to field inhomogeneities. A large flip angle is used for high signal amplitude, and is optimized for the T_1/T_2 times of the region of interest as follows:

$$\cos(\theta_{optimal}) = \frac{T_1 - T_2}{T_1 + T_2} \quad (2.56)$$

such that:

$$M_{xy}(\theta_{optimal}) = \left(\frac{T_2}{T_1}\right)^{\frac{1}{2}} \frac{M_0}{2} \quad (2.57)$$

provided that TR is short and TE is zero.

Several T_1 times are required to get the equilibrium transverse magnetization to the steady-state. Preparation pulses can be applied to put the magnetization close to the steady-state, after which acquisition can be started immediately. Contrast can be manipulated with the use of other prepulses for the purposes of fat saturation or $T_{1,2}$ weighting [15].

For short TE and TR, the signal intensity depends on the combined effects of T_1 and T_2 . Substances with a high T_2/T_1 ratio, such as blood, will have the greatest intensity, and the short TE/TR times lead to insensitivity to flow artifacts. Thus the pulse sequence has high SNR and blood-myocardium contrast and is now commonly used for cardiac function and anatomical studies. Dark band artifacts can occur if TR is not short enough, but generally contrast and SNR are higher than that of GRE techniques.

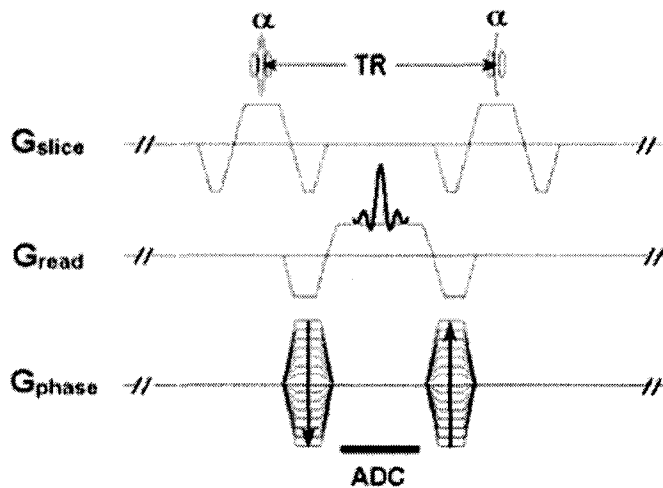


Figure 2.17 Typical SSFP pulse sequence. RF pulses are symmetrical and all gradient effects are rewound. TR, repetition time [15].

2.3 Projection Reconstruction Trajectory

Radial or projection reconstruction (PR) has been around since the development of computed tomography imaging, and improvements in gradient coil hardware and computational power has led to renewed interest in its application. One of the strengths of this trajectory is its insensitivity to motion, which is especially attractive for imaging regions with a large degree of movement, such as the heart. This section will describe the implementation of the sampling trajectory and its associated advantages and disadvantages as compared to Cartesian imaging.

2.3.1 Projection Reconstruction

A line of k-space (projection) consisting of a set number of readout points is acquired at a set angle from the x-axis, and the angle is varied for subsequent projections until k-space is fully covered (Figure 2.18). The trajectory is defined as:

$$k(t) = \gamma \left(\cos(\theta(t)) + i \sin(\theta(t)) \right) \quad (2.58)$$

Where $k(t) = k_x(t) + ik_y(t)$ is the complex location in k-space (radians/length), r is the radius from the origin and $\theta(t)$ is the projection angle. Typically θ is specified such that the projections are spaced at equal intervals around the origin.

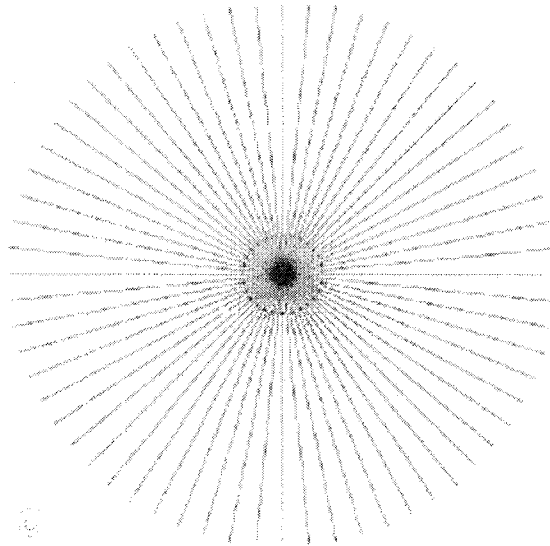


Figure 2.18 Projection reconstruction trajectory with 32 evenly spaced projections. The dotted circle delineates the threshold for full FOV reconstruction [56].

The number of projections is selected such that the maximum spacing between adjacent points should be $1/\text{FOV}$ to reconstruct a fully sampled image, according to the Nyquist

sampling criterion. If there are N_r readout points per projection, the number of required projections N_p is given as:

$$N_p = \frac{\pi}{2} N_r \quad (2.59)$$

Note that this formula applies to an end-to-end 180° acquisition, while a centre-out 360° acquisition would require double the number of projections. There is a factor of $\pi/2$ increase in data acquisition time from Cartesian to PR because of the higher sampling density near the origin. The centre of k-space is updated with each projection, and the averaging of low spatial-frequency components results in decreased motion artifacts, but spatial resolution is decreased due to reduced sampling at the edge of k-space. PR also features shortened minimum TE between excitation and data acquisition, which is useful in imaging short T_2 species and dynamic imaging.

2.3.2 Regridding

A disadvantage inherent in all non-Cartesian trajectories is the complexity of conversion from k-space to image space. The most common approach is to regrid the data points to a Cartesian grid and apply the FFT.

Infinite k-space is sampled with a non-Cartesian trajectory S such that k-space is zero everywhere except at the sampling points (delta functions). These points will be gridded to a Cartesian trajectory by convolution where the data points within a certain range of the nearest Cartesian point contribute varying weights of their magnitude to the Cartesian

point's magnitude. Any arbitrary convolution kernel function can be used that has its maximum value at the centre and drops off towards the edges of the nearest neighbourhood, with the easily computable Kaiser-Bessel function providing the best performance [22]. Specifications for Kaiser-Bessel kernel design include the order of the Besseli function, β which is used to calculate the shape of the kernel, the number of sampling points N in the nearest neighbourhood and the number of inter-sampling points M between them (Figure 2.19).

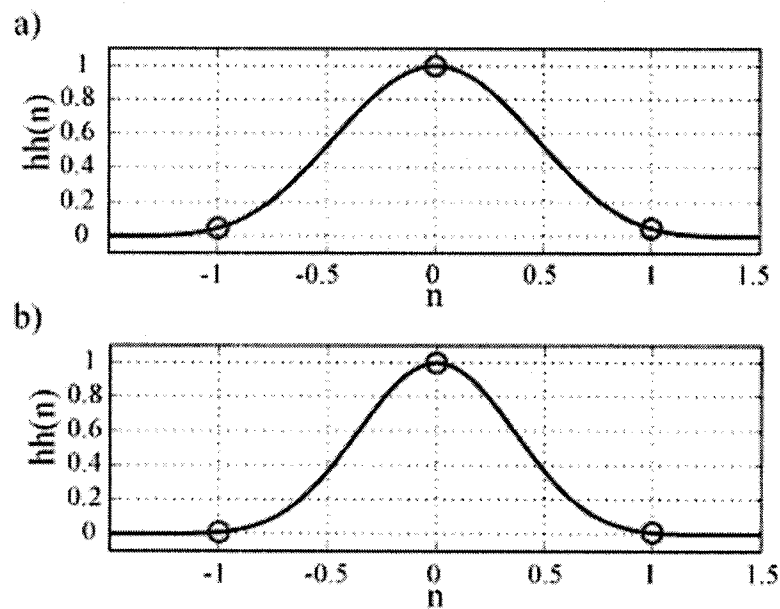


Figure 2.19 Kaiser-Bessel function used as the convolution kernel. $N = 3$, $M = 2048$, order = 8. a) $\beta = 8$. b) $\beta = 16$. Circles indicate the N sampling trajectory points.

The sampling density is non-uniform being weighted more in the centre than at the edges, which will introduce unwanted signal variation. This can be corrected prior to regridding by multiplying the k-space dataset by a density compensation function (DCF) that is the inverse of the current sampling density. After regridding, the image may have signal variations due to the convolution operation, which is correctable by deconvolving k-space

by the convolution kernel, or dividing the image by the Fourier transform of the kernel (termed the apodization function).

In general:

$$M_c(k_x, k_y) = \left\{ \left[\left(M_s(k_x, k_y) \bullet W(k_x, k_y) \right) \otimes C(k_x, k_y) \right] \bullet R(k_x, k_y) \right\} \otimes^{-1} C(k_x, k_y) \quad (2.60)$$

where $M_C(k_x, k_y)$ is the regridded k-space data, $M_S(k_x, k_y)$ is the k-space data sampled with the non-Cartesian trajectory $S(k_x, k_y)$, $W(k_x, k_y)$ is the density compensation function, $C(k_x, k_y)$ is the convolution kernel, and $R(k_x, k_y)$ is the desired output Cartesian trajectory.

The density compensation function W can influence the amount of high-frequency artifacts and ringing present in the image. The simplest is the absolute ramp or Ram-Lak function, which is simply an inverted triangle. Other functions include the Shepp-Logan (Ram-Lak modulated by a sinc function), the cosine, or the Hamming and Hann filters. Pipe et al proposed an iterative density compensation scheme, which uses the k-space trajectory S itself to design the weighting function [41, 43].

The goal of data weighting is to produce an even sampling density across S , such that:

$$S(W \otimes C) = S \quad (2.61)$$

Solving for W , the iterative function is as follows:

$$W_{i+1} = \frac{W_i}{W_i \otimes C} \quad (2.62)$$

where each estimate of the weighting function W_i is updated by dividing it by the convolution of itself with the kernel function C . The initial starting point ($i=1$) uses S as the weighting function W_1 , given that W will be zero everywhere except on the S trajectory, and every point is initially weighted at its full value. An advantage of this technique is that it does not require information about the type of sampling trajectory, and can handle variable sampling density, but requires an excessive amount of processing time.

2.3.3 Undersampling

One approach for improving temporal resolution is to reduce the number of k-space data points through undersampling (Figure 2.20). Most of the energy of an image is contained in the centre of k-space, so trajectories that oversample that region such as PR can reduce the number of projections/interleaves such that the overall image contrast is preserved with minimal artifacts. This strategy is used mainly for ultra-fast applications such as real-time interactive imaging that requires high temporal resolution and can tolerate reduced spatial resolution.

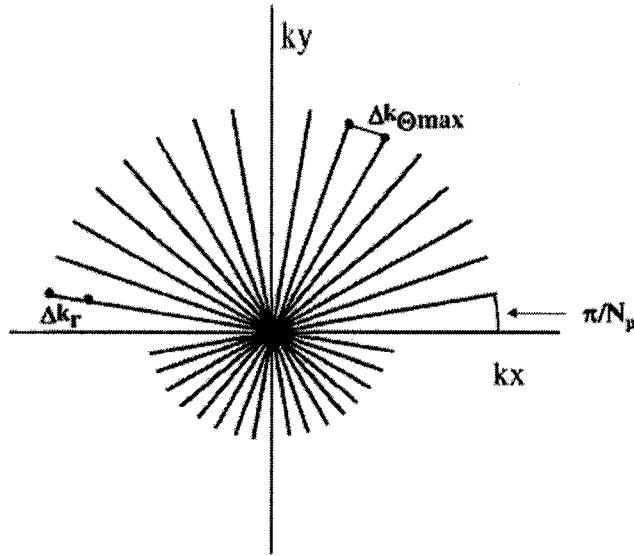


Figure 2.20 Undersampling for projection reconstruction trajectory can be accomplished by reducing the number of projections N_p so the angular spacing $\Delta k_{\Theta \max}$ exceeds the radial spacing Δk_r . The angular step size is given by π/N_p [40].

The main effect of undersampling can be seen in the point spread function (PSF), which is the impulse response of the sampling trajectory, where the diameter of the alias-free region of the PSF decreases as a function of the maximum fully sampled FOV that can be reconstructed. The missing spatial frequencies from unsampled regions will alias into the full reconstructed image FOV, causing ghosting or ringing (Gibbs ringing). Truncating the extent of k-space will widen the main lobe of the PSF, increasing blurring, but reduces the overall level of artifacting so that the SNR improves (Figure 2.21).

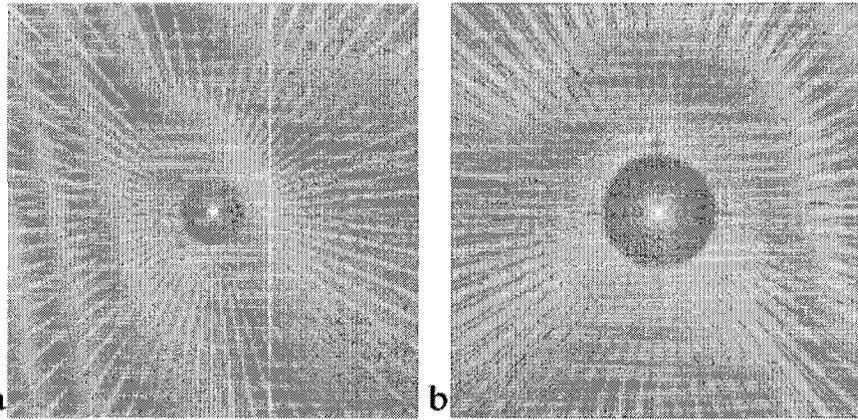


Figure 2.21 Point spread functions of a) undersampled PR and b) truncated undersampled PR. The unaliased or low-aliasing zone and the main lobe is wider for b), leading to increased blurring but decreased overall aliasing [56].

During image reconstruction, if the convolution kernel width is smaller than the maximum inter-point spacing, the iterative weighting function will flatten out at the point the Nyquist sampling criterion is violated because there is no correlation between adjacent points thereafter. This reduces undersampling artifacts and widens the PSF main lobe causing blurring. Increasing the kernel width will eliminate mainlobe spreading but increase the aliasing energy outside of the PSF low-aliasing region, degrading the overall image quality. A balance between image artifact and blurring must be reached to obtain the best quality image.

3 Cardiac Imaging (Literature Review)

This chapter will describe the specifics of how to image the dynamics of the cardiovascular system. Challenges include the separation of motion of the heart and the respiratory system, as well as correction or suppression of respiratory motion artifacts. Various techniques to correct for respiratory motion will be discussed in the following sections while a detailed discussion of the specific approach taken in this project is provided in Chapter 4, Methods.

3.1 Cardiac Gating

When imaging a dynamic process like the cardiac cycle, often there is a trade-off between temporal and spatial resolution, where increasing one will drastically decrease the other beyond any useful capacity. The periodicity of the cardiac cycle allows for gated-segmented acquisition, where a reduced k-space dataset (segment) is acquired for each stage of motion or cardiac phase over several heartbeats with an interleaved sampling trajectory such that the combination of the segments for each phase create a fully sampled dataset that has excellent temporal and spatial resolution [25]. It is assumed that issues regarding flow and gradient induced distortion of the ECG have been sufficiently dealt with and will not be discussed here.

The acquisition can be matched to the ECG signal either prospectively or retrospectively. Prospectively triggered gating starts the segment sequence upon the acquisition of the ECG R-wave, and each segment acquired represents a single cardiac phase (Figure 3.1 a).

The acquisition is often set to a certain number of segments regardless of the actual length of the individual heartbeat, so phases at the end of the cardiac cycle may not be fully sampled and early R-waves may be missed. Retrospectively triggered gating acquires segments over the entire acquisition regardless of where they are in the heartbeat, and reconstruct the images by using recorded ECG signal data to match the segments to corresponding cardiac phases (Figure 3.1b). The segments no longer line up within the cardiac cycle, so there is a chance that two segments with identical sampling trajectories and cardiac phases could be acquired, and full sampling would not be attained; however, the entire cardiac cycle is covered for full temporal sampling [8, 16].

Drawbacks to this method are that the images are not real-time, so cannot be used for processes that require constant updating such as contrast-enhanced angiography. Also, any extraneous motion between heartbeats will introduce motion artifacts into the final reconstructed images. If the ECG signal is erratic, as with arrhythmia, some k-space regions may get less coverage for certain cardiac phases, and the final images may contain undersampling artifacts. Retrospective cine imaging can be performed with rejection of data acquired during arrhythmic cardiac cycles to produce good quality images [25]. An advantage of segmented acquisition is that each segment can be used to measure real-time motion, either by reconstructing low-resolution images for use in image registration or by measuring errors in k-space characteristics such as first moments [55, 57].

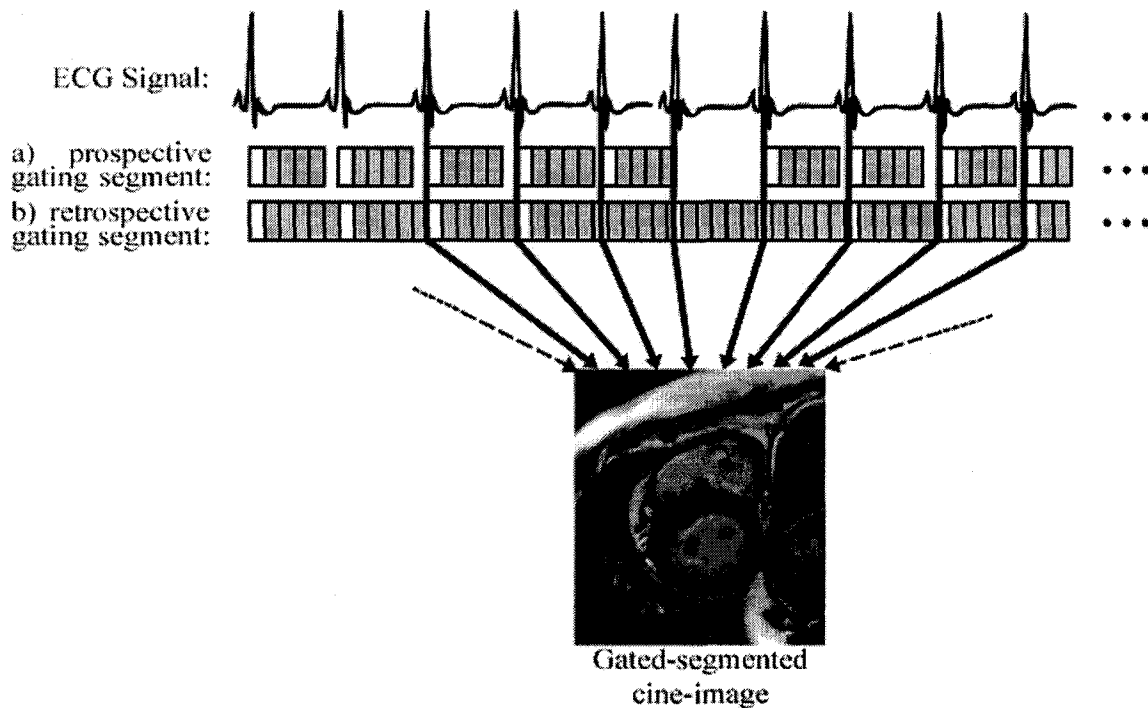


Figure 3.1 Cardiac gated-segmented acquisition. K-space data acquired at each cardiac phase can be combined into a fully sampled dataset that gives a high spatial and temporal resolution image. a) Prospective triggering acquires a certain number of segments for each cardiac cycle starting at a particular point in the cardiac cycle, regardless of the length of each individual heartbeat. b) Retrospective triggering acquires segments over the entire acquisition, relying on recorded ECG signal data to match up the data for the appropriate phases post-acquisition.

A variant on gated-segmented imaging is data sharing or sliding window reconstruction, where images are constructed closer together in time by overlapping the data acquired in adjacent segments. This does not alter temporal resolution in that it still takes the same amount of time to acquire a single image, but the time interval between two images is decreased, leading to smoother cines.

3.2 Respiratory Motion

Motion contamination has been a major issue since the 1980s, when a number of scientists noted the detrimental effects of respiration on abdominal imaging [1, 3, 17, 49,

59, 60]. The effect of respiration on the position of the heart is complex, including 3D translation, rotation, and local deformation [33]. There is also great variability between patients and positional differences that are dependent on the respiratory waveform [10, 23, 36]. The following section describes image artifacts due to motion, and ways that it can be corrected during acquisition or post-acquisition.

3.2.1 Artifacts

Diffusion and perfusion can dephase the magnetic moments within the tissue reducing signal amplitude, while physiological motion can introduce discrepancies between the excitation pulse and the actual acquisition of the signal (intra-view), or between two consecutive acquisitions (inter-view), causing signal intensity and phase modulation. Pulsatile blood flow will move the excited nuclei out of the imaging FOV during the scan and introduce fresh blood signal flowing in.

The signal $s(t')$ acquired in a particular direction will be modulated by a signal intensity variation function $m(t')$ caused by motion (where t' is the index along the phase-encode direction), which in image space translates into the convolution of the corresponding component of the object $S(f)$ by the Fourier transform of the modulation function $M(f)$ (Figure 3.2) [3]. For periodic motion, $M(f)$ will consist of spikes separated by the frequency of motion f_{mot} , resulting in repetitions of the object component across the image, or ghosts. The distance between the ghosts can be calculated as follows:

$$d = f_{mot} \Delta t N \quad (2.63)$$

where d is the separation distance, f_{mot} is the frequency of motion, Δt is the time before k -space is incremented in a particular direction, and N is the number of points in that direction [54]. Basically the formula says that ghost separation is dependent on the time used to acquire the dataset in one direction ($\Delta t N$) and the rate of movement f_{mot} . Thus for Cartesian acquisition, ghosts in the phase-encoding direction are more noticeable than in the frequency-encoding direction (which suffers more from blurring) because acquisition time is longer (repetition time TR between excitation pulses as opposed to sampling time Δt between readout points) allowing for greater signal modulation [3, 17, 49, 59]. Ghosts that would appear beyond the image FOV are wrapped back around to the other side and aliased back into the image. Ghost artifact appearance can vary from complete copies of the static image to less defined curvilinear artifacts due to self-interference which reinforces the artifacts at some points and cancels them out at others. Motion that is not periodic results in smearing rather than ghosting in the phase-encode direction.

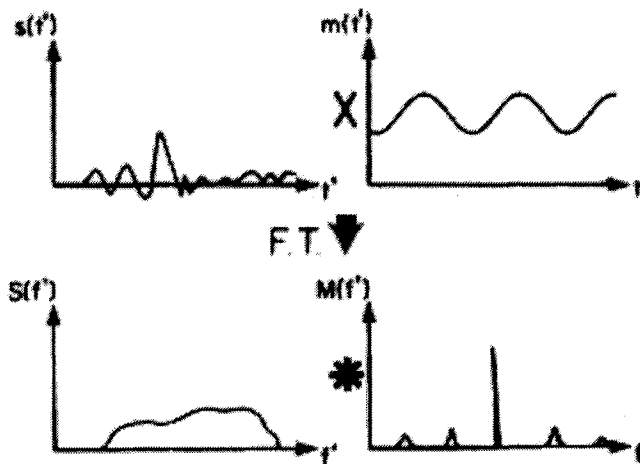


Figure 3.2 A 1D signal $s(t')$ obtained by applying different phase-encode gradient pulses is modulated by a periodic motion-induced variation in signal $m(t')$. In image space, this

translates into the convolution of the corresponding component of the stationary object $S(f')$ by the Fourier transform of the modulation function $M(f')$ [3].

Trajectories that re-acquire the centre of k-space for every projection benefit from signal-averaging of low-frequency components that minimizes ghosting by increasing the signal-to-noise ratio, but increases acquisition time and does not eliminate blurring [60]. PR also suffers from additional radial streaking perpendicular to the endocardial border. Three artifact suppression approaches are typical in imaging: limiting or reducing the motion during acquisition such as with breath-holds or gating; acquiring the information in a time that is relatively short compared to the motion; or using post-acquisition techniques to correct the motion-distorted dataset.

3.2.2 Motion Artifact Suppression

The major techniques for suppression of motion artifacts during data acquisition will be explained and discussed in terms of overall success and effect on image acquisition.

3.2.2.1 Breath-hold

Usually the patient is asked to hold their breath during acquisition, ranging from 5 to 20 seconds. Consistency is important for selecting subsequent image orientations based on previous scans, and is generally better for end-expiration breath-holds [8]. It requires no equipment or extra MR pulses, and a complete cine-image series for a single slice can be acquired within a breath-hold with fast pulse sequences such as turboFLASH or SSFP.

The breath-hold is currently the gold standard for motion-free cardiac imaging, easily eliminating much of the blurring due to respiration as in Figure 3.3.

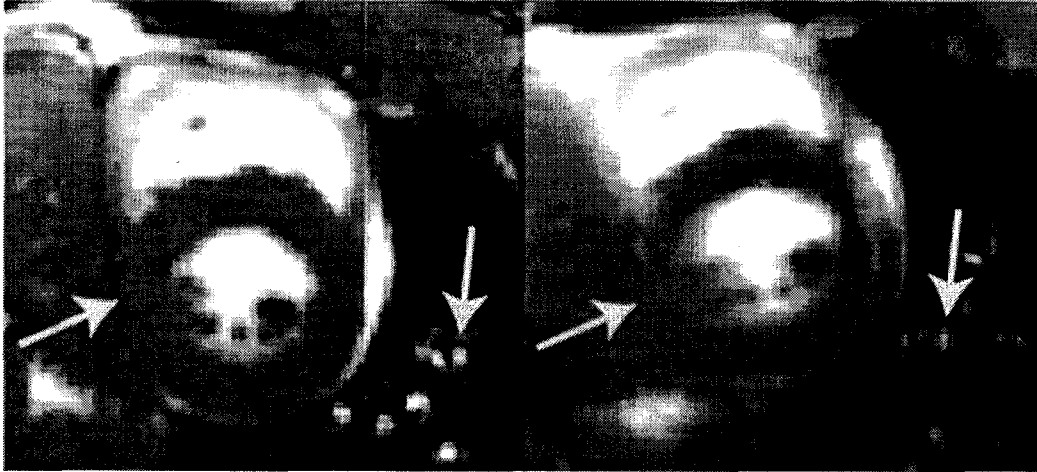


Figure 3.3 a) Breath-hold gold standard and b) free-breathing short-axis cardiac images. In b), the edge of the myocardium is blurred, and fine features such as pulmonary vessels in the lungs are obscured (arrows). Adapted from [52].

One drawback is the increased patient discomfort during the procedure. Furthermore, children or the very ill who are unable to voluntarily hold their breath are excluded from this technique. Spatial and temporal resolution are decreased by limitations on scan duration, and the technique is not perfect in that there can still be motion between breath-holds, which can cause misregistration of consecutively acquired images, or during the breath-hold itself, resulting in motion artifacts. Holland et al found that the mean diaphragm displacement during a breath-hold was a quarter of the displacement during normal breathing, and the heart did not maintain a consistent position during consecutive heartbeats [21]. Small objects such as the coronary arteries cannot be distinguished due to this inconsistency. The overall scan time is prolonged by recovery periods between breath-holds, during which no data can be acquired. Thus developing techniques to

maintain free-breathing during data acquisition is an important goal for clinical cardiac imaging.

3.2.2.2 Gating

One method of motion suppression during free-breathing is gating or windowing, where the data acquisition only occurs when the region of interest is within a certain spatial window. This involves measuring a signal that represents thoracic expansion or relaxation, which usually comes from a pneumatic pressure belt strapped across the abdomen, and triggering the acquisition around end-expiration [47].

The duty cycle must be kept low to minimize motion during acquisition, prolonging the scan time. Also, the respiratory waveform can be inconsistent, so data acquisition may not be triggered regularly. Respiratory motion is an indirect measure of cardiac position, so there may be positional inconsistencies across respiratory cycles that are not adequately characterized, resulting in motion artifacts. Gating is not a widely used technique for these reasons.

A related method is the diminishing variance algorithm (DVA), where initially a complete scan is done simultaneously with position measurement, creating a histogram of positions. The data is then analysed for deviation from a reference position, and the portions that were recorded far from the reference are rescanned [48]. Again, the scan time is prolonged and several passes may be needed to produce a complete dataset.

3.2.2.3 Navigators

More accurate determination of the heart's position allows for a longer gating acquisition window, so Ehman and Felmlee came up with the navigator echo [13]. This involves excitation of spins within a column of tissue parallel to the direction of motion and a spin or gradient echo is recorded while a frequency-encode gradient is applied along the column. The column is typically placed across the boundary between the diaphragm and lung and the signal is measured prior to each phase-encode line, taking less than 50 ms. This gives a 1D edge signal that can be used to determine respiratory motion, as in Figure 3.4. Because the navigator echo is an additional excitation extraneous to the main experiment, care must be taken not to interfere with the region of interest and introduce saturation artifacts. The relative displacement or correction factor is used to either correct the image slice location during acquisition, as in real-time prospective slice –following for coronary angiography [9, 31], or post-acquisition, to allow for patient-specific correction factor optimization.

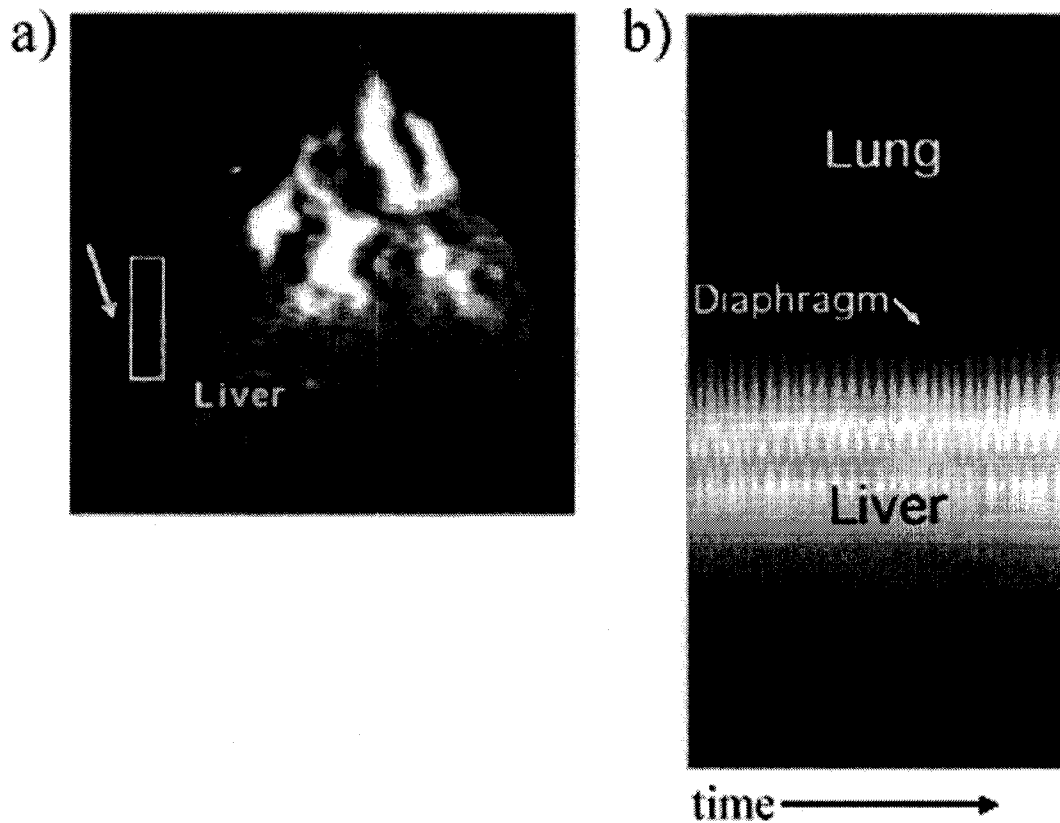


Figure 3.4 Typical vertical navigator echo used in cardiac imaging. a) Coronal scout MR image showing column of excited spins across liver-diaphragm-lung boundary marked by white rectangle, with right hemidiaphragm marked by white arrow. b) 1D edge signal representing respiratory motion over time [30].

The additional acquisition of the navigator information prolongs the acquisition and reduces scan efficiency. Despite the additional accuracy, the respiratory waveform is still an indirect method of assessing heart position, and the drawbacks of section 3.2.2.2 still apply. The heart undergoes 3-D translation that is not represented by the superior-inferior translation of the diaphragm, and Nerhke et al found that certain patients exhibited hysteresis, where the position of the heart differed at expiration and inspiration for the same diaphragmatic position [36]. Applying a navigator directly to the heart would resolve this issue, but placement is difficult due to its complex geometry and 3D motion [23, 30]. If positioned incorrectly, the navigator will not pass through the same region of

the heart at all points of the respiratory cycle. Wang et al used a navigator on the epicardial fat surrounding the coronary arteries that measured global heart motion as accurately as or better than a diaphragmatic navigator, and provided slightly shorter scan times [37].

The accuracy of the navigator technique depends on the navigator signal-to-noise ratio and spatial resolution. The more navigators that are repeated in a single cardiac cycle, the lower the signal-to-noise ratio. Thus for cine-imaging, navigators interleaved with the image acquisition reduce the time in which actual data can be acquired, and will be reduced in quality themselves [14].

3.2.2.4 Phase-encode Reordering

To eliminate periodicity of the motion, and resultant ghosting artifacts, the phase-encode lines or views are ordered to match respiratory motion amplitude. In respiratory ordered phase encoding (ROPE), the smallest amplitude is matched to the most negative phase encoding value and the largest amplitude is matched to the most positive phase encoding value. As a result, the motion function increases monotonically with time during inspiration [4]. The decreased period of motion decreases the separation of the ghosting artifacts to a pixel and essentially eliminates them. ROPE has an asymmetric effect on k-space, causing phase shifts in image space. Another technique, centrally ordered phase encoding (COPE), orders the data from the central region outwards [17]. This creates symmetrically equivalent spatial frequency components, which can be symmetrically filtered while preserving all the best data.

Phase-encode reordering in itself does not prolong imaging time with extra acquisitions or gating, but requires the measurement of the amplitude of motion through navigators or other methods. The artifact energy is conserved and spread over the image as additional blur and distortion, which may be unacceptable for applications with inherently low SNR.

3.2.2.5 Gradient Moment Nulling

Intra-view motion artifacts are caused by motion along the gradients, which leads to dephasing of magnetization and consequent blurring in the image. The motion is modeled as a Taylor series, of which the first three terms correspond to position, velocity and acceleration. A series of gradients are tailored to null the corresponding moments. This procedure is generally called gradient moment nulling, but is also known by other names such as motion artifact suppression technique (MAST) [39], rephasing gradients technique [18], and compensating gradients technique [45]. This does not increase imaging time, but any additional gradients increases the minimum achievable TE. The complicated respiratory motion introduces complexity into sequence design, especially for nonconstant velocities [46]. Other factors such as original gradient functions for slice selection and readout, avoidance of unwanted gradient echoes, and system limitations need to be considered [42].

3.2.3 Real-time Ultrafast Imaging

Another approach is to use ultrafast imaging sequences that are relatively insensitive to motion. The data for an entire image slice is acquired in one distinct temporal window, as opposed to segmented acquisition. There is no need for cardiac or respiratory gating but the reduction in data acquisition time will reduce the spatial resolution and SNR of the image. The combination of parallel imaging with fast pulse sequences such as SSFP can increase the temporal resolution four-fold and alternative trajectories like spiral imaging can sample k-space efficiently with reduced flow and motion artifacts [25, 35]. Echo-planar imaging is very fast, acquiring data in under 100 ms, but issues with spatial resolution and magnetic susceptibility disqualify it from clinical use at present [54]. SNR can be improved by imaging at higher fields, but that comes with its own inherent artifacts arising from susceptibility, off-resonance, RF inhomogeneity and tissue relaxation differences [35].

3.2.4 Motion Artifact Correction

The third approach is the correction of motion artifacts post-acquisition, which requires knowledge of the nature of the motion. Characterization of cardiac motion due to respiration is difficult because of its complex and inconsistent nature. The simplest motion model would be based purely on in-plane translation and rotation. From the Fourier theorem, translation and rotation result in phase modulation and rotation in k-space respectively [24, 60]. Translation motion perpendicular to the imaging plane was found to cause signal amplitude modulation [34]. Chest expansion or dilation was found to cause distortion of both signal phase and amplitude [2]. The heart undergoes twisting

and elastic deformation as well, so more complex modeling is needed for complete characterization.

Manke et al proposed a 3D affine motion model that included scaling (dilation or compression) and shear [28]. Mathematically, the transformation can be written in matrix form as follows:

$$\mathbf{A}(\mathbf{r}) = \mathbf{A} \bullet \mathbf{r} + \mathbf{t} = \begin{bmatrix} \mathbf{a}_{11} & \mathbf{a}_{12} & \mathbf{a}_{13} \\ \mathbf{a}_{21} & \mathbf{a}_{22} & \mathbf{a}_{23} \\ \mathbf{a}_{31} & \mathbf{a}_{32} & \mathbf{a}_{33} \end{bmatrix} \begin{bmatrix} x \\ y \\ z \end{bmatrix} + \begin{bmatrix} t_x \\ t_y \\ t_z \end{bmatrix} \quad (3.1)$$

where $\mathbf{A}(\mathbf{r})$ is the complete transformation of spatial point $\mathbf{r} = (x,y,z)$, \mathbf{A} is the affine transformation matrix, and \mathbf{t} is the 3D translation matrix. There are 12 degrees of freedom in total, with the 9 in \mathbf{A} representing a 3D linear transformation. \mathbf{A} can be decomposed into rotation, scaling and shear matrices as follows:

$$\mathbf{A} = \mathbf{R}(\phi, \theta, \psi) \begin{bmatrix} 1 & S_{xy} & S_{xz} \\ 0 & 1 & S_{yz} \\ 0 & 0 & 1 \end{bmatrix} \begin{bmatrix} S_x & 0 & 0 \\ 0 & S_y & 0 \\ 0 & 0 & S_z \end{bmatrix} \quad (3.2)$$

where $\mathbf{R}(\phi, \theta, \psi)$ is the 3D rotation matrix, $\{S_{xy}, S_{xz}, S_{yz}\}$ is the 3D shear matrix, and $\{S_x, S_y, S_z\}$ is the 3D scaling (dilation or compression) matrix. The lower triangle of the shear matrix represents the perpendicular shearing components of the upper triangle elements

$\{S_{yx}, S_{zx}, S_{zy}\}$. Taking advantage of Fourier transform properties, the spatial affine transformation can be applied to k-space with

$$\mathbf{k}' = \mathbf{A}^{-T} \mathbf{k} \quad (3.3)$$

where \mathbf{k}' is the transformation of the spatial frequency \mathbf{k} . It then follows that the k-space dataset \mathbf{F} is related to the transformed dataset \mathbf{F}' as follows:

$$\mathbf{F}(\mathbf{k}) = \frac{e^{i2\pi(\mathbf{k}' \cdot \mathbf{t})}}{|\det(\mathbf{A})|} \mathbf{F}'(\mathbf{k}') \quad (3.4)$$

This motion model describes complex motion and yet is easily applicable to k-space. Local elastic deformation is present but there is no way to tell the individual effects on k-space, so residual blurring may be present after affine motion correction [33].

3.2.5 Dual-Purpose Acquisition

In gated-segmented imaging, it is possible to use the reduced k-space segments to reconstruct real-time images that are diagnostically useless, but still good enough to measure the motion of the heart. Each segment acquires data evenly over the whole of k-space, but is severely undersampled. The same data is also used to reconstruct high temporal and spatial resolution cine-images, where the segments that make up one cardiac phase's cine-image are interleaved such that there is full sampling of k-space.

Larson et al used a cine radial experiment to monitor the cardiac cycle of the heart in real-time, in order to collect an MRI-gating signal, which was subsequently used to reconstruct the same data via a conventional gated-segmented approach [7, 26]. A similar method was reported for phase-contrast blood velocity experiments [53]. Several coronary angiography groups have compared real-time sub-images to a pre-defined template to detect data acquired without excessive distortion or through-plane motion [20, 50]. McLeish et al reported the use of under-sampled radial images to monitor respiratory motion over many cardiac cycles in order to correct the motion prior to combining the image data into a fully sampled image [32]. However, this study relied on a separate navigator acquisition to monitor through-plane motion and thus was limited to only a single cardiac phase.

The advantage to this technique is the possibility of 100% duty cycle and accurate direct measurement of in-plane or 3D motion of the heart. Using an appropriate motion model such as in section 3.2.4, post-acquisition motion correction can be used to eliminate ghosting and blurring artifacts.

4 Methods

Cardiac cine-imaging is a difficult process due to the need for simultaneously high temporal and spatial resolution. External methods of respiratory motion measurement are not accurate, and internal methods such as navigators require extra acquisition time that will lower the duty cycle and thus the temporal resolution. Real-time imaging has low spatial resolution due to the reduced data acquisition window available for each cardiac phase, and as such, cannot be used diagnostically.

The cine-navigator method advanced in this section proposes to use the k-space data itself to measure cardiac motion, without any extraneous data acquisition or external transducers. It will expand on previous studies by adapting the dual-purpose acquisition for continuous cine-imaging, as opposed to a single cardiac phase, and correcting the motion effects in k-space so as to use a greater percentage of the data.

4.1 K-space Acquisition Scheme

Normally a Cartesian gated-segmented cine experiment would acquire multiple segments of k-space lines over many heartbeats and combine the lines at the same cardiac phase to create a more densely sampled k-space dataset, resulting in higher spatial resolution. This allows for higher temporal resolution since fewer lines can be acquired per segment than would be needed for adequate image quality. The cine-navigator technique incorporated k-space ordering which allowed real-time images to be acquired throughout a conventional gated-segmented cine-experiment, using the same k-space for both purposes. A conventional trueFISP or SSFP pulse sequence was chosen for its high

myocardium-blood contrast and fast imaging speed. Shimming was required to eliminate off-resonance artifacts caused by field inhomogeneity, and the shim box was reduced to cover only the region of the heart for maximum uniformity in that area.

The entire acquisition was broken up into segments of time within which undersampled k-space datasets are acquired. In this study, interleaved radial k-space trajectories were used to allow full field of view, full spatial resolution real-time (RT) images to be directly reconstructed from reduced k-space datasets. Theoretically this could be done with Cartesian trajectories and parallel imaging techniques, but the radial trajectory also allows for easier application of affine motion correction parameters to k-space.

For the gated-segmented (GS) images, the k-space lines at the same true cardiac phase in all the heartbeats were used to reconstruct a fully sampled high-resolution image of that cardiac phase (Figure 4.1), and each unique segment configuration was angularly offset from the previous one to maintain even k-space coverage in the GS dataset (Figure 4.2).

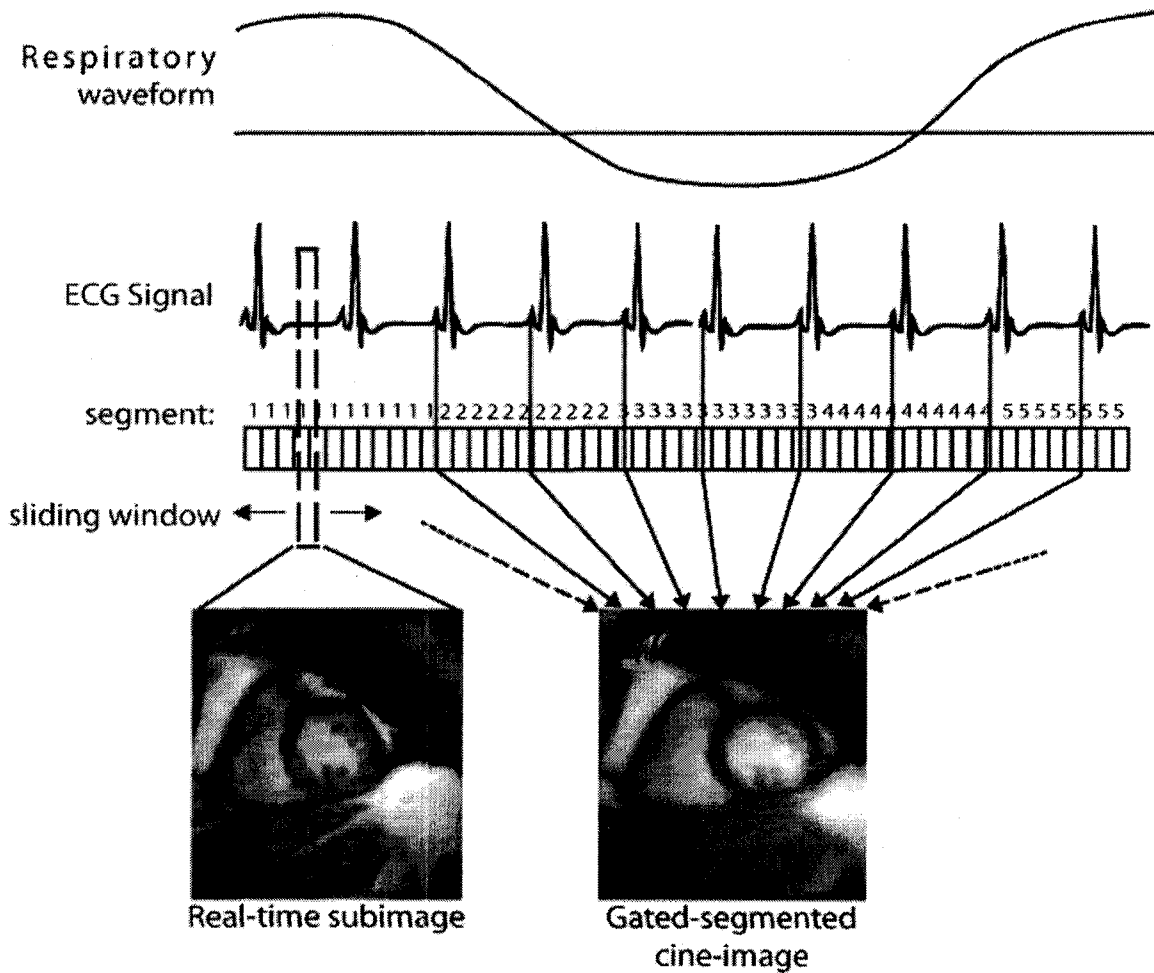


Figure 4.1 K-space dual-purpose acquisition scheme. Sliding window reconstruction is used to create a series of real-time subimages (left) for respiratory motion navigation purposes. The corrected k-space lines are then used in conventional gated-segmented reconstruction to create high temporal and spatial resolution cine-images, which contain blurring and ghosting due to motion (right). For greater temporal resolution of each line, each unique segment configuration (i.e. segment 1, 2, 3, 4, 5, etc) is acquired over several heartbeats.

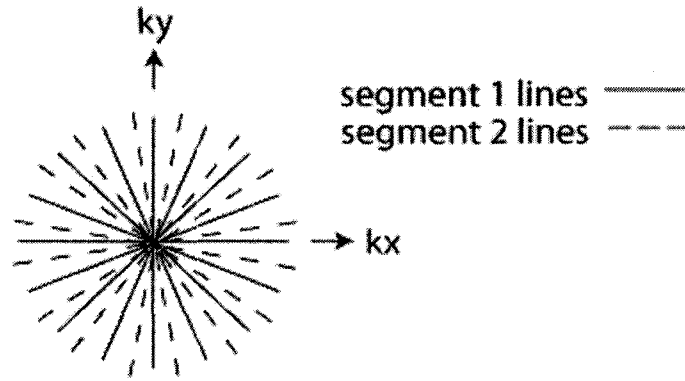


Figure 4.2 K-space radial trajectory interleaving. Each consecutive radial segment configuration is angularly offset from the previous. This gives even coverage of k-space for both the undersampled real-time and the combined gated-segmented dataset.

In conventional interleaving, each segment's lines are acquired at equispaced intervals to evenly cover k-space. With cine-navigator interleaving, every segment's lines cover half of k-space, such that every two segments' worth of lines is used to create one real-time image, as in Figure 4.3. The minimization of large jumps in k-space reduces artifacts due to eddy currents. The segments are acquired over a fixed period of time, regardless of the length of the cardiac cycle, so each line will not be acquired at the exact same time within each cardiac phase of each heartbeat. In order to maintain the temporal resolution of the GS cine-image series, each unique segment configuration is acquired over several heartbeats to increase the temporal sampling frequency of each line (Figure 4.1). Sliding window reconstruction is used to reconstruct RT images for user-defined real-time cardiac phases, with a temporal resolution of less than 100 ms.

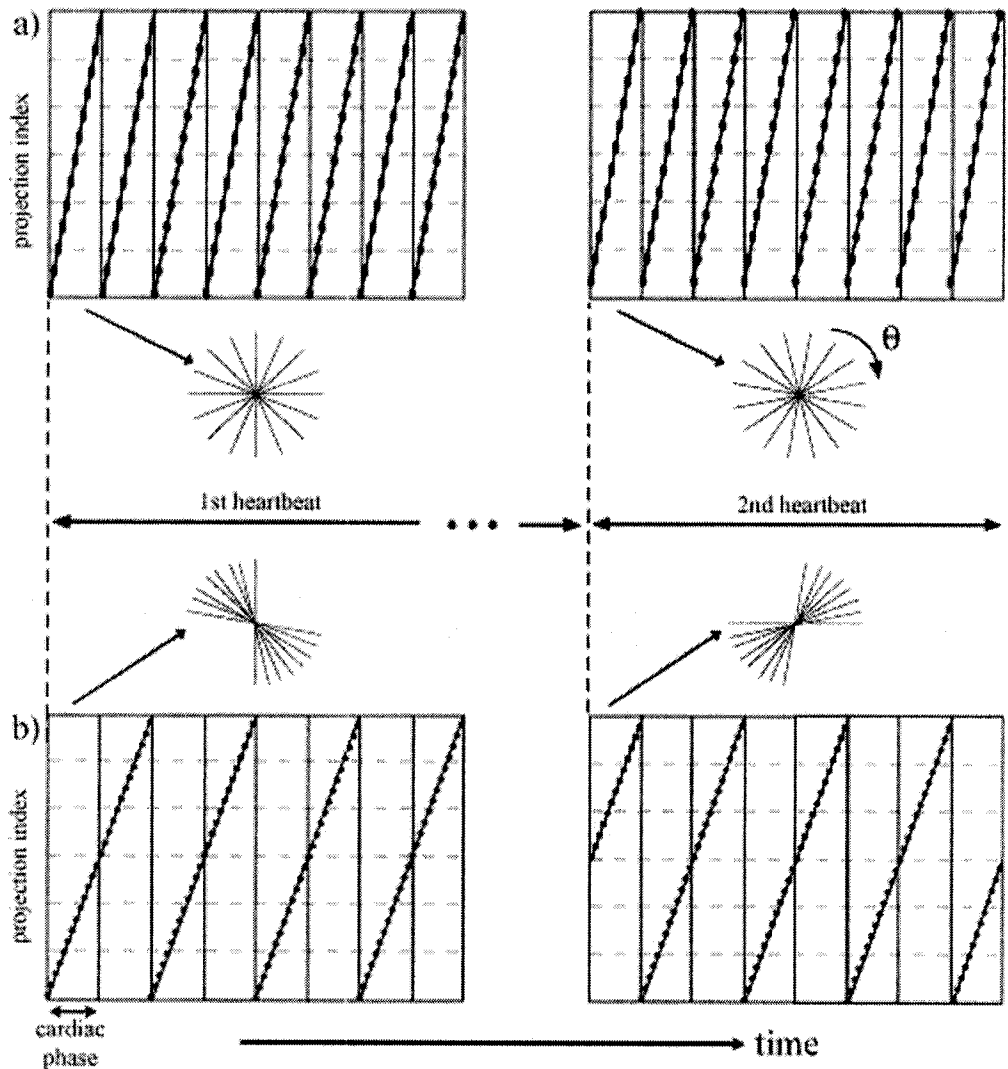


Figure 4.3 K-space segment line ordering. a) Conventional cine-imaging line interleaving with each segment's lines or projections evenly covering k-space, and b) cine-navigator line interleaving, where every two consecutive segments' projections combine for a more densely sampled dataset. Each line is acquired at different times for each heartbeat due to retrospective triggering, so each unique segment configuration is acquired over several heartbeats to maintain the temporal resolution of the k-space lines (in this example, lines have been shifted by a whole cardiac phase from one heartbeat to the next).

The radial dataset was regridded to a Cartesian trajectory for use with the fast Fourier transform, using a Kaiser-Bessel convolution kernel ($\beta = 8$, order = 8, $M = 2048$) of width $N = 9$ for the RT reconstruction and $N = 3$ for the GS reconstruction [22, 43]. The undersampling ratio, or the ratio between the maximum inter-projection spacing and the readout point spacing, for the RT reconstruction was 14.5, but a nearest neighbourhood of

$N = 29$ produced excessive blurring, so a smaller value was chosen to minimize blurring yet suppress overall image artifacting. For the gated-segmented image reconstruction, temporal as well as spatial regridding was performed, with each image's reconstruction including data from neighbouring cardiac phases weighted by the temporal convolution kernel ($\beta = (0.25\pi)20N/n_{\text{cardphases}}$, $N = 3$). Since cardiac motion is cyclic, the data from phases at the beginning and end of the cardiac cycle were wrapped around to the other side for use in regridding. Iterative density compensation was applied to even out the RT sampling density and the GS DCF was calculated as the multiplication of the entire dataset's spatial DCF by its temporal weighting (Figure 4.4). Due to reconstruction time constraints, a Shepp-Logan filter was used as the GS DCF, as the iterative density compensation function calculation time exceeded 35 hours.

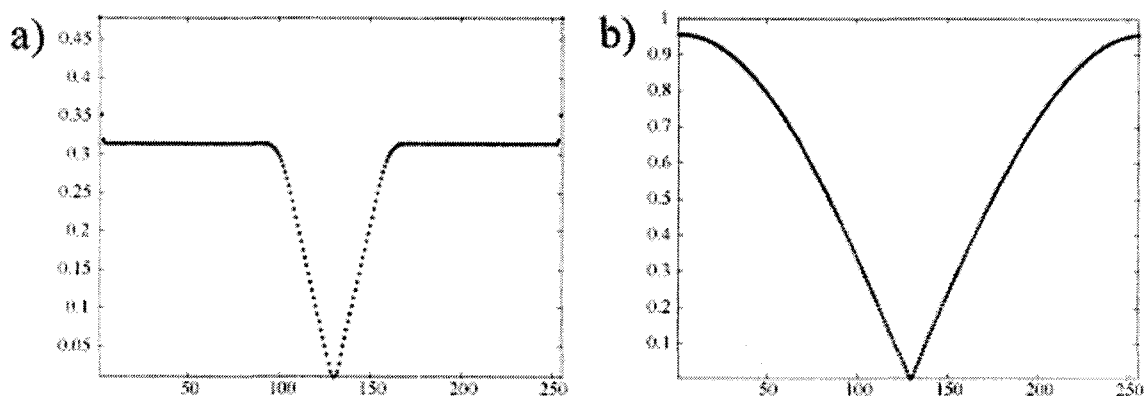


Figure 4.4 a) Undersampled RT DCF (calculated with $N = 9$, $\beta = 8$ Kaiser-Bessel kernel). b) Fully sampled GS DCF (Shepp-Logan filter). The vertical axis gives the weighting value while the horizontal axis gives the index of the readout points in each projection. The DCF would be applied to each individual projection in the RT or GS k-space dataset.

The cine-navigator technique utilized the real-time images to measure and correct for unwanted respiratory motion through image matching or registration, as described in the next section. The acquisition was retrospectively triggered, allowing for more complete

coverage of the cardiac cycle and thus a more accurate measure of the respiratory waveform.

4.2 *Real-time Motion Measurement*

In order to distinguish between respiratory and cardiac motion, the real-time images acquired throughout free-breathing were registered separately for each real-time cardiac phase (Figure 4.5). Respiratory motion was measured in terms of the difference between the orientation of the heart in the free-breathing image series and a reference image. Reference images for each cardiac phase were chosen from the free-breathing images themselves, and do not require additional navigator or training data acquisitions, or an interruption of the steady-state magnetization.

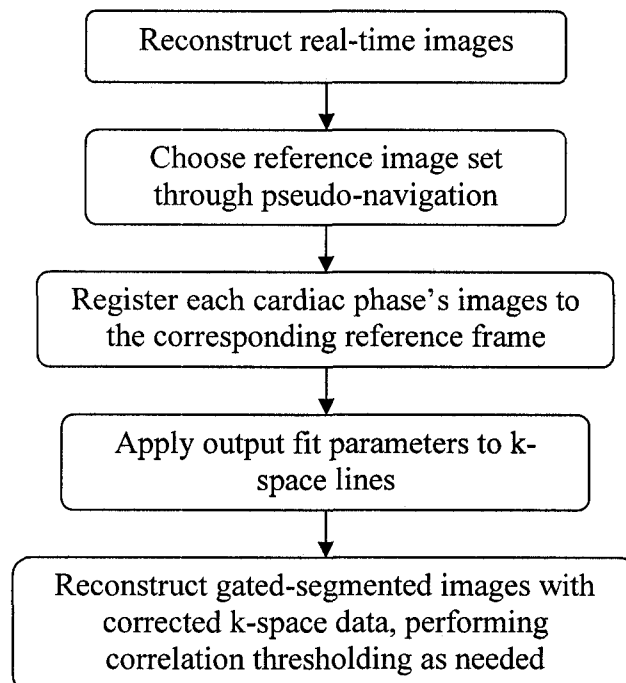


Figure 4.5 Flowchart of real-time respiratory motion measurement and correction procedure.

An intensity-based registration algorithm was used to perform image comparison and registration [51]. Landmark-based registration was not advisable for this method since cardiac physiology will vary from subject to subject and may be obscured by noise or motion artifacts. A sample image or series of sample images was compared to a reference image and a set of output fit parameters was returned, including affine and translation matrices that can be applied to the sample image to match it to the reference image, as in equation 3.1.

To select the reference image set, a pseudo-navigator profile method was devised, where a 1-D profile was measured across the heart parallel to the intraventricular septum (IVS) for all images, creating a rough time series of translational movement in that direction (Figure 4.6). The time intervals that show the least translational movement were assumed to be end-expiration, and the reference image set was chosen as the cardiac cycle with the least change in position over the individual frames. The normal respiratory period lasts over several heartbeats so this reference image series can be taken as relatively static. For other orientations, the profile was drawn perpendicular to the IVS in the 4-chamber view.

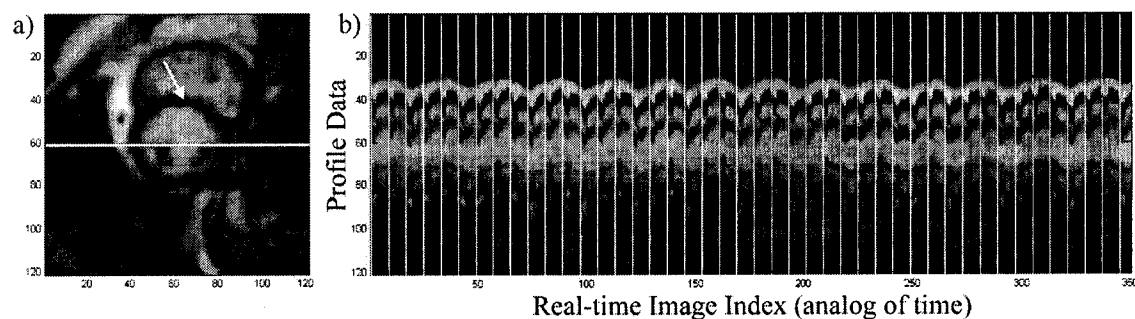


Figure 4.6 Reference profile-time series. a) A 1-D profile (white line) is chosen parallel to the intraventricular septum (white arrow) across the left ventricle for all the real-time images, going

from left to right. b) When ordered sequentially, the profile series gives the translational motion with respect to time in that direction. Both the respiratory and cardiac motion characteristics are easily visible. The white lines delineate the individual cardiac cycles.

For rotation, a positive rotation angle θ resulted in clockwise rotation around the center of the image, and the opposite occurred for a negative rotation angle θ . Scaling in the horizontal or vertical dimensions was indicated by the elements S_x and S_y respectively, while shear could be in the horizontal or vertical direction, as indicated by the S_{xy} and S_{yx} elements. Plotting the affine parameters for the complete acquisition serially in time gives a rough respiratory waveform, as in Figure 4.7.

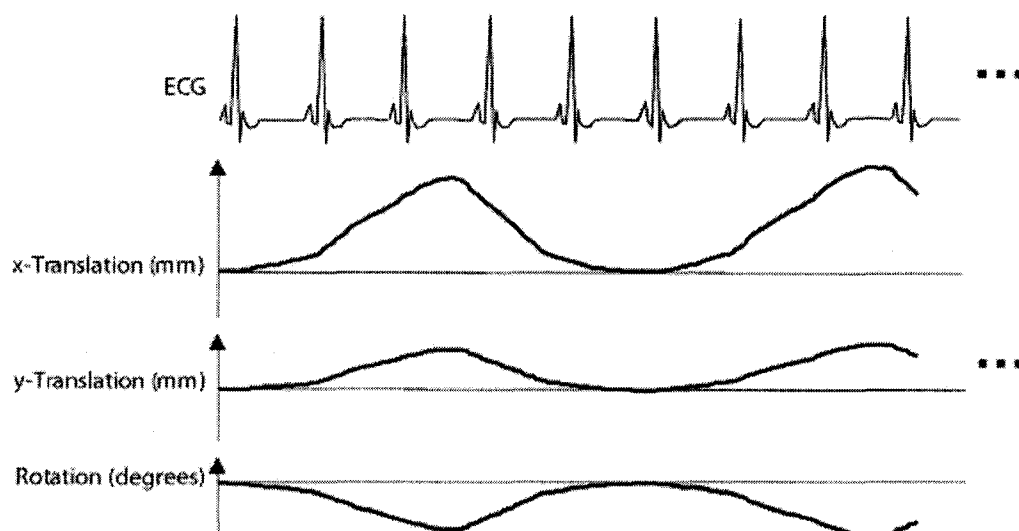


Figure 4.7 In-plane translation (x and y directions) as well as rotation parameters returned by the registration algorithm, mapped out serially in time.

The image registration algorithm worked best for high-intensity features, but the brightest intensity came from unwanted fat outside the heart, causing misregistration of the heart. Masking of the region of interest limited the calculation to the region of interest, increasing the accuracy of the fit. To mask out the extraneous regions but still encompass the entire range of cardiac and respiratory motion, the user was asked to define the region

of interest on an image constructed by adding all the images in the study together. The mask was then applied to both the input and reference images. The mask was defined around the entire heart and the separate ventricles to determine its effect on the accuracy of registration for each ventricle.

The efficiency and accuracy of the registration could be adjusted through various user-inputted settings in the program. The registration algorithm could be set to use translation only, rotation and translation only, or shear and translation only (affine) registration criterion to match the images. Affine registration was chosen to achieve the most accurate fit for the cardiac situation, as negative pressure in the chest cavity during inspiration imposes more than just translation on the heart. Local deformations cannot be easily translated to k-space, so were not measured in this study.

There was no isometric scaling calculated with the rotation or affine options, as it indicates excessive through-plane motion. It was thus assumed that the affine matrix was made up of only the rotation and/or shear matrices. A motion phantom consisting of a cylindrical body with several cylindrical rods was used to validate the image registration for rotation and translation. The phantom underwent 2D and 3D motion to simulate in-plane and through-plane motion. A digitally sheared image of the phantom was used to test the registration algorithm output for linear shear. It was discovered that the affine matrix returned is the inverse transpose of that which would transform the input images to match the reference image (Figure 4.8). For rotation, this is irrelevant since the matrix is unaffected, but for shear this results in a shear transformation in the orthogonal

direction. To compensate, the fit was read in as $[A(1,1) \ -A(2,1); \ -A(1,2) \ A(2,2)]$, which gives the correct transformation.

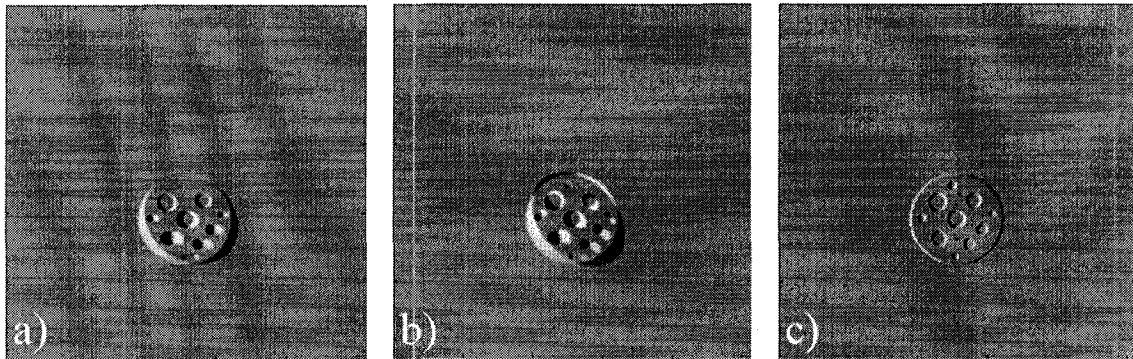


Figure 4.8 Affine registration algorithm phantom test. a) Difference image of phantom and artificially sheared phantom. b) Difference image of phantom and artificially sheared phantom corrected with output parameters of registration algorithm. c) Difference image of phantom and artificially sheared phantom corrected with inverse transpose of registration algorithm output parameters.

4.3 Image Correction & Ultimate Reconstruction

The image registration parameters were applied to k-space as described in section 3.2.4. Translation must be applied before the affine matrix for an accurate registration, due to the way the registration algorithm computes the transformations. Once k-space was corrected, the images were compared to the reference images again and the lines of insufficiently registered sub-images were excluded from the cine-image reconstruction. The dataset was temporally oversampled by running the segment acquisition over many heartbeats, so k-space lines that cannot be corrected sufficiently by image registration could be discarded in the ultimate image reconstruction through correlation thresholding.

Correlation coefficients (CC) comparing the cardiac phase images to their reference were used as a measure of the success of respiratory motion correction, as calculated by the `corr2` function in MATLAB (Mathworks, Natick, MA). The calculation was performed only for the region of interest as delineated by the registration mask. The CC values were used as a measure of acceptance where the k-space lines corresponding to images with CC values below an arbitrary threshold were excluded from the ultimate image reconstruction. Initially the CC values were spread out from low values, due to small correlation between end-inspiration images and the reference images, to unity, where reference images were compared to themselves. After successful motion correction, the CC values should be higher overall with smaller deviation from the mean.

4.3.1 Patient Studies

Nine patients were scanned in mid-cardiac short-axis orientations during breath-hold and free-breathing. Two scans of mid-cardiac 4-chamber and 3-chamber orientations each were also acquired for characterization of the cine-navigator technique in other views. Imaging was performed on a Siemens Magnetom Sonata 1.5 Tesla scanner (Siemens Medical Solutions, Erlangen, Germany), with a two-channel quadrature array coil and six-channel spine array, with a selection of the channels of the latter used based on patient orientation. Imaging parameters included an FOV of 360 mm², 6 mm slice thickness, bandwidth of ± 100 kHz, flip angle of 60°, TE/TR of 1.5 ms/3.0 ms, 32 lines per segment, and 256 readout points per line. The breath-hold scans were acquired with a conventional Cartesian SSFP pulse sequence, and the ECG was monitored using the supplied ECG recorder unit of the Sonata scanner.

4.3.2 Quantitative Sharpness Analysis

Conventionally, cine-image quality is rated by cardiologists or radiologists in a blind test. To quantitatively measure the ultimate cine-image quality, the normalized sharpness Sh_{norm} can be calculated using:

$$Sh_{norm} = \max\left(\frac{dS_{norm}}{dr}\right) \quad (4.1)$$

where Sh_{norm} is the normalized sharpness or the slope of the normalized signal intensity S_{norm} (entire image's intensity values divided by the average bright blood signal value in the left ventricle) across the profile r , as calculated by the `diff` function in MATLAB. No windowing or leveling was performed otherwise. The bright blood signal was measured using the Region of Interest (ROI) tool in the `imagescn` function (Peter Kellman, National Institute of Health, Bethesda, Maryland) and profiles were measured using the `improfile` function in MATLAB. Profiles were taken across blood-myocardium interfaces (i.e. ventricle walls in short-axis (SAX) view), or if this was difficult, across blood-papillary muscle interfaces and the maximum sharpness was taken from the normalized signal profile plots. Pre-, post-correction and gold standard breath-hold maximum sharpness values were compared using a one-way analysis of variance (ANOVA) test and post-hoc Tukey-Kramer analysis to see if the datasets were significantly different ($p < 0.05$), using the `anova1` and `multcompare` functions. A flow chart of the process of statistical analysis is given in Figure 4.9. The ANOVA test determines if there are any significantly different

datasets, and the post-hoc analysis determines which specific datasets are different using pairwise comparisons. Left and right ventricles were individually isolated by a mask during registration to increase the accuracy of each ventricle's motion correction, and profiles are measured separately on each and compared to profiles measured on cardiac images corrected using a entire-heart mask.

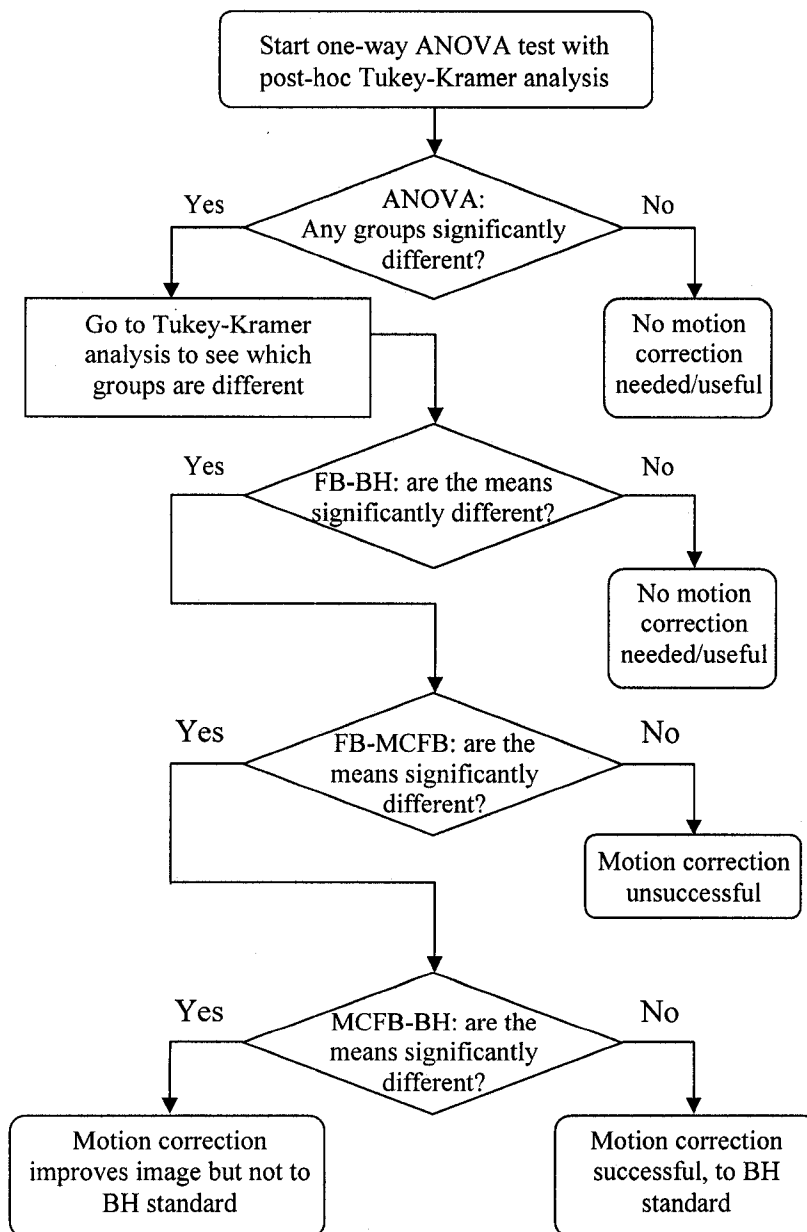


Figure 4.9 Flowchart of statistical analysis using the results of the one-way ANOVA test with Tukey-Kramer analysis. F values indicate if there is significant difference between any of the means of the groups being compared, while the Tukey-Kramer analysis performs pairwise comparisons to see which of the groups are significantly different. FB, free-breathing; MCFB, motion-corrected free-breathing; BH, breath-hold image series.

5 Results

In this chapter, a comparison of pre-registration to post-registration free-breathing gated-segmented images will be presented, as well as the comparison to the breath-hold gold standard. The effects of thresholding and variable masking will be examined and quantitative sharpness analysis results are displayed.

5.1 Acquisition

Each slice took 18 seconds to acquire, and the reconstruction from reading in the raw data to the output of the final image takes place in ~13 minutes. User input is required to choose the mask and reference dataset, but the technique is otherwise automated. The real-time image temporal resolution is less than 100 ms per image, while the gated-segmented cine-image temporal resolution is 30 frames per second.

5.2 Full Reconstruction

Images reconstructed with all lines of k-space demonstrated quantitative improvement in image sharpness, primarily in the differentiation of fine features such as the papillary muscles and the blood-myocardium interface (Figure 5.1). The most noticeable blurring in the FB series was in the left-right direction parallel to the intraventricular septum, thus the motion correction was the greatest in that direction. The anterior right ventricle wall at the top of the image still has remaining blurriness that is not corrected, due to local deformations that cannot be modeled by affine transformation. Radial streaking artifacts

are visible in the radial images outside the heart, mostly due to high-intensity fatty areas.

Appendix 1 contains images for all the patient studies for interest's sake.

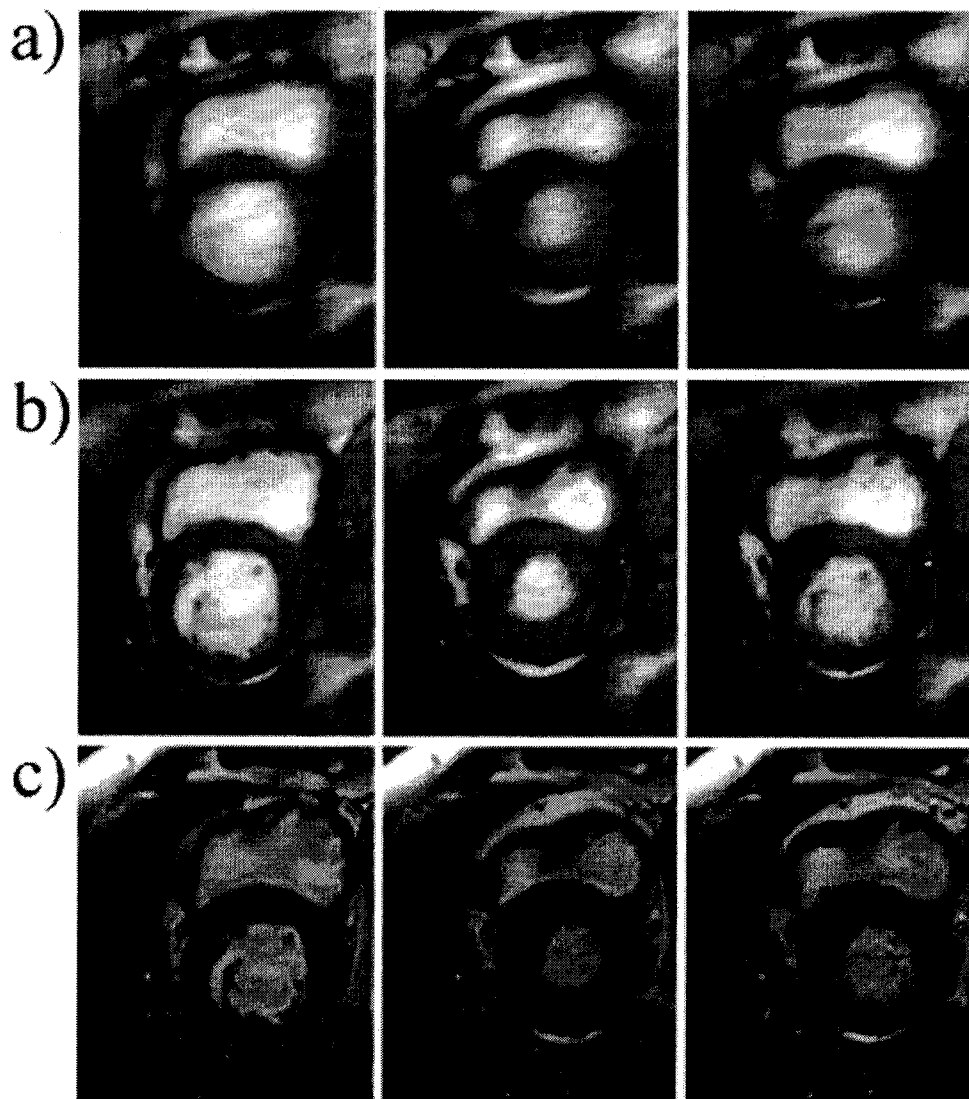


Figure 5.1 a) Pre-registration free-breathing, b) post-registration free-breathing, and c) breath-hold gold standard short-axis gated-segmented image. Images within each series are at (from left-to-right) end-diastole, end-systole, and mid-contraction.

5.3 Correlation Threshold Reconstruction

With thresholding, the post-registration real-time images are compared to their reference images, returning a spectrum of CC values. These are plotted in a histogram and an

arbitrary CC threshold level is chosen; in this case, a threshold level is chosen that would eliminate a set percentage of the real-time images (Figure 5.2).

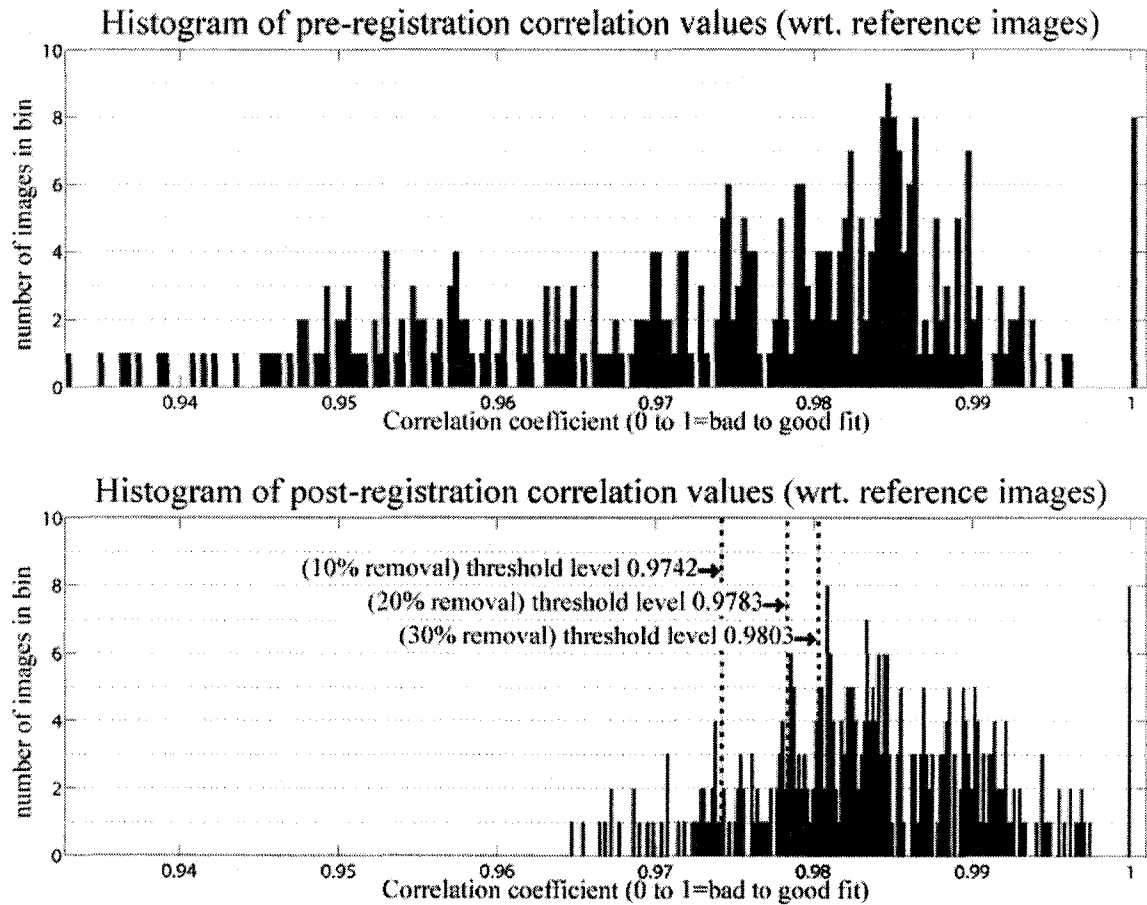


Figure 5.2 Sample histograms of correlation coefficient values for pre- (top) and post-registration (bottom) real-time images of short-axis view. Threshold levels for 10%, 20% and 30% removal of lines from final reconstruction are shown on the post-registration histogram.

The post-registration correlation coefficients are very high, so removing a certain percentage of the images does not have a significant effect, and introduces undersampling streaking artifacts into the image beyond 30% thresholding.

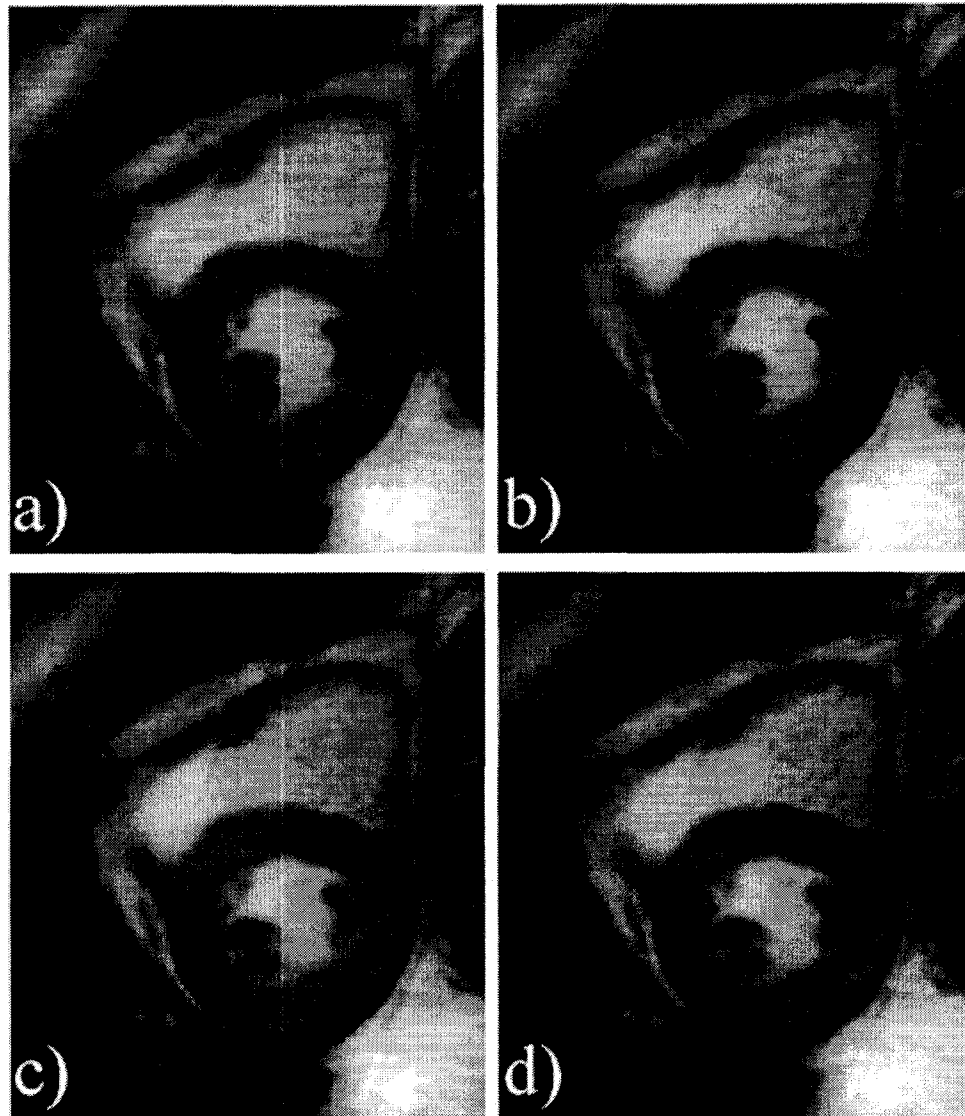


Figure 5.3 Correlation thresholded images at end-diastole: a) full reconstruction, b) 10% threshold, c) 20% threshold, and d) 30% threshold.

5.4 Sharpness Profiling Analysis

The maximum Sh_{norm} was measured over 4 profiles over the left ventricle at three cardiac phases (end-diastole, end-systole, and mid-contraction), for uncorrected free breathing (FB), motion-corrected free breathing (MCFB), and breath-hold (BH) image series from the nine patient studies (Figure 5.4). Profiles were drawn in 4 directions over the intraventricular septum (IVS), the LV posterior free wall (LV-PFW), the LV lateral free

wall (LV-LFW), and the LV anterior free wall (LV-AFW). The right ventricle physiology varies widely over the patient studies, making it difficult to compare meaningfully.

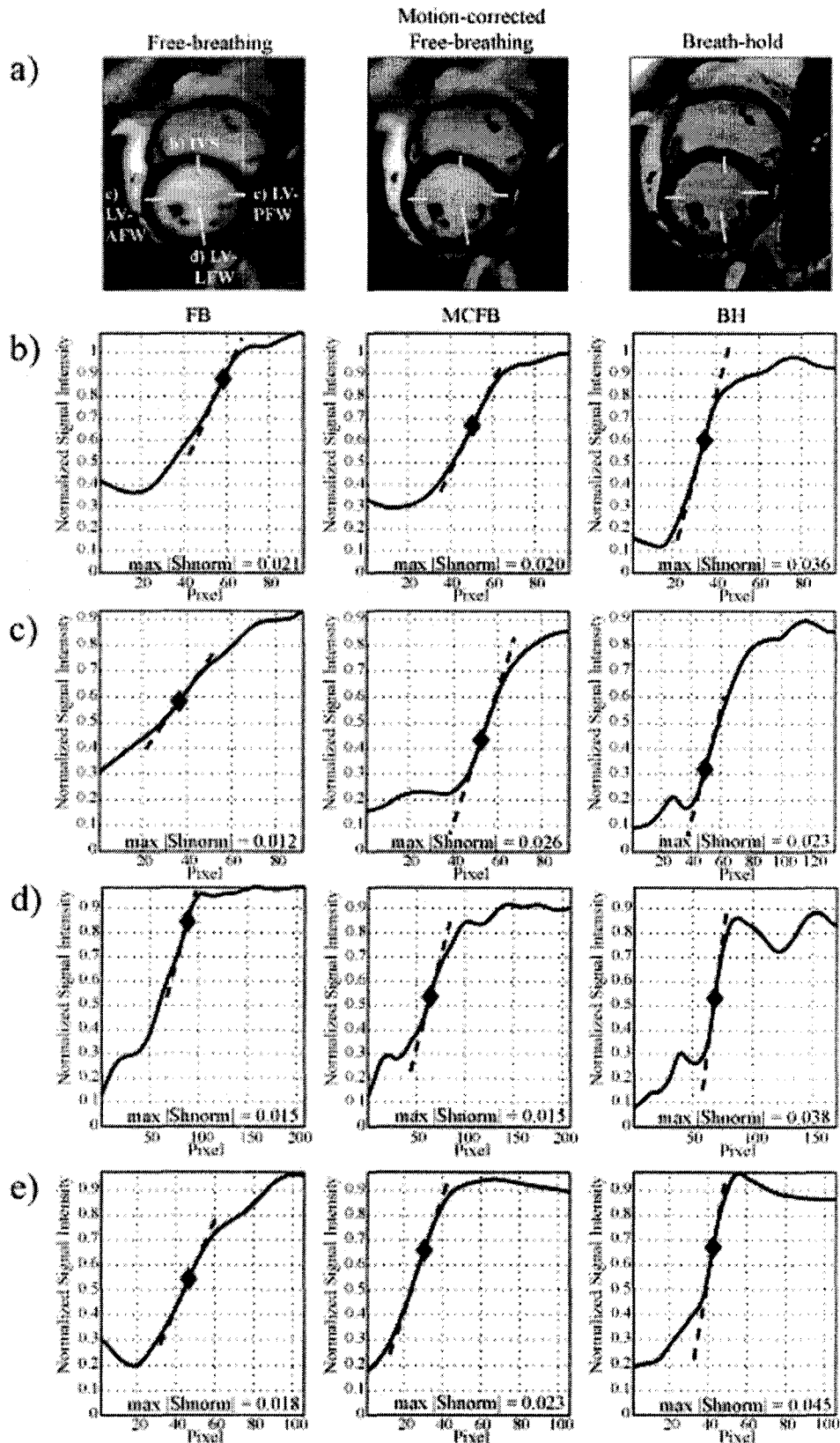


Figure 5.4 a) Example of profiles drawn over the left ventricle at end-diastole for the three image series (FB, MCFB, BH). The corresponding normalized signal profile plots are given for the b) IVS, c) LV-PFW, d) LV-LFW, and e) LV-AFW. The maximum absolute normalized sharpness ($\max |Sh_{norm}|$) is indicated on the graph with a diamond.

ANOVA tests with Tukey-Kramer post-hoc analysis were performed across the three image series to see if their mean maximum Sh_{norm} values were significantly different from each other. Box plots illustrating the confidence intervals of the sharpness values across nine patients are displayed in Figure 5.5 below.

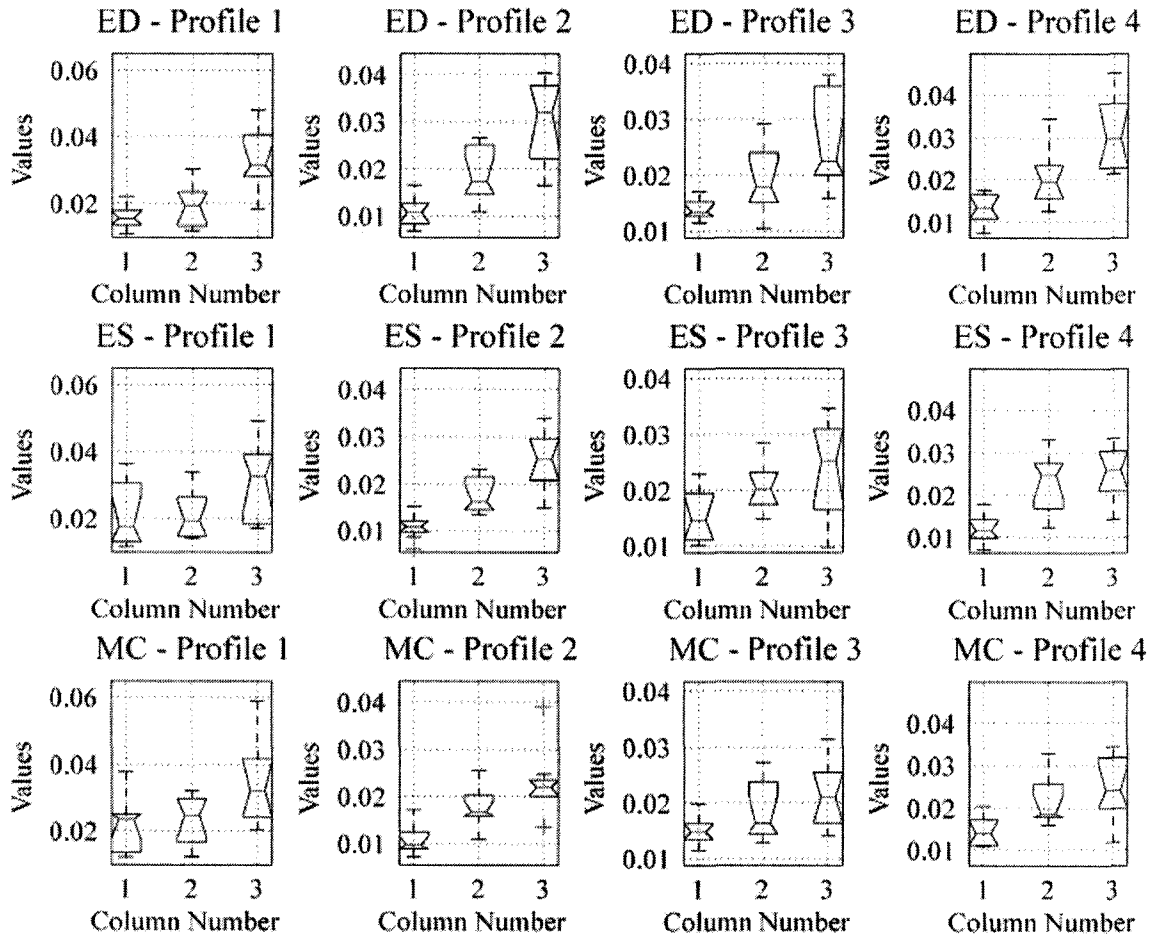


Figure 5.5 Motion correction with entire-heart mask. Box plots of max $|Sh_{norm}|$ values for 4 profiles drawn on three different cardiac phases across 9 patient studies. ED, end-diastole; ES, end-systole; MC, mid-contraction. Profile 1, IVS; Profile 2, LV-PFW; Profile 3, LV-LFW; Profile 4, LV-AFW. Column 1, FB; Column 2, MCFB; Column 3, BH.

The median and lower/upper quartile values are the middle, bottom and top horizontal lines respectively, and the whiskers indicate the extent of the rest of the data to 1.5 times the interquartile value. Outliers are indicated by crosses, and the notches are a robust

estimate of the uncertainty about the medians. If the notches do not overlap between datasets, they are significantly different for $p < 0.05$ or 95% confidence. Thus box plots are a quick way to see if there is any significant difference in sharpness between FB, MCFB, and BH image series.

Another more rigorous way of looking at the results is to use the results of the pairwise comparisons from the post-hoc Tukey-Kramer analysis as in Figure 4.9. Figure 5.6 gives the estimated difference between mean maximum $|Sh_{norm}|$ values of each pairwise comparison with their upper and lower confidence limits. If the range between the confidence limits does not include zero, the datasets are significantly different.

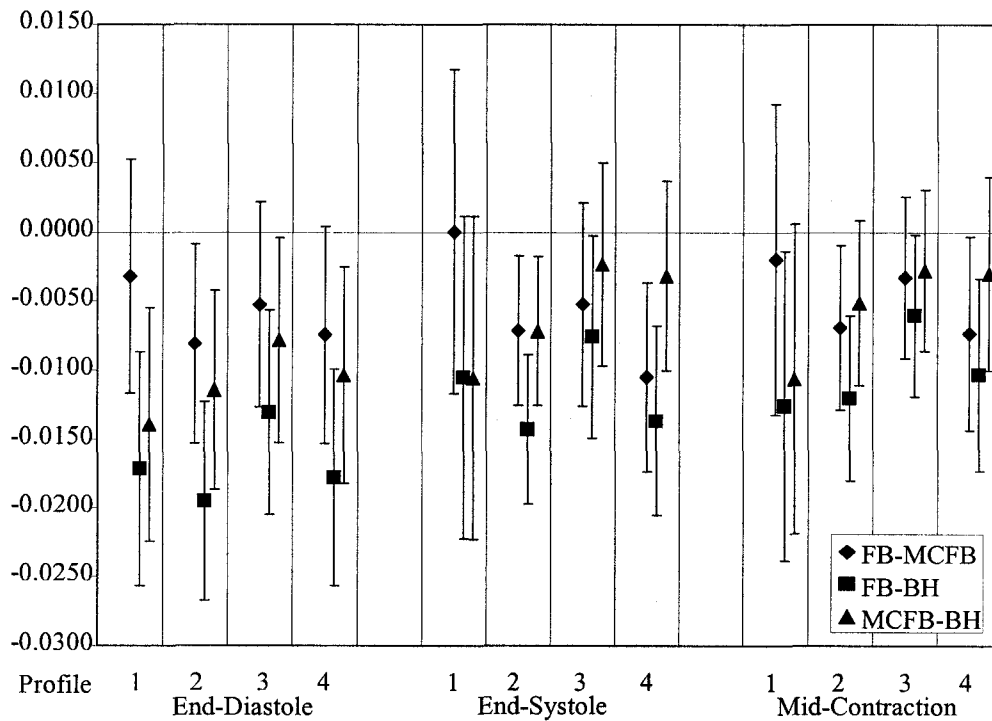


Figure 5.6 Motion correction with entire-heart mask. Graph of estimated differences between mean maximum $|Sh_{norm}|$ values for each pairwise comparison (FB-BH, FB-MCFB, MCFB-BH) and the respective confidence interval limits for $p < 0.05$. If range does not include 0, groups are significantly different. Profile 1, IVS; Profile 2, LV-PFW; Profile 3, LV-LFW; Profile 4, LV-AFW.

Motion correction is most successful in the directions parallel to the intraventricular septum, as illustrated by profiles 2 and 4 for each cardiac phase in both Figure 5.5 and Figure 5.6. The box plots of profiles 2 and 4 do not show any overlap in the notches for FB-MCFB (except for ED profile 4), and the confidence interval range for FB-MCFB shows a significant difference between the two datasets, while the confidence interval range for MCFB-BH shows less or no significant difference than FB-BH at end-systole or mid-contraction. The exception for profile 4 at end-diastole may be due to increased local deformations due to the lower pressure inside the ventricle, making the ventricle wall shape more susceptible to respiratory pressure changes. Motion in the direction perpendicular to the intraventricular septum is either less noticeable and does not require correction, as in profile 1 and 3 for end-systole and mid-contraction, or is not correctable due to local deformations, as in profile 1 and 3 for end-diastole. In most cases, the estimated mean difference is smaller for MCFB-BH (after correction) than FB-BH (before correction). A table summarizing the results is given below.

Image	Profile	FB-MCFB	FB-BH	MCFB-BH	Result
ED	IVS	0	1	1	Motion correction unsuccessful
ES	IVS	0	0	0	No motion correction needed/useful
MC	IVS	0	1	0	Motion correction unsuccessful, but no difference between MCFB-BH
ED	LV-PFW	1	1	1	Motion correction successful, not to BH standards
ES	LV-PFW	1	1	1	Motion correction successful, not to BH standards
MC	LV-PFW	1	1	0	Motion correction successful, to BH standards
ED	LV-LFW	0	1	1	Motion correction unsuccessful
ES	LV-LFW	0	1	0	Motion correction unsuccessful, but no difference between MCFB-BH
MC	LV-LFW	0	1	0	Motion correction unsuccessful, but no difference between MCFB-BH

ED	LV-AFW	0	1	1	Motion correction unsuccessful
ES	LV-AFW	1	1	0	Motion correction successful, to BH standards
MC	LV-AFW	1	1	0	Motion correction successful, to BH standards

Table 5.1 Summary of results of motion correction for EH mask, for ED, ES and MC images, across four profiles (IVS, LV-PFW, LV-LFW, LV-AFW). 1 means there is significant difference between the image series (FB, MCFB, BH), 0 means there is none.

5.5 Individual Ventricle Correction

Individual ventricles were isolated in the SAX view and motion correction was performed to see if there was any improvement from the entire-heart motion correction procedure. The left ventricle box plots and mean difference graph are presented in Figure 5.7 and Figure 5.8. There is an increase in the MCFB confidence interval for profile 2 at mid-contraction, but overall the difference from the entire-heart registration procedure is slight. The results of the motion correction are given in Table 5.2.

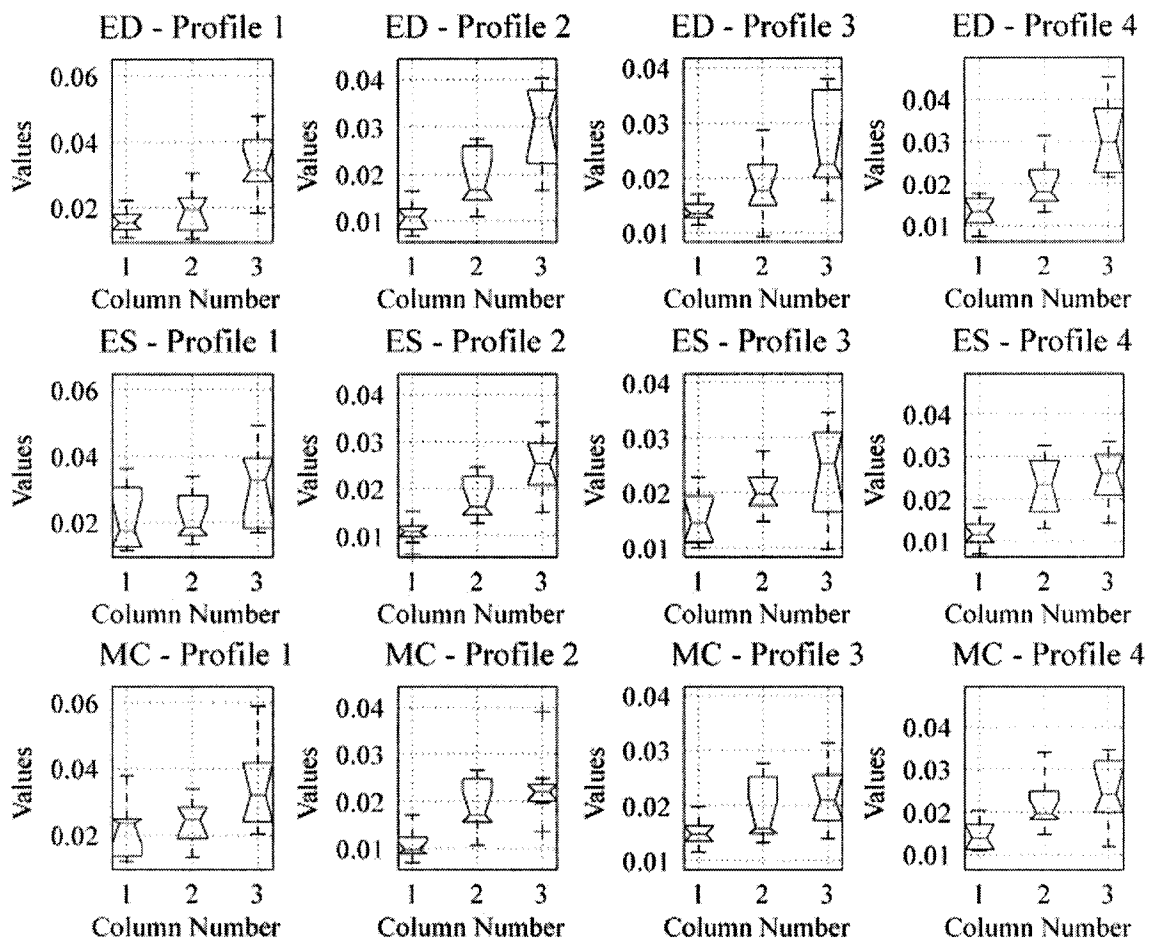


Figure 5.7 Motion correction with left-ventricle mask. Box plots of $\max |Sh_{\text{norm}}|$ values for 4 profiles drawn on three different cardiac phases across 9 patient studies. ED, end-diastole; ES, end-systole; MC, mid-contraction. Profile 1, IVS; Profile 2, LV-PFW; Profile 3, LV-LFW; Profile 4, LV-AFW. Column 1, FB; Column 2, MCFB; Column 3, BH.

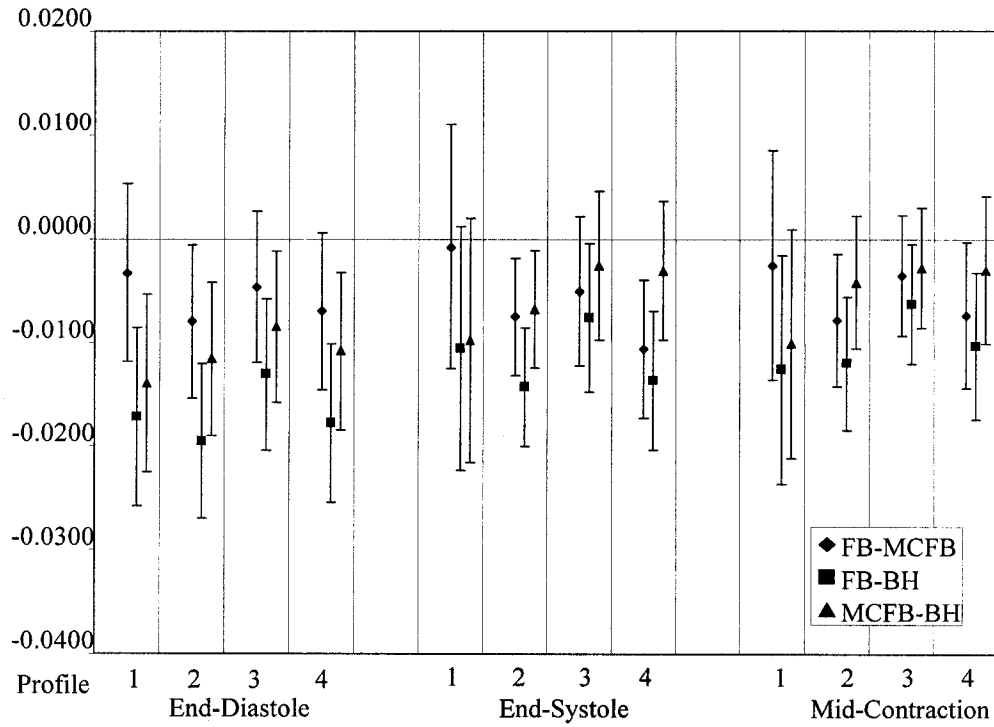


Figure 5.8 Motion correction with left-ventricle mask. Graph of estimated differences between mean maximum $|Sh_{norm}|$ values for each pairwise comparison (FB-BH, FB-MCFB, MCFB-BH) and the respective confidence interval limits for $p < 0.05$. If range does not include 0, groups are significantly different.

Image	Profile	FB-MCFB	FB-BH	MCFB-BH	Result
ED	IVS	0	1	1	Motion correction unsuccessful
ES	IVS	0	0	0	No motion correction needed/useful
MC	IVS	0	1	0	Motion correction unsuccessful, but no difference between MCFB-BH
ED	LV-PFW	1	1	1	Motion correction successful, not to BH standards
ES	LV-PFW	1	1	1	Motion correction successful, not to BH standards
MC	LV-PFW	1	1	0	Motion correction successful, to BH standards
ED	LV-LFW	0	1	1	Motion correction unsuccessful
ES	LV-LFW	0	1	0	Motion correction unsuccessful, but no difference between MCFB-BH
MC	LV-LFW	0	1	0	Motion correction unsuccessful, but no difference between MCFB-BH
ED	LV-AFW	0	1	1	Motion correction unsuccessful
ES	LV-AFW	1	1	0	Motion correction successful, to BH standards

MC	LV-AFW	1	1	0	Motion correction successful, to BH standards
----	--------	---	---	---	---

Table 5.2 Summary of results of motion correction for LV mask, for ED, ES and MC images, across four profiles (IVS, LV-PFW, LV-LFW, LV-AFW). 1 means there is significant difference between the image series (FB, MCFB, BH), 0 means there is none.

5.6 Other Orientations

To test how well other orientations did with motion correction, four-chamber and three-chamber views were obtained for a limited number of the patients. Due to the motion-insensitivity of the radial trajectory, there were no extremely noticeable artifacts in the images. Figure 5.9 displays the pre- and post-registration correlation coefficient histograms for a four-chamber orientation, which shows that motion correction in this orientation does not have as great an effect as in the SAX orientation, and Figure 5.10 shows the pre- and post-correction 4-chamber view images for full reconstruction and thresholded reconstruction at 10 and 30 percent removal.

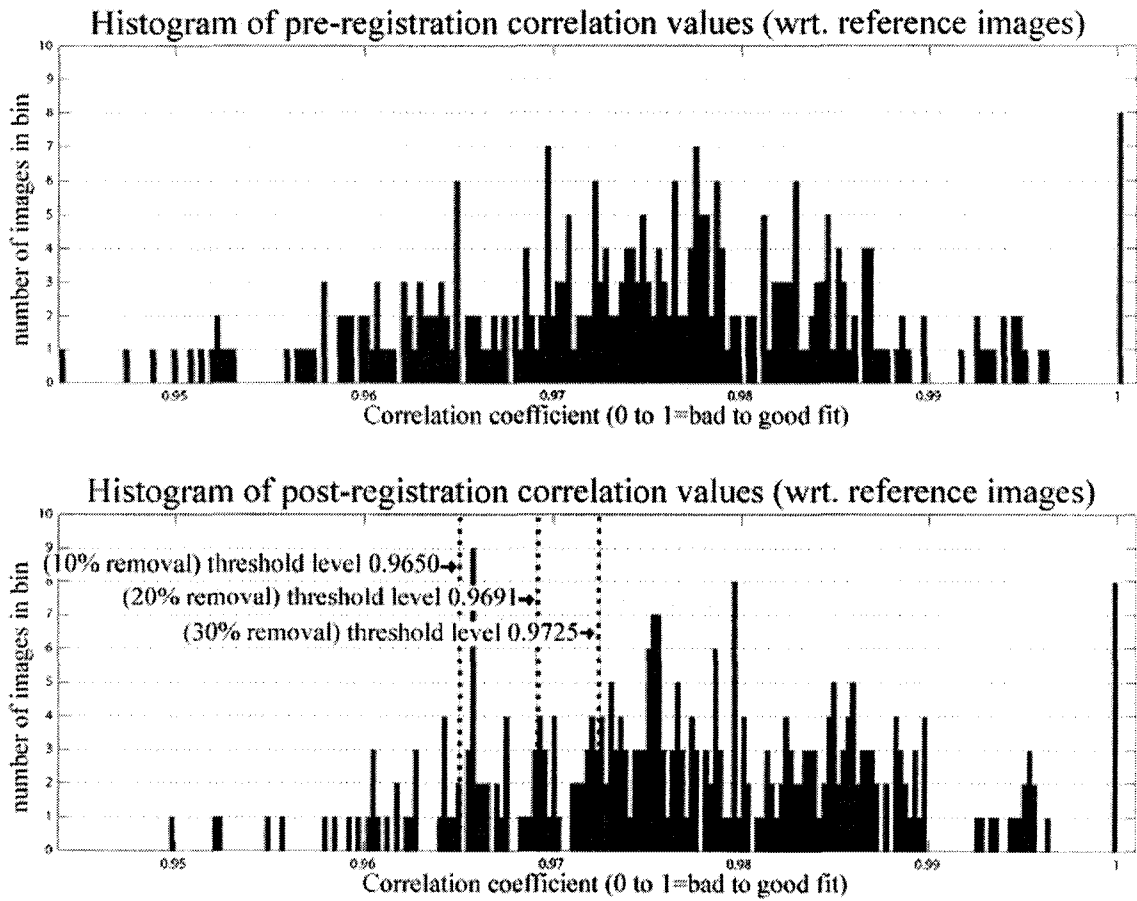


Figure 5.9 Sample histograms of correlation coefficient values for pre- (top) and post-registration (bottom) real-time images of four-chamber orientation. Threshold levels for 10%, 20% and 30% removal of lines from final reconstruction are shown on the post-registration histogram.

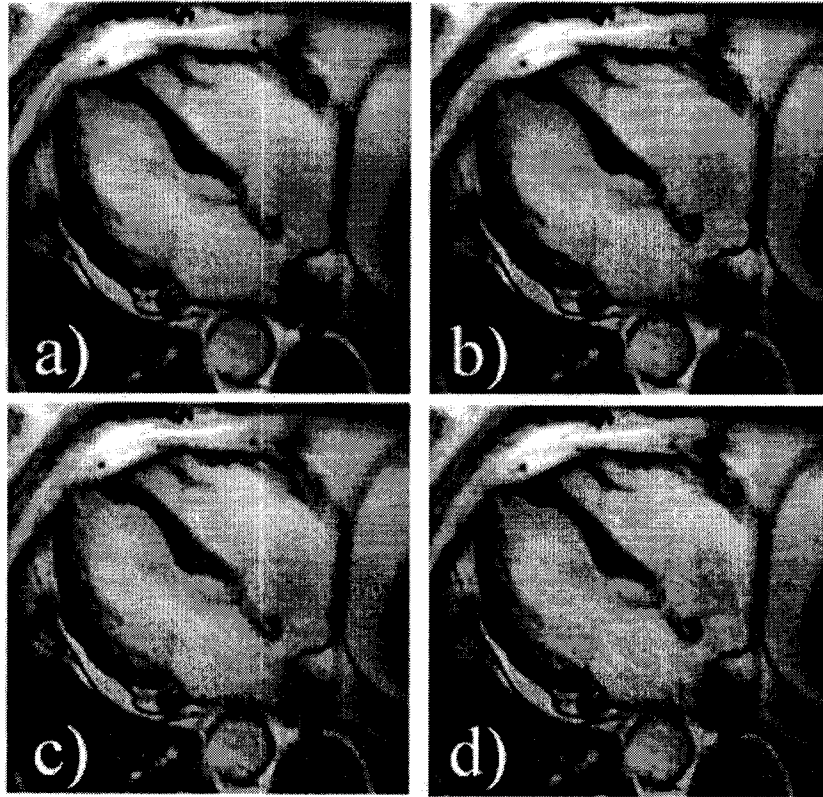


Figure 5.10 4-chamber view of the heart for: a) uncorrected free-breathing, b) motion-corrected free-breathing at full reconstruction, c) 10% thresholded, and d) 30% thresholded motion-corrected free-breathing.

6 Discussion/Conclusion

A cine-navigator technique was presented for correction of motion artifacts due to respiration during cardiac imaging. The k-space data was acquired in a segmented radial trajectory and interleaved such that the k-space lines had high temporal resolution. The trajectory was designed to minimize large jumps in k-space to eliminate eddy current artifacts.

The k-space data was reconstructed as both real-time images and conventional gated-segmented images. Respiratory motion was separated from cardiac motion effects by intra-cardiac phase image registration. The real-time images in each phase were registered to a user-selected reference image to measure the effect of respiratory motion on the heart, and the returned affine transformation parameters were then directly applied to the k-space lines. The conventional gated-segmented reconstruction used the corrected lines to produce a motion-corrected image with high spatial and temporal resolution. The in-plane resolution was 3-5 times higher than the slice resolution, so imaging was tolerant of through-plane motion.

Some features to note about this technique are that it requires no extraneous navigator acquisitions or respiratory gating but relies on the k-space data itself to measure and correct respiratory motion, so the scan time is not prolonged by a low duty cycle. Respiratory motion is measured directly from the heart, which is more accurate than external transducers like pneumatic pressure belts. The duty cycle is 100%, and there is no patient exclusion based on breath-hold ability. The acquisition is longer than the

single-slice breath-hold scan because of the multiple heartbeat segment acquisition, but for multiple slice acquisitions the higher duty cycle of the cine-navigator technique may result in a shorter scan time overall. The reconstruction is user-friendly and almost entirely automated, with only the selection of the reference image set and the ROI mask requiring input.

K-space acquisition is retrospectively triggered which means there is no control over which phase encode lines are acquired at a specific cardiac phase, so if the segments fit evenly within a cardiac cycle, it is possible to re-acquire the same segment at the same point in time, reducing the temporal sampling density at other points. A future development may be to incorporate prospective triggering into the acquisition to ensure even temporal coverage and perhaps minimize the number of heartbeats the segment is acquired over. Due to the lack of cardiac triggering, temporal regridding is required to reconstruct the gated-segmented images and may possibly contribute to blurring in the image.

The technique has numerous degrees of flexibility. The user can choose any feature of interest through masking and focus on motion correction of that feature alone. There are no constraints on how big or small the mask may be, but it is advisable to block out high intensity fatty areas to avoid misregistration. The reference image series is chosen at end-expiration for consistency with breath-hold standards but the procedure does not suffer if the reference images are chosen at another respiratory phase, although they may have more local deformation than at end-expiration. Future developments could include the

automation of reference image selection through a translation waveform slope calculation, and the technique may need to be refined for fast or irregular breathing patterns that are too erratic for the current method. Pediatric patients in particular have high breathing rates that may require the individual selection of reference frames for each phase instead of using the frames from one single heartbeat.

Once the reference images are chosen, the cine-navigator technique can measure motion even in the case of fast irregular breathing patterns. Image registration can return translation, rotation, or affine transformation parameters depending on the needs of the situation. This allows for application to other parts of the body, such as the head or the extremities. The algorithm also has the capability to do 3D registration for use in whole heart acquisitions. The respiratory waveform as mapped out by the transformation parameters may contain high-frequency components unrelated to respiratory motion, which could be eliminated through some energy minimization scheme. More accurate motion measurement can be achieved with a more complex motion model, but caution must be exercised lest pertinent local deformations caused by conditions such as myocardial infarct are eliminated from the images.

Correlation thresholding is an option that was explored in this project to see if it could eliminate through-plane motion or local deformations. Since the radial trajectory is insensitive to motion and the in-plane/slice resolution ratio renders the images insensitive to through-plane motion, the correlation coefficients before registration were already quite high, and after correction all the images have very little difference from the

reference images. Thresholding thus did not produce a noticeable effect on normal images, and beyond 30% elimination, radial streaking artifacts were more severe due to undersampling of certain portions of the dataset. In tests that artificially sheared 10% of the real-time images, the correlation thresholding was able to detect and eliminate the sheared images, but this shearing was extreme and not representative of normal respiratory-induced deformation.

Spatial regridding of the radial trajectory to a Cartesian grid for fast Fourier transform application is an important step that determines the quality of the gated-segmented images. Undersampling and holes in k-space introduce streaking and blurring artifacts into the image which can be minimized with a proper density compensation function. The iterative DCF calculation method proposed by Pipe is accurate but time consuming, and reconstruction time can be decreased if the DCF and regridding computation time is reduced through more streamlined coding.

Temporal regridding is applied to the k-space data to weight the data closer to the time point of the actual cardiac phase higher than data in between the phases. Another approach is to filter the k-space data such that the low-frequency information further away from the desired cardiac phase time is removed with care taken not to severely undersample the dataset, and the high-frequency information is preserved. In this way, blurring could be reduced while edge sharpness is preserved [6, 11]. Cardiac phases at the beginning and end of the cardiac cycle are wrapped around to the other side, but after

registration may not match up with the adjacent cardiac phase's data trajectory and there may be undersampling or k-space hole artifacts.

Sharpness profiling indicated that blurring was more pronounced in the direction parallel to the IVS in the SAX view, so it naturally follows that motion correction is most effective in that direction as well. The overall cine-image quality will be rated by cardiologists in a future study. Fine features such as the papillary muscles that were obscured in the free-breathing dataset were more distinguishable post-registration. Other orientations of the heart did not demonstrate significant motion artifacts even before the motion correction was applied, due to the motion insensitivity of the radial trajectory, and thus were not significantly altered post-registration. The technique could be applied to other parts of the body that undergo respiratory motion, such as the liver or the lungs, and image-registration-based motion measurement may be useful in tracking motion in other regions such as the head or the extremities.

In conclusion, a relatively fast and effective cine-navigator imaging technique for the elimination of respiratory motion artifacts has been presented. The dual purpose acquisition does not interrupt the acquisition for motion measurement, and there is no patient exclusion based on breathing ability. The method allows the user a large amount of control over the process through relatively simple steps, and it is flexible for patient exam requirements. Further validation in the form of ventricular volume measurement will be needed prior to any clinical application. Some issues that must be addressed are the shortening of reconstruction time through more efficient coding, temporal filtering to

eliminate further blurring, and better spatial regridding for datasets that are undersampled or have holes in the trajectory, such as might occur during thresholding. Future acquisition considerations include the effect of tissue power deposition in 3D acquisitions, the inclusion of a steady-state initialization prepulse, the use of prospective gating or self-gating, and the incorporation of alternative Cartesian and spiral trajectories with parallel imaging.

7 Bibliography

1. Aisen, A., et al., *Motion artifacts in quantitative magnetic resonance imaging*. Magn Reson Imag, 1986. 4(3): p. 207-213.
2. Atalar, E. and L. Onural, *A respiratory motion artifact reduction method in magnetic resonance imaging of the chest*. IEEE Trans Med Imag, 1991. 10(1): p. 11-24.
3. Axel, L., et al., *Respiratory effects in two-dimensional Fourier transform MR imaging*. Radiology, 1986. 160(3): p. 795-801.
4. Bailes, D., et al., *Respiratory ordered phase encoding (ROPE): a method for reducing respiratory motion artifacts in MR imaging*. J Comput Assist Tomogr, 1985. 9: p. 835-838.
5. Bloch, F., W. Hansen, and M. Packard, *Nuclear Induction*. Phys Rev, 1946. 69(3-4): p. 127.
6. Block, W., et al. *3D time-resolved vastly undersampled isotropic projection (VIPR) imaging with spatial frequency dependent temporal filtering*. in *ISMRM workshop on minimum MR data acquisition methods: making more with less*. 2000. Marco Island, FL: ISMRM.
7. Boll, D., et al., *Comparison of ECG-gated rectilinear vs real-time radial k-space sampling schemes in cine true-FISP cardiac MRI*. J Card Magn Reson, 2004. 6(4): p. 793-802.
8. Bornstedt, A., *Introduction to motion suppression and motion correction*. 1 ed. Cardiovascular Magnetic Resonance, ed. E. Nagel, A.v. Rossum, and E. Fleck. Vol. 1. 2004, Germany: Steinkopff Verlag Darmstadt. 302.

9. Danias, P., et al., *Prospective navigator correction of image position for coronary MR angiography*. Radiology, 1997. **203**(3): p. 733-736.
10. Danias, P., et al., *Relationship between motion of coronary arteries and diaphragm during free breathing - lessons from real-time MR imaging*. Am J Roentgenol, 1999. **172**: p. 1061-1065.
11. Du, J., et al., *Time-resolved, undersampled projection reconstruction imaging for high-resolution CE-MRA of the distal runoff vessels*. Magn Reson Med, 2002. **48**(3): p. 516-522.
12. Edelstein, W., et al., *Spin warp NMR imaging and applications to human whole-body imaging*. Phys Med Biol, 1980. **25**: p. 751-756.
13. Ehman, R. and J. Felmlee, *Adaptive technique for high-definition MR imaging of moving structures*. Radiology, 1989. **173**(1): p. 255-263.
14. Firmin, D. and J. Keegan, *Navigator echoes in cardiac magnetic resonance*. J Card Magn Reson, 2001. **3**(3): p. 183-193.
15. Fuchs, F., G. Laub, and K. Othomo, *TrueFISP - technical considerations and cardiovascular applications*. Eur J Radiology, 2003. **46**(1): p. 28-32.
16. Gatehouse, P. and D. Firmin, *The cardiovascular magnetic resonance machine: hardware and software requirements*. Herz, 2000. **25**(4): p. 317-330.
17. Haacke, E. and J. Patrick, *Reducing motion artifacts in two-dimensional fourier transform imaging*. Magn Reson Imag, 1986. **4**(4): p. 359-376.
18. Haacke, E. and G. Lenz, *Improving MR image quality in the presence of motion by using rephasing gradients*. AJR, 1987. **148**: p. 1251-1258.
19. Hahn, E., *Spin echoes*. Phys Rev, 1950. **80**(4): p. 580-594.

20. Hardy, C., et al., *Coronary MR angiography: respiratory motion correction with BACSPIN*. J Magn Reson Imaging, 2003. **17**(2): p. 170-176.
21. Holland, A., J. Goldfarb, and R. Edelman, *Diaphragmatic and cardiac motion during suspended breathing: preliminary experience and implications for breath-hold MR imaging*. Radiology, 1998. **209**(2): p. 483-489.
22. Jackson, J., et al., *Selection of a convolution function for Fourier inversion using gridding*. IEEE Trans Med Imag, 1991. **10**(3): p. 473-478.
23. Keegan, J., et al., *Coronary artery motion with the respiratory cycle during breath-holding and free-breathing: Implications for slice-followed coronary artery imaging*. Magn Reson Med, 2002. **47**(3): p. 476-481.
24. Korin, H., et al., *Spatial-frequency-tuned markers and adaptive correction for rotational motion*. Magn Reson Med, 1995. **33**: p. 663-669.
25. Larson, A., et al., *Cardiac imaging techniques*. 3 ed. Clinical Magnetic Resonance Imaging, ed. R. Edelman, et al. Vol. 1. 2006, Philadelphia: Saunders Elsevier. 4200.
26. Larson, A., et al., *Self-gated cardiac cine MRI*. Magn Reson Med, 2004. **51**(1): p. 93-102.
27. Lauterbur, P., *Image formation by induced local interactions: examples employing nuclear magnetic resonance*. Nature, 1973. **242**(5394): p. 190-191.
28. Manke, D., et al., *Respiratory motion in coronary magnetic resonance angiography: a comparison of different motion models*. JMRI, 2002. **15**(6): p. 661-671.

29. Mansfield, P., *Multi-planar image formation using NMR spin echoes*. J Phys C, 1977. **10**(3): p. L55-L58.
30. McConnell, M., et al., *Comparison of respiratory suppression methods and navigator locations for MR coronary angiography*. AJR, 1997. **168**(5): p. 1369-1375.
31. McConnell, M., et al., *Prospective adaptive navigator correction for breath-hold MR coronary angiography*. Magn Reson Med, 1997. **37**(1): p. 148-152.
32. McLeish, K., et al., *Free-breathing radial acquisitions of the heart*. Magn Reson Med, 2004. **52**(5): p. 1127-1135.
33. McLeish, K., et al., *A study of the motion and deformation of the heart due to respiration*. IEEE Trans Med Imag, 2002. **21**(9): p. 1142-1150.
34. Mitsa, T., et al., *Correction of periodic motion artifacts along the slice selection axis in MRI*. IEEE Trans Med Imag, 1990. **9**(3): p. 310-317.
35. Nayak, K., et al., *Real-time cardiac MRI at 3 tesla*. Magn Reson Med, 2004. **51**(4): p. 655-660.
36. Nehrke, K., et al., *Free-breathing cardiac MR imaging: study of implications of respiratory motion - initial results*. Radiology, 2001. **220**(3): p. 810-815.
37. Nguyen, T., et al., *Direct monitoring of coronary artery motion with cardiac fat navigator echoes*. Magn Reson Med, 2003. **50**: p. 235-241.
38. Oppelt, A., et al., *FISP - a new fast MRI sequence*. Electromedica, 1986. **54**: p. 15-18.
39. Pattany, P., et al., *Motion artifact suppression technique (MAST) for MR imaging*. J Comput Assist Tomogr, 1987. **11**(3): p. 369-377.

40. Peters, D., et al., *Undersampled projection reconstruction applied to MR angiography*. Magn Reson Med, 2000 Jan. **43**(1): p. 91-101.
41. Pipe, J., *Reconstructing MR images from undersampled data: data-weighting considerations*. Magn Reson Med, 2000. **43**: p. 867-875.
42. Pipe, J. and T. Chenevert, *A progressive gradient moment nulling design technique*. Magn Reson Med, 1991. **19**(1): p. 175-179.
43. Pipe, J. and P. Menon, *Sampling density compensation in MRI: rationale and an iterative numerical solution*. Magn Reson Med, 1999. **41**(1): p. 179-186.
44. Purcell, E., H. Torrey, and R. Pound, *Resonance absorption by nuclear magnetic moments in a solid*. Phys Rev, 1946. **69**: p. 37-38.
45. Quencer, R., et al., *Improved MR imaging of the brain by using compensating gradients to suppress motion-induced artifacts*. AJR, 1988. **151**: p. 163-170.
46. Runge, V. and M. Wood, *Fast imaging and other motion artifact reduction schemes: a pictorial overview*. Magn Reson Imag, 1988. **6**(5): p. 595-608.
47. Runge, V., et al., *Respiratory gating in magnetic resonance imaging at 0.5 Tesla*. Radiology, 1984. **151**(2): p. 521-523.
48. Sachs, T., et al., *The diminishing variance algorithm for real-time reduction of motion artifacts in MRI*. Magn Reson Med, 1995. **34**(3): p. 412-422.
49. Schultz, C., et al., *The effect of motion on two-dimensional Fourier transformation magnetic resonance images*. Radiology, 1984. **152**(1): p. 117-121.
50. Sussman, M., et al., *Variable-density adaptive imaging for high-resolution coronary artery MRI*. Magn Reson Med, 2002. **48**(5): p. 753-764.

51. Thevenaz, P., U. Ruttimann, and M. Unser, *A pyramid approach to subpixel registration based on intensity*. IEEE Trans Image Process, 1998. **7**(1): p. 27-41.
52. Thompson, R. *Free Breathing Cine MRI*. 2006. Miami, FL.
53. Thompson, R. and E. McVeigh, *Flow-gated Phase-Contrast MRI Using Radial Acquisitions*. Magn Reson Med, 2004. **52**(3): p. 598-604.
54. Walle, R.V.d., I. Lemahieu, and E. Achten, *Magnetic resonance imaging and the reduction of motion artifacts: review of the principles*. Technol Health Care, 1997. **5**(6): p. 419-435.
55. Walle, R.V.d., I. Lemahieu, and E. Achten, *Two motion-detection algorithms for projection-reconstruction magnetic resonance imaging: theory and experimental verification*. Comput Med Imaging Graph, 1998 Mar-Apr. **22**(2): p. 115-121.
56. Wang, W., R. Grimm, and S. Riederer, *A modified projection reconstruction trajectory for reduction of undersampling artifacts*. J Magn Reson Imaging, 2005 Feb. **21**(2): p. 179-186.
57. Welch, E., et al., *Self-navigated motion correction using moments of spatial projections in radial MRI*. Magn Reson Med, 2004 Aug. **52**(2): p. 337-345.
58. Wilman, A. and C. Beaulieu, *Principles of Magnetic Resonance Imaging*. University of Alberta, 2005.
59. Wood, M. and R. Henkelman, *MR image artifacts from periodic motion*. Med Phys, 1984. **12**(2): p. 143-151.
60. Wood, M. and R. Henkelman, *Suppression of respiratory motion artifacts in magnetic resonance imaging*. Med Phys, 1986. **13**(6): p. 794-805.

8 Appendix I

Presented are the SAX images from all the studies at end diastole, end systole, and mid-contraction for free-breathing, motion-corrected free-breathing and breath-hold series. The rows represent pre-registration free-breathing, post-registration free-breathing, and breath-hold gold standard short-axis gated-segmented images, and the columns within each series represent images at (from left-to-right) end-diastole, end-systole, and mid-contraction.

